2012

The Dynamic Model of the Foot and Ankle System

Hwa Bok Wee
Lehigh University

The Dynamic Model of the Foot and Ankle System

by

Hwa Bok Wee

Presented to the Graduate and Research Committee

of Lehigh University

in Candidacy for the Degree of

Doctor of Philosophy

in

Mechanical Engineering

Lehigh University

September 2012

Approved and recommended for acceptance as a dissertation in partial fulfillment of the requirements for the degree of Doctor of Philosophy

_____

Date

_____
Dr. Arkady Voloshin, Dissertation Advisor

_____

Accepted Date

Committee Members:

_____
Dr. Sudhakar Neti, Committee Member

_____
Dr. N. Duke Perreira, Committee Member

_____
Dr. Eric P. Salathe, Committee Member

Acknowledgments

I sincerely appreciate my advisor Prof. Arkady Voloshin. My academic achievement would not have been possible without his guidance. He always inspired and encouraged me to become an independent researcher and keep going through the tough times.

I would like to thank my committee members, Prof. Sudhakar Neti, Prof. N. Duke Perreira, Prof. Eric P. Salathe, for their help and advice. I also thank Prof. Susan Perry. She has helped me to learn a new academic research area and given me good advice for life and future. In addition, I would like to thank Prof. Jacob Kazakia for his support.

I am thankful to Korean friends and colleagues for their help. Especially, I would like to give many thanks to Jonghyun Oh. He has supported and encouraged me like a big brother and a friend.

Finally, I have a great debt of gratitude to my family, father, mother, father in-law, mother in-law, and all other family members for their love and constant support. I would like to give special thanks to my wife, son, and daughter for their sacrifice and support.

To My Family

Geum Hwa Lee, Alex Jonghyun Wee, and Claire Seohyun Wee

Table of Contents

Acknowledgments ..... **iv**
Table of Contents ..... **vi**
List of Tables ..... **viii**
List of Figures ..... **ix**
ABSTRACT **1**
CHAPTER 1
Introduction **3**
1.1 Motivation 3
1.2 Overview of the structure and function of the foot and ankle [1, 2] 4
1.3 Overview of the effect of vibration on human [4] 6
1.4 Overview of the system identification [8, 9] 7
1.5 Organization of Thesis 9
CHAPTER 2
Dynamic response of human foot and ankle to vertical vibration **11**
2.1 Introduction 11
2.2 Methods 14
2.2.1 Subjects 14
2.2.2 Experimental set-up 16
2.2.3 Data Analysis 18
2.3 Results 19
2.3.1 Effect of the load on transmissibility and phase 19
2.3.2 Effect of the posture on transmissibility and phase 24
2.3.3 Transmissibility of single degree of freedom model 27
2.4 Discussion 29
2.5 Conclusion 31
Chapter 3
Foot and ankle system identification base on black box models **33**
3.1 Introduction 33
3.2 Method 36
3.2.1 Experimental data and procedures of system identification 36

3.2.2 Model structure selection, estimation, validation 37
3.3 Results 43
3.4 Conclusions 49

CHAPTER 4

Development of the dynamic model of the foot and ankle system exposed to vertical vibration 51

4.1 Introduction 51
4.2 The model of the foot and ankle 54
4.3 Equations of motion 59
4.4 Simplification of dynamic equations 67
4.5 Parameter estimation 75
4.6 Results 80
4.7 Conclusion 101

CHAPTER 5

Modal analysis of a spread single bone cell using the Finite Element Method ... 103

5.1 Introduction 103
5.2 Modeling 105
5.3 Modal analysis 110
5.4 Results 111
5.5 Discussion and conclusion 115

CHAPTER 6

Conclusion and future work 118
References 123
APPENDIX A 129
APPENDIX B 143
APPENDIX C 150
APPENDIX D 152
VITA 164

List of Tables

Table 2.1 Physical Parameters of the subjects 15
Table 3.1 Linear polynomial model structures. 39
Table 3.2 Black box system identification results (Subject # 16)..... 45
Table 4.1 The constants of system. 59
Table 4.2 The range of parameters for sensitivity analysis. 70
Table 5.1 Utilized material properties in cell modeling. 109
Table 5.2 Material properties of each cellular component. 109
Table A.1 Black box system identification results (Subject # 2)..... 134
Table A.2 Black box system identification results (Subject # 3)..... 135
Table A.3 Black box system identification results (Subject # 4)..... 136
Table A.4 Black box system identification results (Subject # 5)..... 137
Table A.5 Black box system identification results (Subject # 6)..... 138
Table A.6 Black box system identification results (Subject # 7)..... 139
Table A.7 Black box system identification results (Subject # 8)..... 140
Table A.8 Black box system identification results (Subject # 9)..... 141
Table A.9 Black box system identification results (Subject # 10)..... 142

List of Figures

Figure 1.1 Schematic representation of the plantar aponeurosis and the long plantar ligament [1]....4
Figure 1.2 Talocrural, talcocalcaneal, and midtarsal joint [2]. 5
Figure 1.3 Arches of the foot [3]. 6
Figure 1.4 A system with output *y*, and input *u*, measured disturbance *w*, and unmeasured disturbance *v* [8, 9]. 8
Figure 1.5 General procedure of System Identification.....9
Figure 2.1. The schematic of experiment setup. 17
Figure 2.2. Midstance (a), plantarflexion with 10 degree (b), and dorsiflexion with 10 degree (c). 18
Figure 2.3. MB transmissibility and phase in three mass cases for all subjects. 20
Figure 2.4. TB transmissibility and phase in three mass cases for all subjects. 21
Figure 2.5: The mean transmissibility and phase for MB, TB, and TM in three mass cases. Vertical arrows show the observed resonance frequencies. 23
Figure 2.6. MB transmissibility and phase in three posture cases for all subjects. 25
Figure 2.7. TB transmissibility and phase in three posture cases for all subjects....26
Figure 2.8. The mean transmissibility and phase for the MB, TB, and TM in three postures.....27
Figure 2.9. A single degree of freedom system. 27
Figure 2.10 Transmissibility contour lines of a single degree of freedom model with base excitation. 28
Figure 3.1 The procedure for system identification [8, 9]. 37
Figure 3.2 Structure of a black box model with two transfer functions [8, 9].....38
Figure 3.3 An example of black box system identification results at 10 Hz (subject # 16). 46
Figure 3.4 An example of black box system identification results at 15 Hz (subject # 16). 47
Figure 3.5 An example of black box system identification results at 20 Hz (subject # 16). 48
Figure 3.6 An example of black box system identification results at 25 Hz (subject # 16). 49
Figure 4.1 The simplified biomechanical models of foot ((a) [36] and (b) [37]). 56
Figure 4.2 The model of the foot and ankle structure (a) 3d model [53], (b) geometry, and (c) dynamic properties.....58
Figure 4.3 The relative sensitivity of parameters.....71
Figure 4.4 Two degrees of freedom model with linear springs and nonlinear damping.73
Figure 4.5 The process of the parameter estimation [9]. 76

Figure 4.6 The estimated results according to the applied mass at 10 Hz (Subject # 16). 81
Figure 4.7 The estimated results according to the applied mass at 15 Hz (Subject # 16). 82
Figure 4.8 The estimated results according to the applied mass at 20 Hz (Subject # 16). 83
Figure 4.9 The estimated results according to the applied mass at 25 Hz (Subject # 16). 84
Figure 4.10 The estimated results according to the applied mass at 30 Hz (Subject # 16). 85
Figure 4.11 The estimated results according to the applied mass at 35 Hz (Subject # 16). 86
Figure 4.12 The estimated results according to the applied mass at 40 Hz (Subject # 16). 87
Figure 4.13 The estimated results according to the applied mass at 45 Hz (Subject # 16). 88
Figure 4.14 The estimated results according to the applied mass at 50 Hz (Subject # 16). 89
Figure 4.15 Hysteresis behavior (force vs. displacement plot) of the estimated model without an extra mass. 92
Figure 4.16 Hysteresis behavior (force vs. displacement plot) of the estimated model with 2.3 kg mass. 93
Figure 4.17 Hysteresis behavior (force vs. displacement plot) of the estimated model with 4.5 kg mass. 94
Figure 4.18 The mean value of the spring constants (k_T) of the talocrural joint. 96
Figure 4.19 The mean value of the damping constants (c_{11}) of the talocrural joint..... 96
Figure 4.20 The mean value of the damping constants (c_{12}) of the talocrural joint..... 97
Figure 4.21 The mean value of the damping constants (c_{13}) of the talocrural joint..... 97
Figure 4.22 The mean value of the spring constants (k_F) of the foot fat pad. 98
Figure 4.23 The mean value of the damping constants (c_{21}) of the foot fat pad. 99
Figure 4.24 The mean value of the damping constants (c_{22}) of the foot fat pad. 100
Figure 4.25 The mean value of the damping constants (c_{23}) of the foot fat pad. 100
Figure 5.1 Culturing cells (a) various shapes of cells (b) ellipsoid shape of cells [76] (c) cross section of a cell [77]. 106
Figure 5.2 The simplified ellipsoid dome model of a cell. 106
Figure 5.3 The four types of ellipsoidal dome shape models. 107

Figure 5.4 A spread bone cell model in culturing condition (a) an example (100×40 μm) of three-dimensional model, and (b) an example of the finite element mesh model. 109
Figure 5.5 The modal analysis results for 135×30 μm with10 μm height and 100 Pa Young's modulus shape..... 112
Figure 5.6 The modal analysis results for 100×40 μm with10 μm height and 100 Pa Young's modulus shape..... 112
Figure 5.7 The modal analysis results for 80×50 μm with10 μm height and 100 Pa Young's modulus shape..... 113
Figure 5.8 The modal analysis results for 67×60 μm with10 μm height and 100 Pa Young's modulus shape..... 113
Figure 5.9 The natural frequencies of an adhered cell model in the function of spread shapes..... 114
Figure 5.10 The natural frequencies of an adhered cell model in the function of the elastic modulus. 115
Figure 5.11 The calculated first natural frequency as the function of elastic modulus.116
Figure A.1 An example of black box system identification results at 30 Hz (subject # 16) 129
Figure A.2 An example of black box system identification results at 35 Hz (subject # 16) 130
Figure A.3 An example of black box system identification results at 40 Hz (subject # 16) 131
Figure A.4 An example of black box system identification results at 45 Hz (subject # 16) 132
Figure A.5 An example of black box system identification results at 50 Hz (subject # 16) 133
Figure C.1 The relative sensitivity of parameters (30 cases)..... 151
Figure D.1 The distribution of the estimated parameters for without an extra mass.. 155
Figure D.2 The distribution of the estimated parameters for with 2.3 kg mass..... 159
Figure D.3 The distribution of the estimated parameters for with 4.5 kg mass..... 163

ABSTRACT

Transfer of the external loading such as shock or vibration to whole body could cause harmful or beneficial effects, depending on its nature. Two contradicting effects were investigated with macro and micro scale. In macro scale, the vibration absorbing capability of the human foot and ankle system (FAS) was investigated as the starting point of the whole body vibration using experimental method (transmissibility and phase delay measurement) and a model development. For biological cells, Finite Element modeling was utilized for modal analysis of an adherent cell in micro scale.

Vibration transfer characteristics of the FAS have been studied under vertical sinusoidal vibration (10-50 Hz with 5 Hz increments and 17.9 m/s^2 (peak to peak)) as a function of the external mass and foot and ankle postures. The results showed that the FAS played an important role in vibration transmission since the transmissibility of the FAS was dominant in lower leg. It was also found that the applied mass made the system stiffer and less damping, and the increase of the applied mass led to the increase of the resonant frequency from 20 to 30-40 Hz. This result explains that the overweight or obese persons can get more vibration transmission to the whole body when they are exposed to higher frequency (30-40 Hz). Furthermore, it supports that the resonant frequency of overweight or obese persons is similar to a major frequency range of heel strike, and overweight and obesity could be a potential injurious effect.

As the beginning step of a model development, system identification based on black box models (linear polynomial structures and state-space models) was utilized for understanding the transfer function on the basis of the acceleration measurement data of the foot and ankle exposed to vertical excitation. The identification of black box models

showed good estimation results (60-98 %). The fitting error of the lower frequency (10 and 15 Hz regardless of the applied mass conditions) was observed because of nonlinear behavior of the viscoelastic material of the foot and ankle system. The identified state-space model gave the guide for order selection (2-8) of the grey box model in the next step.

The dynamic model of the foot and ankle exposed to vertical vibrations has been developed by deriving analytical dynamic equations that include viscoelastic material properties. Using parameter sensitivity analysis with respect to the states, complex derived equations were simplified as a two degrees of freedom model with linear spring and nonlinear damping at the fat pad and talocrural joint. Unknown parameters of the dynamic model were estimated by the parameter estimation method (optimization algorithm) by fitting the experimental data. The estimated parameters demonstrated that the fat pad dissipated more energy of the applied vibration than the talocrural joint and the applied mass and frequency increase affected the stiffness increase at the ankle joint and fat pad. The derived model is expected to be utilized for estimating some other frequencies and loading conditions.

An adherent single cell was modeled as a simple dome to extract the natural frequency and mode shapes of a cell in the culturing environment using Finite Element modal analysis. Simulation results showed that the adhered cell shape did not affect the modal analysis results. However the natural frequency was increased proportionally to the increase in Young's modulus. It is supposed that the natural frequency of cells (18-25 Hz) is closely related to the optimal vibration range (20-60 Hz) for bone growth.

CHAPTER 1

Introduction

1.1 Motivation

The effect of vibration on the human body can be classified as being good or bad similar to the examples of vibration physics; sound of instrumentation would be a good vibration, and car or machine vibration would be an example of bad vibration. Human beings are always exposed to external force environment intentionally or involuntarily such as various vibrations or shocks during routine life. The effect of this external force to the human body has been studied for more than 50 years from the point of view of the disadvantages. Many studies described the dynamic responses of body vibration with measuring transmission at the specific location of body and explained the relationship between vibration and harmful effects. Recently, the favorable effect of human body vibration was introduced by whole body vibration therapy or dynamic vibration therapy. It has been utilized to enhance bone mineral density and muscle strength.

The foot and ankle system is an important body part as the starting location of whole body vibration. It is necessary to study how the human body responds to the external force and how to model its dynamic response. The study of biodynamic response of the foot and ankle system will be helpful to understand the adverse and favorable effects of whole body vibration. In addition, the view of whole body vibration could extend to micro scale such as the vibration of cells since the growth of bone cells is closely related to the external force environment. These macro and micro studies are expected be broaden the knowledge of whole body vibration.

1.2 Overview of the structure and function of the foot and ankle [1, 2]

The foot and ankle joints consist of 24 bones, 33 joints, and a number of muscles, tendons, and ligaments. The structure of the foot and ankle can be divided into three parts: the forefoot, the midfoot, and the hindfoot (Figure 1.1). The forefoot is the front part of the foot that consists of five phalanges and five metatarsal bones. The midfoot has the cuboid, navicular, and three cuneiforms at the center of the foot. Two bones, the calcaneus and talus in the rear foot compose the hindfoot. These three parts create the arch of the foot; the head of metatarsals and the bottom of the calcaneus are connected with a broad and thick tissue, which is called the plantar aponeurosis.

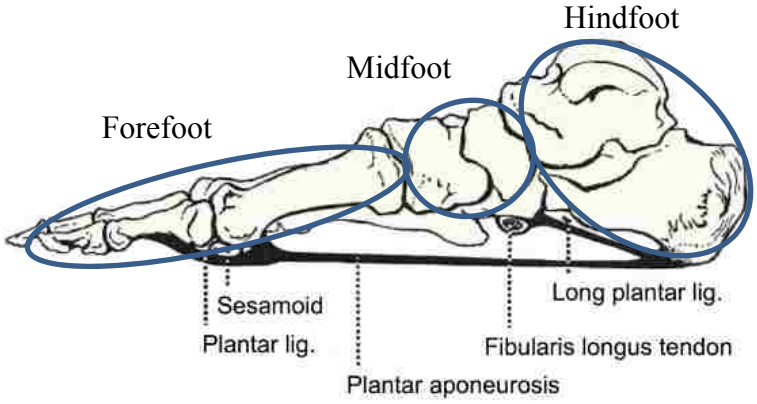

Figure 1.1 Schematic representation of the plantar aponeurosis and the long plantar ligament [1].

There are three main articular joints in the human foot and ankle: the talocrural (ankle), subtalar (talocalcaneal), and midtarsal (transverse tarsal) (Figure 1.2). The talocrural joint is located between the talus and tibia and between the fibula and tibia, and its axis responsible for the rotation of the foot such as plantar flexion, dorsiflexion, abduction, and adduction. The talocalcaneal joint, located between the talus and

calcaneus, has an axis from the bottom of calcaneus to the front talus and allows the supination and pronation. The midtarsal joint is composed of two articulations: the articulation between the talus and navicular and the articulation between the calcaneus and cuboid.

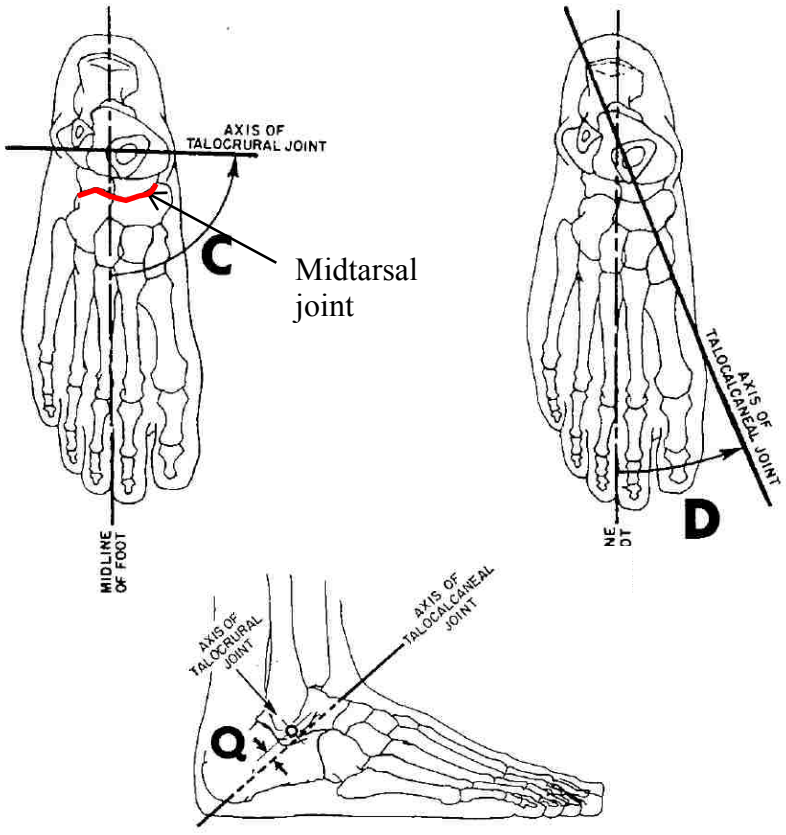

Figure 1.2 Talocrural, talcocalcaneal, and midtarsal joint [2].

The foot has three arches: the medial longitudinal arch, lateral longitudinal arch, and transverse arch (Figure 1.3). These arches are maintained by the shape of the tarsal and metatarsal bones, ligaments and plantar fascia, and they contribute to support and shock absorption. According to the height of the medial longitudinal arch, the foot can be rigid or flexible, and it is classified as a normal arch foot, a high-arched foot (pes

cavus), and a flat-arched foot (pes planus). High-arched feet have poor shock absorbing capability because they are generally more rigid structures. Low-arched feet have flexible structural characteristics, which can produce an excessive pronation.

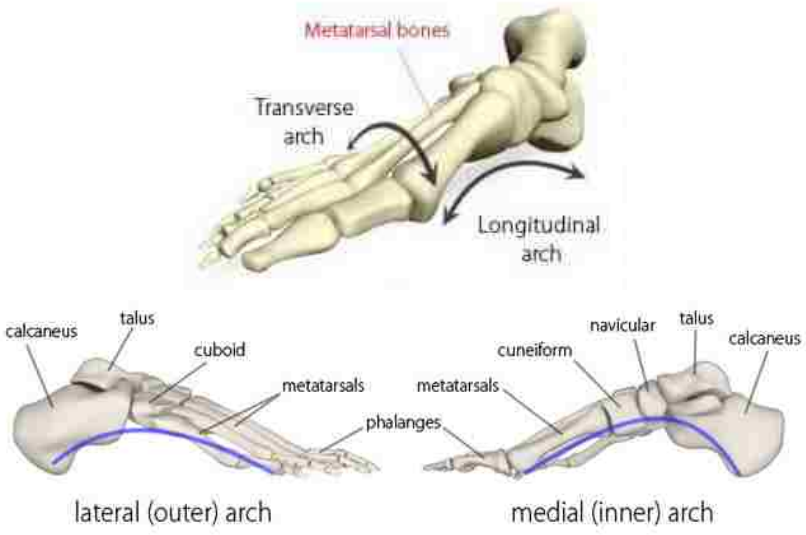

Figure 1.3 Arches of the foot [3].

1.3 Overview of the effect of vibration on human [4]

Since humans use more powerful tools in work environments, these tools tend to transfer more vibration during those cases. As a result, vibration is naturally dissipated to environments and some of the vibrations are transmitted to the body. People experience the general case of whole body vibration during routine life such as riding transportation system. The external vibration generated from shaking conditions transfers through the support point of a sitting or standing human to the whole body. In the case of the standing condition, the external vibration is transmitted to the whole body through the foot and ankle as the starting portion of human body.

The perception of discomfort about vibration depends on the magnitude and frequency of vibration. However, there are some severe conditions unlike the vibration from routine life. For example, when human body is exposed to vibration from severe working conditions such as driving an industrial vehicle or agricultural machinery, and working with heavy machinery, it could result in a health risk and musculoskeletal disorder at specific joints.

In contrast to the adverse effect of whole body vibration, whole body vibration therapy (dynamic vibration therapy) is utilized in the fitness and health industry for beauty, physical therapy, rehabilitation, and so on. The current whole body vibration equipment has a vibrating platform as the vibration source. The vibration type is controlled by the frequency, amplitude, and the direction of the vibrating platform. The vibrating platform types have different features depending on the purpose of whole body vibration: generating stretch-reflex contraction in muscle fibers for the positions' training program, working at various speeds for physiotherapy, working at low speed/amplitude for preventing osteoporosis, improving blood circulation etc. [5, 6, 7].

Although there are benefits in the whole body vibration therapy, it is still considered controversial because of the adverse effects of human body vibration as shown in the previous paragraph. Thus, it is necessary to understand both favorable and adverse effects of whole body vibration.

1.4 Overview of the system identification [8, 9]

System identification is a theory to build mathematical models based on the observed data of systems through the experiments. A system measures an observable

output when it is affected by the external signal as input (Figure 1.4). The application of system identification is broad from mechanical to biological systems.

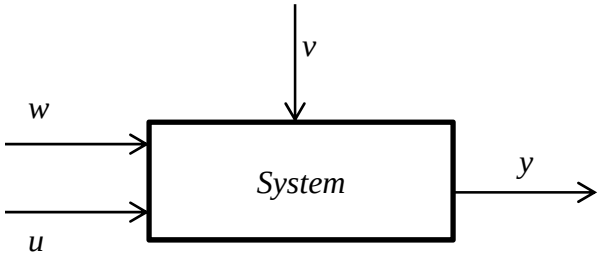

Figure 1.4 A system with output *y*, and input *u*, measured disturbance *w*, and unmeasured disturbance *v* [8, 9].

There are two approaches to identify the system: black box modeling and grey box modeling. Black box modeling is able to define the model form and the coefficient of the extracted model using measured input and output without building the exact mathematical model. However, if the physical insight and knowledge are available, and the derivation of the mathematical model is possible, grey box model can estimate the unknown physical parameters in the derived equation with measured input and output.

The general procedure of system identification is shown in Figure 1.5. The process is performed in an iterative way and trial and error method. At first, an experiment is designed for the selected model, and the measured data is collected. The collected data is evaluated and preprocessed for the next step. Then, the type of model is chosen (black box model) or derived (grey box model) with trial and error. The selected model is identified, or unknown parameters of the derived model are estimated. The identified system is evaluated with the observed data. If the evaluation is not satisfied with the defined criterion, the procedure of system identification is going to the first step for a new iteration.

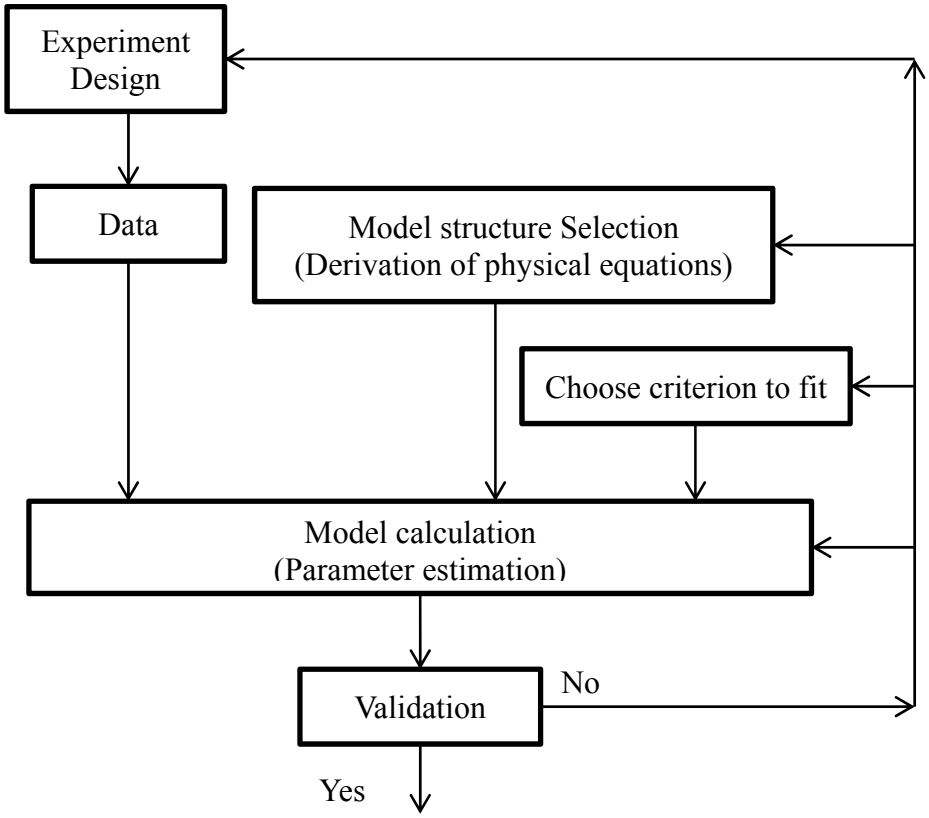

Figure 1.5 General procedure of System Identification.

1.5 Organization of Thesis

This thesis consists of two parts of studies with five chapters. The first part described the dynamic characteristics of the foot and ankle structure exposed to vertical vibration from Chapter 2 to 5.

Chapter 2 reports the dynamic response of the human foot and ankle to vertical vibration with the transmissibility measurement between the Base and Medial Malleolus, between the Base and Tibial Tuberosity, and between the Medial Malleolus and Tibial Tuberosity.

Chapter 3 reports the foot and ankle system identification with black box models based on the experimental results.

Chapter 4 reports the development of the foot and ankle system exposed to vertical vibration and estimation of unknown parameters in the suggested models.

In the second part, the cell adhered on the culturing plate was investigated to understand the dynamic characteristics of an adhered cell in the view of micro scale.

Chapter 5 reports natural frequencies and mode shapes of a single cell adhered to the cell culture plate using Finite Element modal analysis.

CHAPTER 2

Dynamic response of human foot and ankle to vertical vibration

2.1 Introduction

The human musculoskeletal system is continuously exposed to shock and vibration generated from walking, running, jumping, living and working environments. Those external loads are transferred to the whole body through the interference between parts of human body. They are attenuated by natural shock absorbers such as soft tissues and bones. During this process, the external mechanical loading induces internal forces on the human musculoskeletal system and sometimes these forces cause detrimental effects such as injury or disease. The shock and vibration absorbing capability of the human musculoskeletal system is an important function since it is closely associated to the possibility of the above mentioned adverse effects.

The relationship between the external loading and their harmful effects has been studied extensively [10-14]. Folman *et al.* [10] examined the frequency of the cyclic impact loading resulting from the heel strike during normal walking. It was concluded that the impact force generated at heel strike might cause the fatigue failure of the musculoskeletal system. Holt *et al.* [11] investigated the shock transmission at the joints and segments during load carriage and showed the potentially injurious effects during load carriage at higher walking speed. Radin *et al.* [12-14] applied the repetitive impulse loading to the animal joint and studied its effect on cartilage. They found that the applied loading was an essential factor in splitting, wearing and finally preceding to the articular

cartilage degeneration and osteoarthritis. Voloshin and Wosk [15] established that the impact waves generated by repetitive loading during gait were propagated through the whole body and were attenuated by the natural shock absorbers such as soft tissues and bones. It was shown that the low back pain correlated with the reduced shock attenuation capacity of human musculoskeletal system [15]. Shock absorbing capacity during locomotion was explored at various locations of the human musculoskeletal system (knee, medial femoral condyle, and forehead) of young and healthy subjects [16].

Similarly to the impact loading, the transmission of vibration through the whole body may produce harmful effects on the human musculoskeletal system. The whole body vibration studies have focused on investigating the dynamic response and the natural frequency of specific parts of the human body such as pelvis, spinal column, hand, shoulder, neck, and head while the whole human musculoskeletal system was exposed to various frequencies [17-23]. Panjabi *et al.* [17] measured the transmissibility of spinal columns (the lumbar vertebrae and sacrum). The measured average resonance frequency of the lumbar vertebrae was 4.4 Hz. It was expected that those results could help reduce the possibility of the harmful effects by controlling the input vibration. Matsumoto and Griffin [18, 19] measured the dynamic response of seated and standing subjects at the thoracic vertebras, the lumbar vertebras, the pelvis, the iliac crests, and the knee under the vertical whole body vibration. They demonstrated the upper body motion of the seated human body at the principal resonance frequency according to the input vibration and elucidated that a small bending at the lumbar spine and the lower thoracic spine might cause the maximum translation motion of the spine [18]. The standing human body exposed to vertical vibration had been studied to evaluate the influence of the leg posture

and the vibration amplitude on the human body vibration transfer [19]. It was shown that the peak in the apparent mass in the standing case was similar to the seated case. The leg bent posture and the one leg posture showed the attenuated vibration transmission at higher frequencies. The decrease in the resonance frequency of normal posture was observed as the vibration magnitude was increased. Harazin and Grzesik [20] found that the ranges of resonant frequency and the transmissibility were dependent on standing posture during whole body vibration. Paddan and Griffin [21] reviewed the transmissibility of translational vibration between the seat and the subjects' head according to the direction of input vibration and provided the median value of the transmissibility in each direction. Hinz and Seidel [22] investigated the characteristics of the dynamic response at head, acromion, and upper trunk during whole body vibration. At the resonance frequencies, the amplitudes of maximum accelerations were significantly higher than that of minimum accelerations. The nonlinear dynamic response of human body was observed. Mansfield *et al.* [23] measured the apparent mass and absorbed power when the human body was exposed to the random vibration, the repeated shocks, and combination of these. They found out that the type of the applied input did not influence the dynamic response of the human body. In addition, it was found that resonance frequencies decreased with the increase of vibration magnitude (softening effect) and shock stimuli resulted in higher resonance frequencies (stiffening effect). They also showed that the effect of the shock was more severe than the random vibration on the basis of the total absorbed power.

However few studies related to the dynamic response to the external vibration of the Foot and Ankle System (FAS) measured the natural frequency, the stiffness, and the

damping coefficients of the muscle and soft tissue of the lower limbs [24, 25] even though the FAS is the starting point of the whole body vibration. Aruin and Zatsiorsky [24] measured the stiffness and damping coefficient of the ankle joint muscle with vibration and impact test. The stiffness and damping constant were respectively $2.67\pm0.48 \times 10^4$ $N\cdot m^{-1}$and 811 ± 201 $N\cdot s\cdot m^{-1}$ for impact case and the $1.49\pm0.35 \times 10^4$ $N\cdot m^{-1}$ and 430 ± 36 $N\cdot s\cdot m^{-1}$ for vibration case. The frequency response function of the human soleus muscle was measured by Bawa and Stein [25]. They showed that the human soleus muscle was similar to the second order low pass filter and the natural frequency and damping ratio were varied according to the angle of the ankle.

The purpose of the present study was to investigate a structural dynamic response of the FAS exposed to the vertical vibration. Similarly to some of the whole body vibration studies, the transmissibility from the driving point to the Medial Malleolus (MM) and the Tibial Tuberosity (TT) were measured using the vertical sinusoidal vibration input. The resonance frequencies were identified for each case. In addition, the influence of the external static load applied at the lower leg and FAS postures, such as the plantarflexion and the dorsiflexion, on the dynamic characteristics of the FAS were investigated.

2.2 Methods

2.2.1 Subjects

The biodynamic response of human body is usually described using the driving point mechanical impedance, the apparent mass or the transmissibility [26]. In this study, the transmissibility was utilized to describe the vibration transmission through the ankle

and foot system. The experimental procedure for human subjects was followed the regulations of Lehigh University's Office of Institutional Research.

Table 2.1 Physical Parameters of the subjects

Subjects	Age (yr)	Height (m)	Mass (kg)
1	21	1.70	50.8
2	22	1.75	77.11
3	26	1.75	79.38
4	18	1.60	63.50
5	25	1.75	76.66
6	24	1.60	45.36
7	23	1.65	54.43
8	20	1.75	70.31
9	20	1.83	70.31
10	22	1.75	77.11
11	23	1.83	81.65
12	27	1.83	88.00
13	22	1.63	61.23
14	21	1.83	79.38
15	22	1.70	74.84
16	27	1.85	72.57
17	22	1.78	61.23
18	22	1.88	72.57
19	20	1.78	71.21
20	20	1.70	86.18
Mean	22.30	1.75	70.70
STD	2.43	0.08	11.44
Min	18	1.60	45.36
Max	27	1.88	86.18

Twenty healthy male and female subjects with no medical history of severe or permanent ankle injury or ankle arthritis were recruited with the approval of Lehigh University Institutional Review Board. The subjects mean age was 22.4 year old with the mean height and mass of 1.75 m and 70.7 kg, respectively (Table 2.1). The subjects were asked to wear short pants to prevent any disturbances during the test. Prior to the test the

procedure was explained to each subject and they were asked if there was any inconvenience. All subjects signed the informed consent form.

2.2.2 Experimental set-up

The harmonic vibration test (a single frequency excitation at a time) in the range of frequencies from 10 to 50 Hz was used to characterize the transmissibility of the FAS. The subjects were sitting in upright position on a chair placed on the top of a table next to a 1200 pound-force shaker table connected with an ultra-high-powered, precision mono amplifier[1]. The subject's lower leg was placed on a rigid platform attached to the shaker table. The subject was asked to keep his foot on the flat platform in a position similar to free standing. The subject's foot and lower leg were set to be perpendicular to one another, as well as the lower leg and the thigh (Figure 2.1).

The sinusoidal input vibration was controlled by a frequency generator. The input acceleration was measured by a piezoelectric accelerometer (PCB Piezotronics, Inc., type 308B) mounted on the plate attached to the shaker table. The skin mounted accelerometer method was utilized to measure the output accelerations [15]. Two piezoelectric accelerometers (PCB Piezotronics, Inc., type 303A) were placed externally on the MM and TT; they were secured by Velcro straps. Accelerometers were connected to the data acquisition device (Measurement Computing, PMD-1208FS) and raw voltages were collected by a computer. As was shown by several studies [15, 16], the effect of the skin under the accelerometer was negligible since the utilized accelerometer had the low mass of 2.36 g.

[1] Crown Macro-Tech 10000

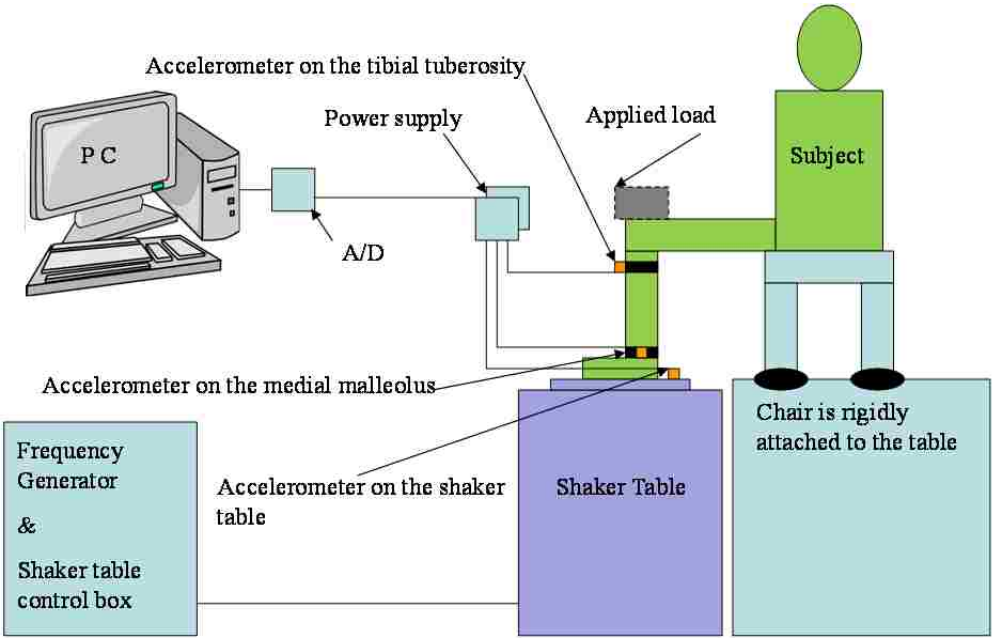

Figure 2.1. The schematic of experiment setup.

The frequency range was selected to be in a range of 10 to 50 Hz with 5 Hz increments. The mean amplitude of peak to peak acceleration was selected to be 17.9 m/s^2 to assure absence of the free falling effect. The acceleration for each frequency case was measured with at 1 kHz sampling rate for 10 seconds. Three different conditions (no extra mass, with added 2.3 kg mass, and 4.5 kg mass) and three postures of the FAS (the midstance, plantarflexion, and dorsiflexion) were considered to characterize the dynamic behavior of the FAS. Additional masses of 2.3 and 4.5 kg were applied to the top of the knee (Figure 2.1). Because the plantarflexion and the dorsiflexion are dependent on the subject's foot length (from the head of metatarsal to the heel pad), 10 degrees, which is based on the range of motion average, were applied at each of the both cases (Figure 2.2). For plantarflexion case, the heads of metatarsals and phalanges are placed on the plate and the height of the heel was raised with plantarflexion (10°). For dorsiflexion case, the

heel pad was contacted to the flat plate and the forefoot was kept in the status of dorsiflexion (10°).

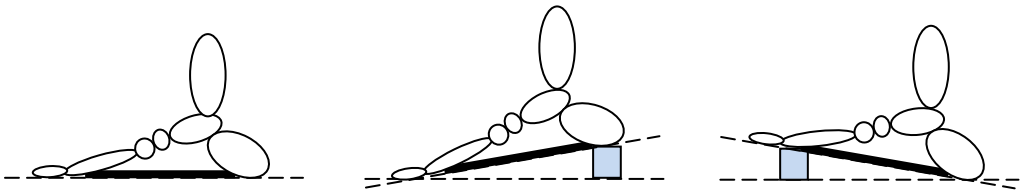

Figure 2.2. Midstance (a), plantarflexion with 10 degree (b), and dorsiflexion with 10 degree (c).

2.2.3 Data Analysis

The high frequency noise was reduced by the 5th order low pass filter over 100 Hz. The peak to peak method was utilized to calculate the transmissibility between the input and the output. It was defined as the ratio of the input ($Accel_{in}$) and the output acceleration ($Accel_{out}$) of the MM, and the TT.

$$Transmissibility\left(\frac{m/s^2}{m/s^2}\right) = \frac{Accel_{out}}{Accel_{in}} \tag{2.1}$$

The phase shift was calculated using the cross spectral density ($\hat{Z}_{XY}(n)$) that uses Fourier transform of the Cross-covariance function ($\hat{C}_{XY}(k)$) to show the relationship between two signals.

$$\hat{Z}_{XY}(n) = \frac{1}{N}\sum_{k=1}^{N}\hat{C}_{XY}(k\Delta t)e^{-jn\omega_0 k\Delta t} \tag{2.2}$$

$$\hat{C}_{XY}(k) = \frac{1}{N}\sum_{i=0}^{N-k}X(i)Y(i+k) \tag{2.3}$$

where X is the input, and Y is the output, ω_0 is the fundamental frequency, n is an integer multiplier of ω_0, N is number data points, k is the discrete variable, and Δt is the time interval [27].

2.3 Results

2.3.1 Effect of the load on transmissibility and phase

The transmissibility and phase between the base and MM (MB), between the base and TT (TB) as a function of loading conditions are shown in Figures 2.3 and 2.4 for all subjects. These plots show spline fit to the actual experimental data that was acquired at 5 Hz intervals. The heavy line is an average of all subjects. The transmissibility results below 10 Hz were not available in this study due to the limitations of the experimental setup. However, on the basis of transmissibility trend, the principal resonant frequency could be assumed to be below 10 Hz for every case. This assumption is supported by studies that measured the vibration transmissibility at the ankle and knee [18-20, 24, 25, 28-30]. Even though there is a large inter-subject variance in dynamic response, the general shape and the frequency of the transmissibility peak has a similar trend between subjects for each condition. A broad peak of transmissibility, that is a resonance frequency, was observed above 10 Hz in every case.

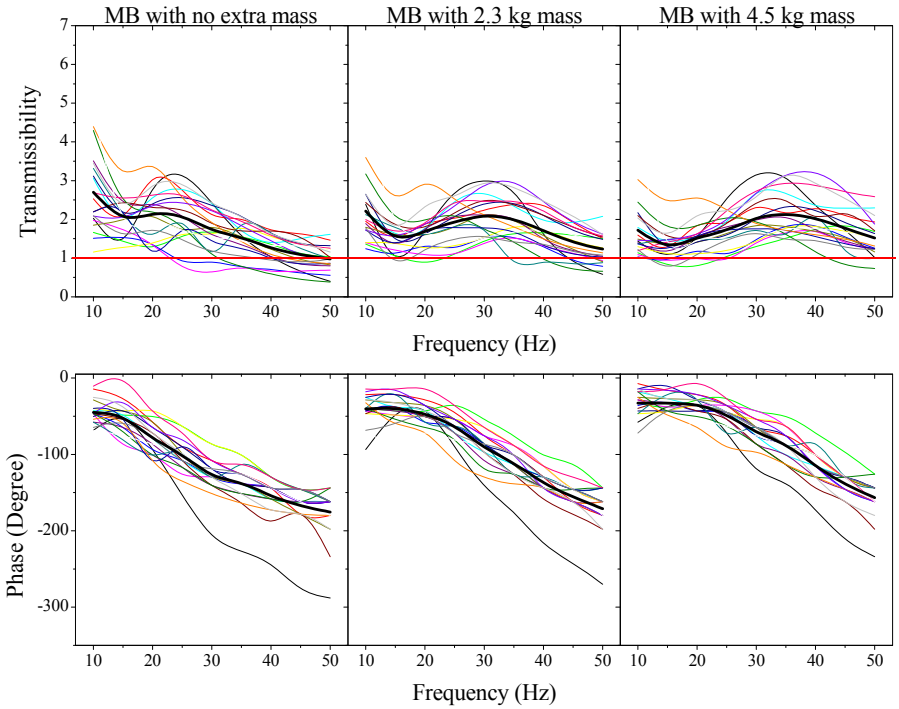

Figure 2.3. MB transmissibility and phase in three mass cases for all subjects.

While some subjects showed unclear peak, the observed resonance frequencies of most subjects for the MB with no extra mass are varied between 20 to 35 Hz, and they are increased to 25-35 and 30-40, respectively, for the cases of 2.3 and 4.5 kg added mass (Figure 2.3). The transmissibility for MB is larger than unity over all frequencies for almost all subjects and mass conditions. The phase lag for MB was increased as frequency was increased. It had a relatively large slope in the same frequency range where broad peaks of the transmissibility were observed.

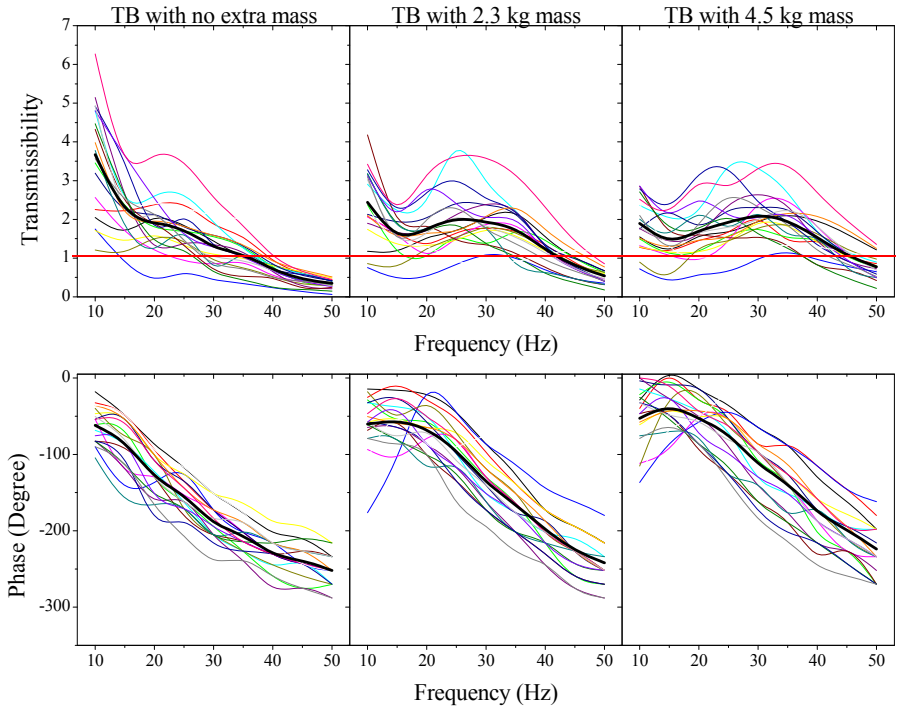

Figure 2.4. TB transmissibility and phase in three mass cases for all subjects.

With respect to TB, in several subjects a peak was shown at 20 and 25 Hz for the case of no extra mass, while both additional mass cases caused a broad peak around 20 to 40 Hz for all subjects (Figure 2.4). The variation of transmissibility magnitude for TB is larger at 10 Hz and near the observed resonance frequency comparing with higher frequencies around 40-50 Hz. The transmissibility for TB is less than one above 30, 35, and 40 Hz, respectively, for no extra mass, 2.3, and 4.5 kg mass. Similarly to the phase delay for MB, the phase delay for TB was increased with increase in the frequency.

The mean transmissibility and phase delay for twenty subjects for MB, TB, and TM (between the MM and TT) were calculated to analyze the influence of the applied mass (Figure 2.5). Statistical tests ($p < 0.05$) were utilized to identify the peak in

transmissibility and compare the transmissibility with unity; paired t-test was used for mean values of peaks, and one-sample t-test is for the unity check. Additionally, one-way analysis of variance ($p < 0.05$) was used for the comparisons between loading conditions. The transmissibility for the MB without additional mass decreased with the increase of frequency. It was greater than unity below 40 Hz and close to unity at 45 and 50 Hz. It showed a plateau at 15-25 Hz range since the mean transmissibility at 20 Hz is not significantly greater than that at 15 and 25 Hz, but it was significantly greater than in the 30 Hz case.

The application of external mass caused the observed resonance frequency for MB shift to higher values, from 15-25 Hz to around 30-40 Hz. In 2.3 kg case, the amplitude at 30 Hz was statistically greater than that at 25 and 40 Hz, but it was not significantly greater than that at 35 Hz (Figure 2.5). As a result, the observed resonance frequency in the 2.3 kg case is located at 30-35 Hz range. The resonance for 4.5 kg mass occurred at 35-40 Hz range; the amplitude at 35 Hz was statistically greater than the value at 30 Hz and 45 Hz and it was not significantly greater compared with the amplitude at 40 Hz. For both loading cases, the transmissibility is larger than unity at all frequencies.

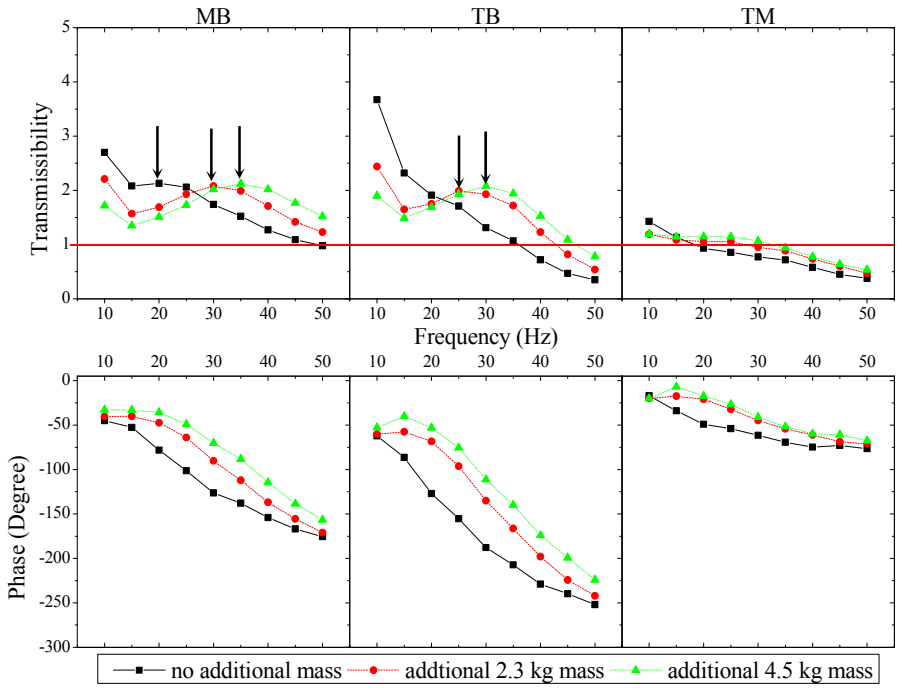

Figure 2.5: The mean transmissibility and phase for MB, TB, and TM in three mass cases. Vertical arrows show the observed resonance frequencies.

The transmissibility for TB is significantly different between three mass cases at 10 Hz. For TB, the transmissibility without extra mass gradually decreased without a peak or flat part, and a broad peak of the transmissibility is located at 25 and 30 Hz for both cases of 2.3 and 4.5 kg added mass; for both masses, the amplitudes at 25 and 30 Hz were statistically greater than the values at 20 and 35 Hz (Figure 2.5). Two additional mass cases have similar amplitude in the range of 15 to 35 Hz since the difference between both cases is not significant in that range. The transmissibility for TB is less than unity below 40 Hz in no extra mass case, below 45 Hz for additional 2.3 kg mass, and at 50 Hz for additional 4.5 kg mass.

The TM transmissibility does not have a resonant peak and is below unity above 25 Hz for no extra mass and above 40 Hz for both cases with added mass (Figure 2.5). The transmissibility gradually decreased in no additional mass case but has a plateau from 10 to 25 Hz in the additional mass case.

The phase delay is naturally increased as the measuring point becomes farther away from the input point. The phase delay difference of both MB and TB between the no extra mass case and the additional mass case is gradually increased and it is maximum around 30-35 Hz, where peaks are observed as resonant frequencies, and then decreased again. The phase difference between applied mass groups was small at the lower (10-15 Hz) and higher frequency range (45-50 Hz), but it was larger in the mid frequency range (20-40 Hz). The average phase for all cases shows that the slope is the largest at the observed resonant frequency.

2.3.2 Effect of the posture on transmissibility and phase

The influence of the FAS posture on the transmissibility for MB and TB are shown in Figures 2.6 and 2.7. Even though some subjects show a peak of the transmissibility, each posture case has a similar trend and variation without a resonance frequency for both MB and TB. The variance of transmissibility is higher at lower frequencies and is decreased as the applied frequency is increased in every case.

The results for MB for three postures show that there is no clear peak in many subjects while broad peaks were observed at 20-35 Hz and 20-30 Hz, respectively, for plantarflexion and dorsiflexion in several subjects (Figure 2.6). The transmissibility for almost all subjects is larger than one. The frequencies, where the transmissibility for

subjects is below one, are 40 Hz for midstance and plantarflexion and 45 Hz for dorsiflexion. The dorsiflexion posture shows that some subjects have higher transmissibility for MB under 15 Hz than midstance and plantarflexion. The transmissibility for TB has a different trend at lower frequency for each posture; its variance is widely spread in the frequency below 30 Hz and then decreased when the frequency is increased (Figure 2.7). The phase delay is increased with the increase of the applied frequency. The variance of phase delay for MB is larger than that for TB above 20 Hz. Specially, the MB with plantarflexion shows the larger variance above 30 Hz frequency.

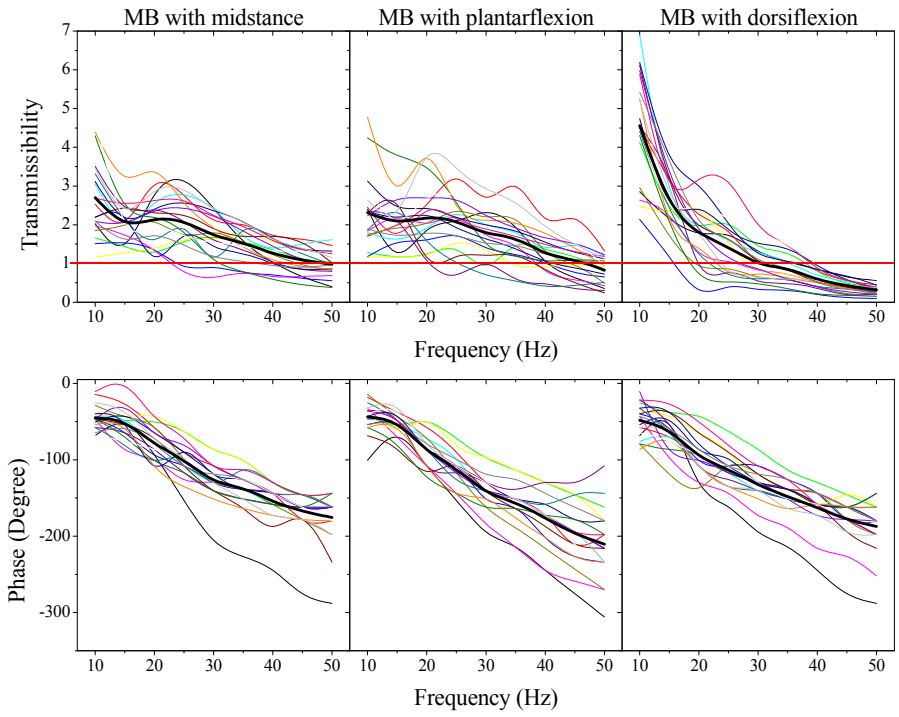

Figure 2.6. MB transmissibility and phase in three posture cases for all subjects.

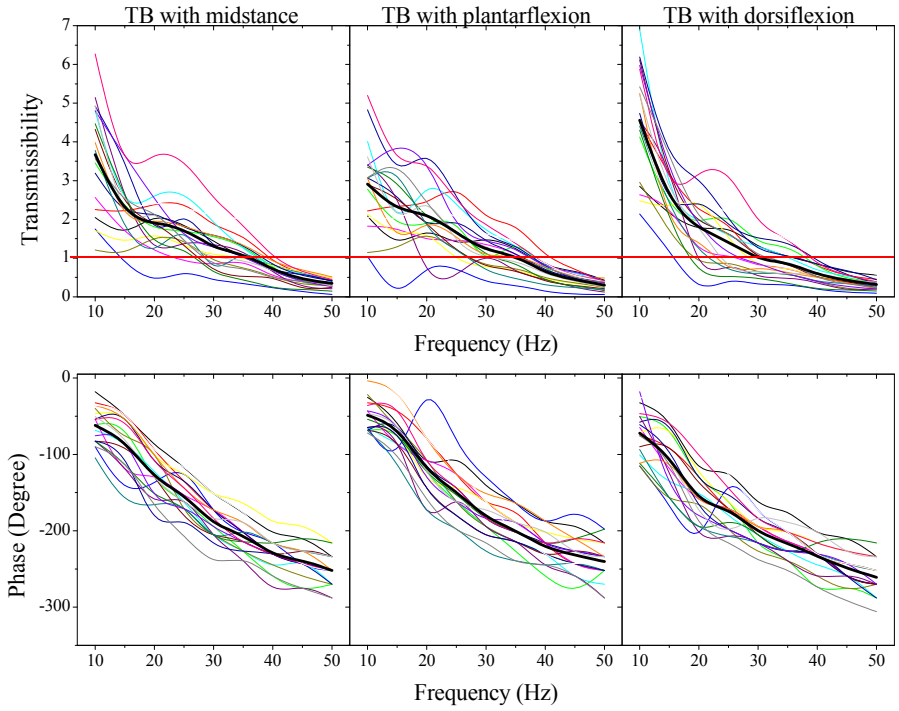

Figure 2.7. TB transmissibility and phase in three posture cases for all subjects.

The mean transmissibility and phase delay for three different postures for MB, TB, and TM are compared in Figure 2.8. The resonance frequency was not observed in dorsiflexion while plantarflexion showed a plateau at 15-25 Hz. The FAS posture affected the transmissibility only at 10 Hz for MB and TB. However, at other frequencies, the transmissibility for all postures for MB and TB were not significantly different. The transmissibility for TM was not significantly different at all frequencies. Only the transmissibility for the MB with all postures was close to unity or less at 50 Hz. For TB the transmissibility of all postures was decreased below unity above 40 Hz, and the transmissibility for TM is less than unity above 25 Hz. For MB, TB, and TM, the overall trend in each posture shows the phase delay increase with the frequency increase and similar trend each other except the case for TM with dorsiflexion.

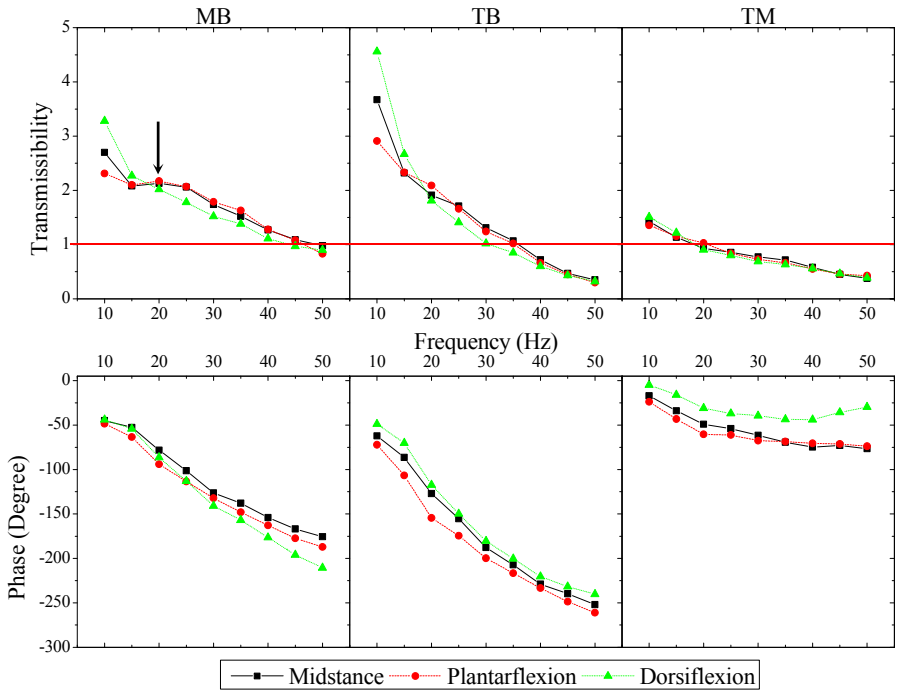

Figure 2.8. The mean transmissibility and phase for the MB, TB, and TM in three postures.

2.3.3 Transmissibility of single degree of freedom model

A single degree of freedom (SDOF) model with stiffness and damping was utilized to describe the transmissibility variance of the FAS (Figure 2.9).

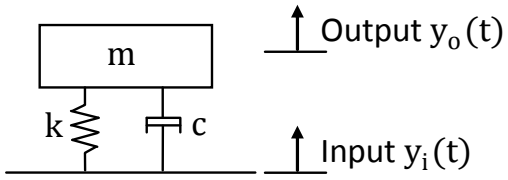

Figure 2.9. A single degree of freedom system.

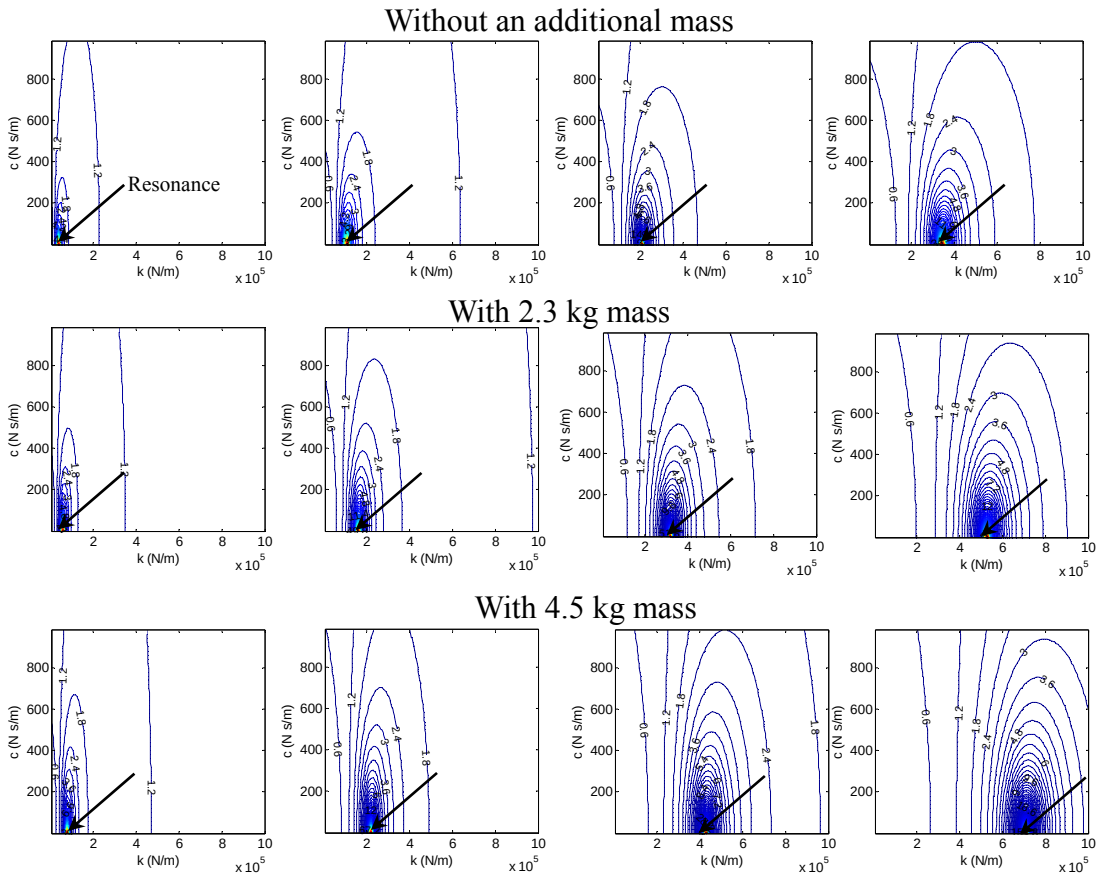

Figure 2.10 Transmissibility contour lines of a single degree of freedom model with base excitation.

The base is excited with a sinusoidal vibration and the mass of single degree of freedom mode represents the mass of the shank and foot. The equation of motion of this model is

$$m\ddot{y}_o(t)+c\left(\dot{y}_o(t)-\dot{y}_i(t)\right)+k\left(y_o(t)-y_i(t)\right)=0 \qquad (2.4)$$

where m is the mass of the foot and shank, y_i is the motion of the base, y_o is the motion of the mass relative to the internal reference frame, c is damping coefficient, and k is spring constant. The transmissibility (T) of displacement, velocity and acceleration are defined by

$$T = \left|\frac{y_o}{y_i}\right| = \left|\frac{\dot{y}_o}{\dot{y}_i}\right| = \left|\frac{\ddot{y}_o}{\ddot{y}_i}\right| = \sqrt{\frac{k^2 + (\omega c)^2}{(k - m\omega)^2 + (\omega c)^2}} \quad (2.5)$$

where ω is the circular frequency [31]. The mean mass of all subjects lower leg (m=4.3 kg) was calculated on the basis of anthropometry data [32]. For the additional mass case, 2.3 and 4.5 kg mass was added to the mean mass of the SDOF. The transmissibility of acceleration for ranges of the stiffness and damping for some frequencies is shown in Figure 2.10. For the measured transmissibility for MB and TB, Figure 2.10 can be utilized to find an approximate range for spring constant and damping coefficient of the FAS.

2.4 Discussion

This study measured the acceleration at the MM and the TT with three mass and three posture conditions when sinusoidal input vibration was applied to the bottom of the foot. Transmissibility and phase for MB, TB, and TM were calculated to analyze the effects of the applied mass and posture. The data below 10 Hz was not available in this study, but the principal resonance frequencies of every case are assumed to be below 10 Hz based on the observed trend. This inference is consistent with other studies shown the principle resonant frequency occurs below 10 Hz [18-20, 24, 25, 28-30]. The overall acceleration patterns at the MM and TT have very similar trend with a study that measured acceleration at the ankle and knee, although it used whole body vibration while standing [28].

For the MB transmissibility, a plateau was observed between 15 and 25 Hz for no extra mass case. This frequency is similar to the third resonant frequency (25-63 Hz) of

ankle which is observed by Harazin and Grzesi [20]. The observed here resonances are not exactly the same as their results since the limitations of experimental setup and the applied frequency increments did not allow for the frequency below and around 10 Hz to be measured. Also, the difference of experimental condition (sitting and standing) could cause the difference in the value of the third resonance.

Applied mass increased the resonance frequency from 15-25 to around 25-40 Hz. Due to additional mass, the heel pad and the articular cartilage between talus and tibia were compressed and stiffened; the foot arch structure also stiffened with the extended plantar fascia. This stiffening effect is closely related to the change of the resonance frequency since the resonance frequency for a SDOF model is proportional to the square root of stiffness and inversely proportional to the square root of mass. As shown in Figure 2.10, the increase in the transmissibility for the MB and TB at the higher frequency could have a resonance when the stiffness is increased more comparatively to the lower frequency.

The transmissibility for the MB and TB below 20 Hz decreased as the additional mass was applied to the system. It indicates that the added mass made the FAS stiffer and also more damped at the lower frequency in comparison with the case of no additional mass. This result is also related to the fact that the system becomes stiffer as the applied mass is increased, and the vibration is propagating faster and therefore, the phase shift is decreased. The transmissibility without extra mass is gradually decreased with frequency, while frequency was increased, for the additional mass cases it showed the resonance frequency at 30-40 Hz for MB and 25-30 Hz for TB.

The transmissibility for MB was larger than unity over all frequencies regardless of the applied mass, while the transmissibility for TM was decreased and was close to unity or less. Thus, it is clear that the major vibration transmission was fulfilled at the FAS in all frequencies and the foot and ankle joint played a major role to contribute to the resonance in the lower leg system. The transmissibility for TM, close to unity, means that it acts like a rigid body, because the shank has a long tibia bone. Over 35 Hz, the transmissibility for TM decreased below unity. This vibration at higher frequency might be absorbed by complex viscoelastic structures such as tissues, muscles, and tendons of the lower leg.

The postures of the FAS slightly influence the transmissibility results. The dorsiflexion made the FAS stiffen and less damping compared with midstance and platarflexion at 10 Hz. Between 25 and 40 Hz the midstance and plantarflexion showed similar transmissibility, but they are larger than that of the dorsiflexion. It means that the posture of dorsiflexion might be less stiff or more damped for the MB at 25-40 Hz.

2.5 Conclusion

The transmissibility for MB was larger than unity for all frequencies while the transmissibility for TM was close to unity or less than unity for each of the loading conditions. It means that the foot structure and ankle joint plays a major role in the vertical vibration transmission to the whole body. The applied mass increased the stiffness of the FAS, and there was an increase from 20 to 30-40 Hz in the observed resonant frequency with the load increase. Since the applied mass case is similar to the heavier system, these results indicate that overweight and obesity leads to the increase in

the stiffness and the resonant frequency of the FAS. The resonant frequency around 25-35 Hz is similar to the impact loading frequency at the heel strike during gait [16]. The applied postures did not show a resonance frequency and affect the transmissibility for MB, TB, and TM in the whole frequency range except 10 Hz.

Chapter 3

Foot and ankle system identification base on black box models

3.1 Introduction

The foot and ankle is a passive structure able to store and release the strain energy during dynamic loading. An important role of the foot and ankle is its capability to absorb shock and vibration; changes in its ability to attenuate heel strike induced shock waves are related to joint degeneration [10, 13].

Experimental methods and modeling have been widely used to understand the dynamic response of the human body. Some studies modeled the human body as a two degree or a three degree of freedom [26, 33, 34] system to analyze the impulse loading or vibration transfer of the lower leg. Wei and Griffin [33] modeled the vertical apparent mass of the seated human body as four models (two single degree of freedom models and two two degrees of freedom models). The developed models were fitted to the measured mean apparent mass of 60 subjects, and the optimum parameters of those models were obtained. In their results, the fitting with the two degrees of freedom model showed similar apparent mass to the human body. Wu *et al*. [26] investigated the body biodynamic response of the seated human using experimental data and four biodynamic models from previous studies. They solved the equations of motion for the selected models to derive the modulus and phase of the measured apparent mass (APMS), the driving-point mechanical impedance (DPMI), and the seat-to-head transmissibility (STHT). The identified primary resonant frequencies were compared, and the results showed APMS and STHT represented appropriate transfer functions of body dynamic

models. The impulse loading during running was modeled by Kim *et al*. [34]. The dissipation and absorption of shock generated during running was investigated by developing a three degrees of freedom model for foot strike transients. Also, the unknown parameters were predicted from the experimental data, and the results of the mathematical model were verified with a drop test. This study concluded that the key role to attenuate the impact loading was the damping constant of the landing cushion.

Some studies modeled the foot and ankle structure exposed to the impact loading as a simple truss structure with only spring or spring and damping combination [35, 36, 37]. Gefen [35] and Simkin and Leichter [36] utilized a simple truss structure (two inclined rigid bodies hinged at the apex of the truss) for the foot longitudinal arch and a spring (the connection between the ends of each bar) for the plantar fascia. Kim and Voloshin [37] used a simple truss structure, but viscoelastic properties were utilized instead of a simple spring for the plantar fascia.

Modeling the complicated structure of the foot and ankle system remains a challenging problem since physical knowledge is not sufficient to describe the foot and ankle system. As shown in literature surveys, the simplified models have been applied to the human body and the foot and ankle for investigating the vibration and impact absorbing capability of the human body and the foot and ankle system. However, it is not reasonable to express the complex foot and ankle structure by a simplified model without any organized approach. Therefore, the system identification via black box models could be a good starting point to model the foot and ankle system because it could provide the characteristics of the dynamic model and guide the development of the dynamic model in the future.

The black box model with parameters or without parameters has been widely used to identify various complex models such as physiological, chemical, and mechanical structures [8, 9, 38-40]. Czop and Wszloek [38] performed the system identification of a servo-hydraulic test rig and obtained the parametric representation of the model. Their study was started from several linear model structures such as linear polynomial models and extended to a nonlinear model structure with the Hammerstein-Wiener model, which uses one or two nonlinear blocks with a linear block to describe dynamic system. The induction motor was identified with the black box model [39, 40]. Yaacob and Mohamed [39] utilized a linear system identification (ARMAX: AutoRegressive Moving Average model with eXogenous input), and Mohamed and Koivo [40] utilized a nonlinear system identification (NNARX: Neural Network Auto-Regressive Moving Average model with eXogenous input). These two studies successfully validated and provided very simple and accurate models of the induction motor. Several examples of black box system identification are shown in the manual of Matlab System Identification toolbox by Ljung [8, 9].

In this study, linear polynomial models ARX (autoregressive models with exogenous input), ARMAX (autoregressive moving average model with exogenous input), OE (Output error), BJ (Box-Jenkins) and the state-space (SS) models were utilized to describe the model structure of the foot and ankle system. The estimated polynomial models and the state-space model of the foot and ankle exposed to vertical excitation are expected to show the system behavior and the dynamic characteristics, such as transfer functions, to describe impact or shock absorbing capability of the foot and ankle system.

3.2 Method

3.2.1 Experimental data and procedures of system identification

The experimental data to identify the system of the lower leg exposed to vertical vibration was obtained from the previous chapter. The experimental data at the MM was selected as the measurement data for parametric black box models since the transmissibility for between the Base and MM was dominant, and the case of additional mass condition was utilized for system identification because three postures of the foot and ankle did not affect the transmissibility results as shown in the previous chapter. The measured input and output data through the experiment was utilized to estimate the transfer characteristics of the foot and ankle system without considering a priori information such as the actual dimensions, geometry and vibrational characteristics.

The basic procedure for system identification is illustrated in Figure 3.1. Using the experimental results, the appropriate model is selected, the selected model is estimated, and then the estimated model is validated. The validation of the estimated model is performed to check the suitableness of the estimated model. If the estimated model is accepted, the procedure of system identification is completed, but if the estimated model is rejected, system identification repeats from the step of model structure selection until the validation is accepted.

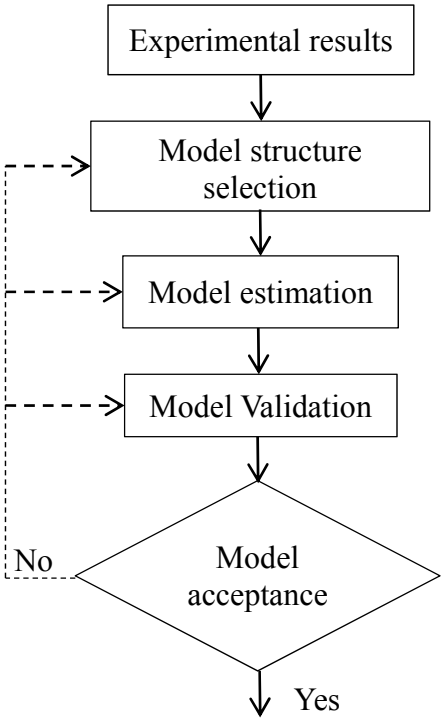

Figure 3.1 The procedure for system identification [8, 9].

3.2.2 Model structure selection, estimation, validation

The general structure of a dynamic system can be expressed with two transfer functions: $G(q)$ for input to output and $H(q)$ for disturbance to output as shown in Figure 3.2. The transfer functions are represented by

$$G(q) = \frac{B(q)}{A(q)F(q)}, \tag{3.1}$$

$$H(q) = \frac{C(q)}{A(q)D(q)}. \tag{3.2}$$

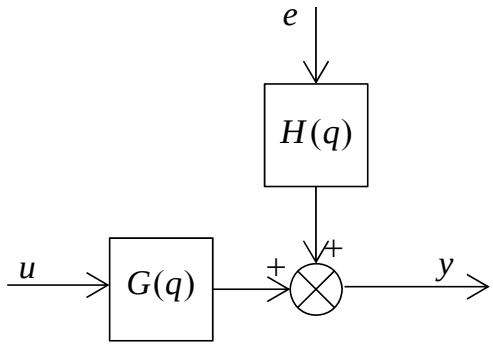

Figure 3.2 Structure of a black box model with two transfer functions [8, 9].

With the expression of the generalized linear polynomial model structure, the general structure of dynamic systems is defined by

$$A(q)y(t) = \frac{B(q)}{F(q)}u(t-k) + \frac{C(q)}{D(q)}e(t), \tag{3.3}$$

where $y(t)$ is an output, $u(t)$ is an input, $e(t)$ is disturbance, q is the forward shift operator, $A(q)$, $B(q)$, $C(q)$, $D(q)$, and $F(q)$ are polynomials of q, and k is the time delay between input and output. The polynomials are represented with the following terms:

$$\begin{aligned} A(q) &= 1 + a_1 q^{-1} + \cdots + a_{n_a} q^{-n_a}, \\ B(q) &= b_0 + b_1 q^{-1} + \cdots + b_{n_b} q^{-n_b}, \\ C(q) &= 1 + c_1 q^{-1} + \cdots + c_{n_c} q^{-n_c}, \\ D(q) &= 1 + d_1 q^{-1} + \cdots + c_{n_d} q^{-n_d}, \\ F(q) &= 1 + f_1 q^{-1} + \cdots + c_{n_f} q^{-n_f}. \end{aligned} \tag{3.4}$$

These are polynomial parameters with n being the order of polynomials (n^a, n^b, n^c, n^d, and n^f) used in the model structures [8, 9].

Among polynomial black box model sets for single input and single output (SISO) structure, ARX, ARMAX, OE, and BJ models were used in this study (Table 3.1) [8, 9].

Table 3.1 Linear polynomial model structures.

Model name	Model structure
ARX	$y(t)=\frac{B(q)}{A(q)}u(t-k)+\frac{1}{A(q)}e(t)$
ARMAX	$y(t)=\frac{B(q)}{A(q)}u(t-k)+\frac{C(q)}{A(q)}e(t)$
OE	$y(t)=\frac{B(q)}{F(q)}u(t-k)+e(t)$
BJ	$y(t)=\frac{B(q)}{F(q)}u(t-k)+\frac{C(q)}{D(q)}e(t)$

When the polynomial terms are applied to each model, the dynamic equations for each model can be expressed as follows [8, 9]:

for ARX model

$$y(t)+a_1y(t-1)+\ldots+a_{n_a}y(t-n_a)=b_1u(t-1)+\ldots+b_{n_b}u(t-n_b)+e(t), \tag{3.5}$$

for ARMAX model

$$\begin{aligned} y(t)+a_1y(t-1)+\ldots+a_{n_a}y(t-n_a)&=b_1u(t-1)+\ldots+b_{n_b}u(t-n_b)\\ &+e(t)+c_1e(t-1)+\ldots+c_{n_c}e(t-n_c), \end{aligned} \tag{3.6}$$

for OE model

$$\begin{aligned} z(t)+f_1z(t-1)+\ldots+f_{n_f}z(t-n_f)&=b_1u(t-1)+\ldots+b_{n_b}u(t-n_b),\\ y(t)&=z(t)+e(t), \end{aligned} \tag{3.7}$$

where $z(t)$ is undisturbed output

for BJ model

$$z(t) + f_1 z(t-1) + \ldots + f_{n_f} z(t-n_f) = b_1 u(t-1) + \ldots + b_{n_b} u(t-n_b),$$

$$w(t) + d_1 w(t-1) + \ldots + a_{n_d} w(t-n_d) = e(t) + c_1 e(t-1) + \ldots + c_{n_c} e(t-n_c),$$

$$y(t) = z(t) + w(t). \tag{3.8}$$

The free parameterization state-space model was also tested to describe the relationship between the input and output signal as a first-order difference equation using the subspace method [6].

$$x(t+1) = Ax(t) + Bu(t) + Ke(t), \tag{3.9}$$

$$y(t) = Cx(t) + Du(t) + e(t), \tag{3.10}$$

$$x(0) = x_0 \tag{3.11}$$

where A, B, C, D and K are the system matrix, and x is the state, u is the input, y is the output, e is the disturbance, and $x(0)$ is the initial condition.

Model selection, estimation and validation of model have been carried out with the System Identification Toolbox of Matlab®. The utilized numerical methods for model estimation were the least-squares method for ARX, iterative prediction-error minimization method for other polynomial models and subspace method (n4sid) for state-space model [8, 9].

Iterative prediction-error minimization method, which is quite well-known and widely used, was utilized to find parameters in the dynamic equations minimizing the prediction error [8, 9]:

$$\varepsilon(t,\theta) = y(t) - \hat{y}(t_{t-1},\theta), \tag{3.12}$$

where θ parameters vectors to be estimate $\varepsilon(t,\theta)$ is prediction error, $y(t)$ is output measure, and $\hat{y}(t_{t-1},\theta)$ is prediction of $y(t)$ with the parameters of the previous step. The general model structure is utilized to apply the prediction error method with a linear predictor. It has the form

$$y(t) = G(q^{-1},\theta)u(t) + H(q^{-1},\theta)e(t),$$

$$\hat{y}(t_{t-1},\theta) = L_1(q^{-1},\theta)y(t) + L_2(q^{-1},\theta)u(t). \tag{3.13}$$

Here, $u(t)$ is the input, $e(t)$ is the sequence of independent random variables with zero means, $L_1(q^{-1},\theta)$ is the past data, and $L_2(q^{-1},\theta)$ is the predictor filters. The prediction error is calculated from the model and predictor as follows:

$$\varepsilon(t) = y(t) - \hat{y}(t_{t-1},\theta) = y(t) - \left\{L_1(q^{-1},\theta)y(t) + L_2(q^{-1},\theta)u(t)\right\}. \tag{3.14}$$

An error criterion to validate the estimated parameters is based on the squared norm of prediction error:

$$V_N(\theta) = \frac{1}{N}\sum_{t=1}^{N}\varepsilon(t,\theta)\varepsilon^T(t,\theta). \tag{3.15}$$

The estimation is to minimize the error criterion described by

$$\hat{\theta} = \arg\min_{\theta} V(\theta). \tag{3.16}$$

Finally, the system matrix of a model was estimated when the error criterion is minimized.

A model structure and order should be selected in such a way that is appropriate for the measured data before estimating a model. The process of choosing a reasonable

model structure and order were performed on the basis of trial and error to check the Akaike's Information Criterion (AIC) for the estimated model. AIC represents the model quality when the model is simulated with a different data set and it is based on Akaike's Final Prediction Error (FPE) shown in the following equation [8, 9]:

$$FPE = V\left(\frac{1+d/N}{1-d/N}\right), \tag{3.17}$$

where d and N is the number of estimated parameters and data set respectively. V is the loss function,

$$V = \det\left(\frac{1}{N}\sum_{1}^{N}\varepsilon(t,\theta_N)(\varepsilon(t,\theta_N))^T\right),$$

where θ_N is the estimated parameters [8, 9]. For $d \ll N$, the approximation of Eq (3.17) is expressed as

$$FPE = V\left(1+\frac{2d}{N}\right), \tag{3.18}$$

the logarithmic form of Eq (3.18) represents [8, 9]

$$AIC = \log\left(V+\frac{2d}{N}\right). \tag{3.19}$$

Relatively simple models such as ARX and OE model were tested in order ranges between 1 to 15 for n^a and n^b and between 1 to 5 for n^f. The suitable n^a, n^b, and n^f were decided based on the AIC. To define the order of the other models (ARMAX and BJ), the selected order of ARX model was applied and n^c and n^d were chosen after several trials. Similar to the identification of polynomial input and output models, the order of the state-space model was selected by trial and error method between 2 to 15.

The validation of model has been performed with the measurement data extracted from the part of the data not used in the identification process. The output was simulated using the estimated model and the percentage between the measurement and simulation was calculated for the model validation. The fitting was defined as follows:

$$fit = \left(1 - \frac{|y - \hat{y}|}{|y - \bar{y}|}\right) \times 100, \tag{3.20}$$

where y is the measured output, $\hat{y}$ is the predicted output, and $\bar{y}$ is the mean value of the measured output [8]. It is necessary to repeat the system identification procedure until the validation is acceptable.

3.3 Results

Model selection, estimation, and validation were performed in the measured frequency range of 10-50 Hz with the measurement data from 10 randomly selected subjects. The selected order and fitting percentage results of a typical subject (subject # 16) for various loading conditions utilizing ARX, ARMAX, OE, BJ, and the state-space model are listed in Table 3.2. The grey cells show the best fitting among identified models. The identified results of the rest of the 9 subjects are included in Appendix A.

All polynomial structures and the state-space model performed well for identifying the black box model. OE model had a good performance in system identification since it showed better fitting than other model structures as the simplest model structure. The obtained range of polynomials orders was mainly distributed in the range of 9 to 15, 1 to 12, 1 to 12 for n_a, n_b, and n_k respectively and n_c, n_d, and n_f were 3 or 5. The order of the state-space model was found to be around 2 to 8 for the whole

frequency range. The higher order of the state-space model was observed at the lower frequency (10-25 Hz) and loaded condition since the output acceleration had nonlinearity with the loaded condition at the lower frequency. This order range would be used as a reference for the identification of the grey box model in the next chapter.

For subject # 16, the validation (10-25 Hz) between the measured data and the simulation of the estimated model are shown in Figures 3.3-3.6 since it has lower fitting percentage and more complex trial and error process comparatively to the higher input frequency case. In Figures 3.3-3.6, the left figures show the overall simulation results, and the right figure show the amplification of a cycle. The difference between measurement and simulation was generally observed in damping oscillation and the shape of acceleration peak. It is closely related to the nonlinearity of the output acceleration. Since the black box models utilized to identify systems were based on the linearized model, they have some limitation to follow the nonlinear behavior shown in the lower frequencies.

Table 3.2 Black box system identification results (Subject # 16).

Freq	Mass	ARX		ARMAX		BJ		OE		SS	
(Hz)	(kg)	(na, nb, nk)	fit (%)	(na, nb, nc, nk)	fit (%)	(nb, nc, nd, nf, nk)	fit (%)	(nb, nf, nk)	fit (%)	(order)	fit (%)
10	0	(9, 7, 2)	74	(9, 7, 5, 2)	74	(7, 5, 5, 5, 2)	80	(7, 5, 2)	79	7	75
	2.3	(13, 12, 15)	72	(13, 12, 3, 15)	72	(12, 3, 3, 3, 15)	69	(12, 3, 15)	77	8	62
	4.5	(11, 11, 8)	79	(11, 11, 3, 8)	78	(11, 3, 3, 3, 8)	68	(11, 3, 8)	84	6	73
15	0	(13, 3, 3)	82	(13, 3, 3, 3)	88	(3, 3, 3, 3, 3)	90	(3, 3, 3)	90	5	88
	2.3	(9, 12, 8)	92	(9, 12, 3, 8)	88	(12, 3, 3, 3, 8)	91	(12, 3, 8)	93	5	84
	4.5	(9, 11, 4)	85	(9, 11, 3, 4)	85	(11, 3, 3, 3, 4)	92	(11, 3, 4)	90	5	82
20	0	(9, 6, 2)	90	(9, 6, 3, 2)	90	(6, 3, 3, 3, 2)	90	(6, 3, 2)	90	5	88
	2.3	(9, 10, 12)	91	(9, 10, 3, 12	91	(10, 3, 3, 3, 12)	94	(10, 3, 12)	95	4	89
	4.5	(12, 10, 9)	93	(12, 10, 3, 9)	93	(10, 3, 3, 3, 9)	95	(10, 3, 9)	95	4	90
25	0	(12, 4, 1)	93	(12, 4, 3, 1)	93	(4, 3, 3, 3, 1)	93	(4, 3, 1)	93	4	89
	2.3	(12, 4, 11)	95	(12, 4, 3, 11)	95	(4, 3, 3, 3, 11)	96	(4, 3, 11)	96	4	93
	4.5	(9, 7, 9)	95	(9, 7, 3, 9)	95	(7, 3, 3, 3, 9)	95	(7, 3, 9)	95	4	93
30	0	(11, 4, 10)	92	(11, 4, 3, 10)	94	(4, 3, 3, 3, 10)	96	(4, 3, 10)	95	4	87
	2.3	(11, 10, 10)	95	(11, 10, 3, 10)	95	(10, 3, 3, 3, 10)	97	(10, 3, 10)	97	5	88
	4.5	(9, 8, 3)	95	(9, 8, 3, 3)	96	(8, 3, 3, 3, 3)	96	(8, 3, 3)	95	5	93
35	0	(10, 5, 2)	92	(10, 5, 3, 2)	92	(5, 3, 3, 3, 2)	95	(5, 3, 2)	93	5	92
	2.3	(9, 6, 10)	96	(9, 6, 3, 10)	97	(6, 3, 3, 3, 10)	88	(6, 3, 10)	97	5	94
	4.5	(12, 2, 4)	94	(12, 2, 3, 4)	90	(2, 3, 3, 3, 4)	89	(2, 3, 4)	89	5	93
40	0	(10, 6, 7)	94	(10, 6, 3, 7)	94	(6, 3, 3, 3, 7)	95	(6, 3, 7)	95	5	93
	2.3	(12, 3, 6)	96	(12, 3, 3, 6)	95	(3, 3, 3, 3, 6)	97	(3, 3, 6)	97	5	93
	4.5	(10, 12, 2)	97	(10, 12, 3, 2)	97	(12, 3, 3, 3, 2)	97	(12, 3, 2)	97	5	92
45	0	(11, 2, 5)	94	(11, 2, 3, 5)	94	(2, 3, 3, 3, 5)	93	(2, 3, 5)	93	3	94
	2.3	(12, 6, 3)	95	(12, 6, 3, 3)	95	(6, 3, 3, 3, 3)	96	(6, 3, 3)	96	3	91
	4.5	(9, 7, 6)	97	(9, 7, 3, 6)	98	(7, 3, 3, 3, 6)	97	(7, 3, 6)	96	2	90
50	0	(10, 9, 5)	83	(10, 9, 3, 5)	83	(9, 3, 3, 3, 5)	84	(9, 3, 5)	95	5	83
	2.3	(9, 7, 8)	97	(9, 7, 3, 8)	96	(7, 3, 3, 3, 8)	97	(7, 3, 8)	97	4	94
	4.5	(10, 4, 3)	95	(10, 4, 3, 3)	95	(4, 3, 3, 3, 3)	95	(4, 3, 3)	95	3	94

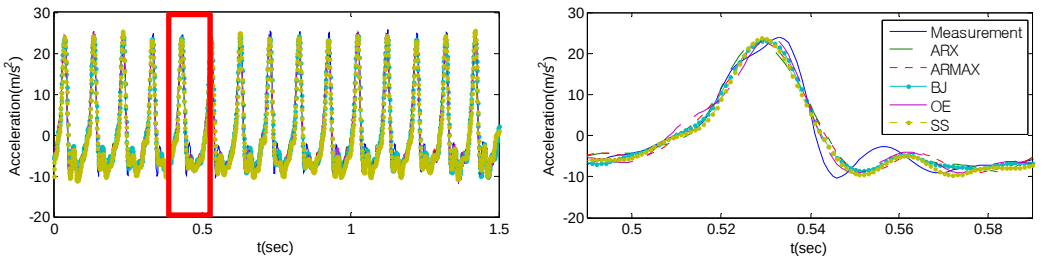

(a) 10Hz & 0kg: ARX(74%), ARMAX(75%), BJ(80%), OE(79%), SS(75%)

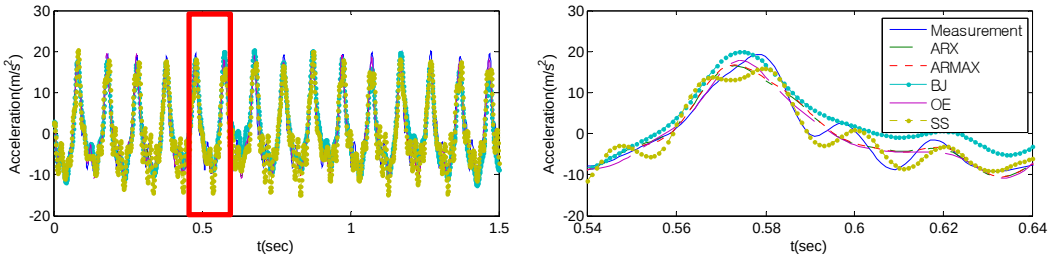

(b) 10Hz & 2.3kg: ARX(72%), ARMAX(72%), BJ(69%), OE(78%), SS(62%)

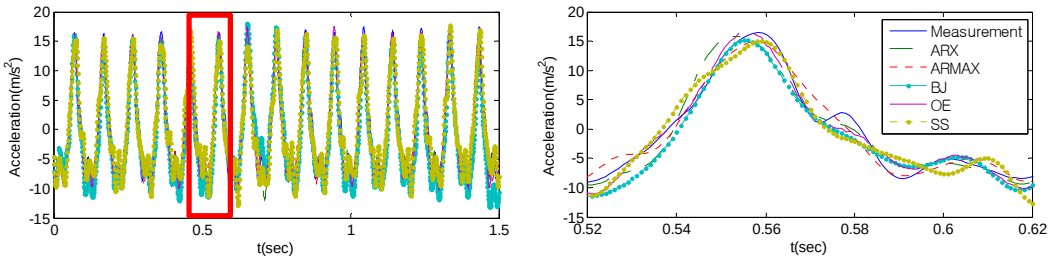

(c) 10Hz & 4.5kg: ARX(79%), ARMAX(79%), BJ(68%), OE(84%), SS(73%)

Figure 3.3 An example of black box system identification results at 10 Hz (subject # 16).

In the estimation result of 10 Hz case, the fitting percentage was lower relatively to the results of higher frequencies (Figure 3.3). Regardless of the applied mass conditions at 10 Hz, the part of damping oscillation in the output acceleration is the major reason why the simulation results are different from the measurement (Figures 3.3 (a)-(c)).

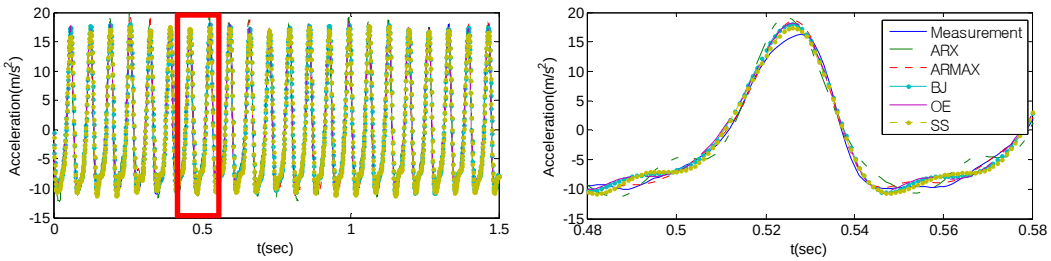

(a) 15Hz & 0kg: ARX(82%), ARMAX(88%), BJ(90%), OE(90%), SS(88%)

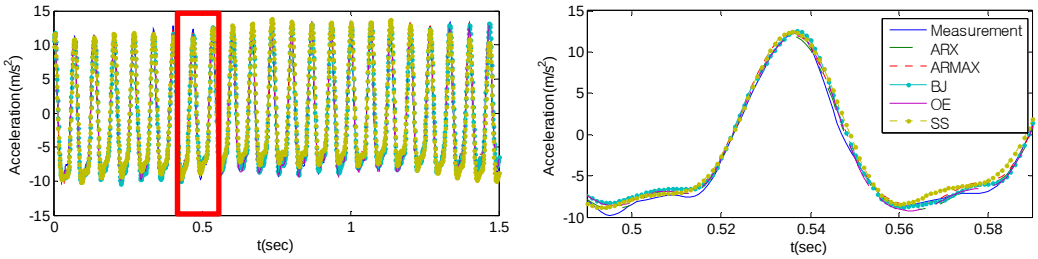

(b) 15Hz & 2.3kg: ARX(92%), ARMAX(88%), BJ(91%), OE(93%), SS(84%)

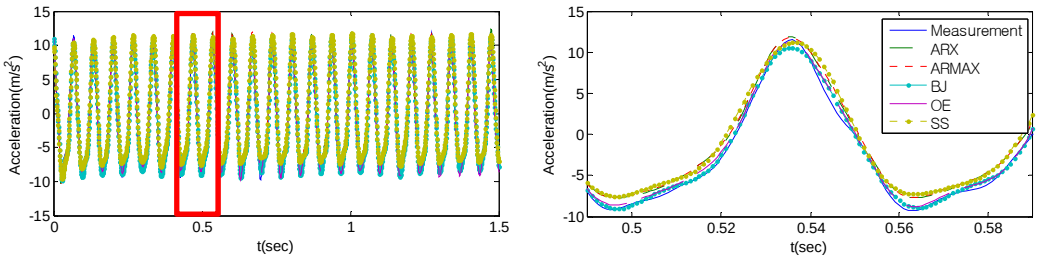

(c) 15Hz & 4.5kg: ARX(85%), ARMAX(85%), BJ(92%), OE(90%), SS(82%)

Figure 3.4 An example of black box system identification results at 15 Hz (subject # 16).

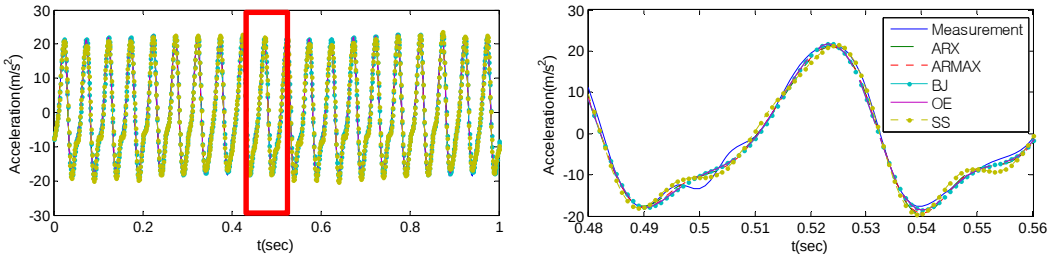

(a) 20Hz & 0kg: ARX(90%), ARMAX(90%), BJ(90%), OE(90%), SS(88%)

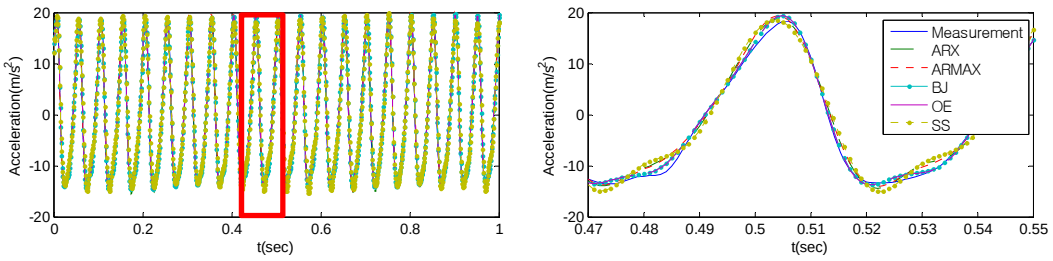

(b) 20Hz & 2.3kg: ARX(91%), ARMAX(91%), BJ(95%), OE(95%), SS(89%)

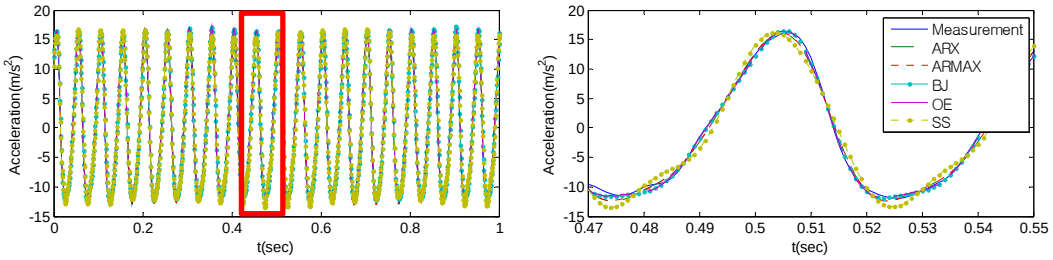

(c) 20Hz & 4.5kg: ARX(93%), ARMAX(93%), BJ(95%), OE(95%), SS(90%)

Figure 3.5 An example of black box system identification results at 20 Hz (subject # 16).

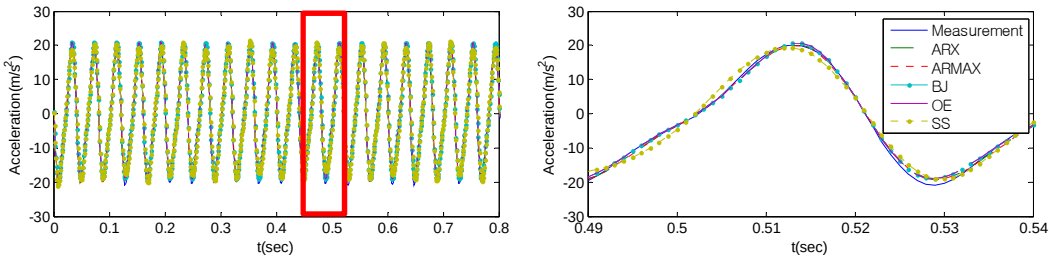

(a) 25Hz & 0kg: ARX(93%), ARMAX(93%), BJ(93%), OE(93%), SS(89%)

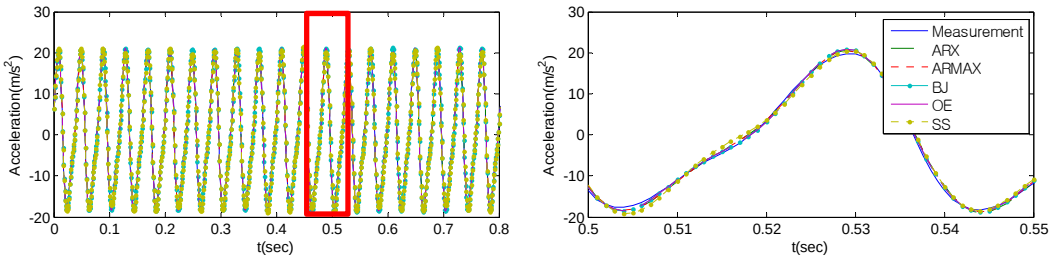

(b) 25Hz & 2.3kg: ARX(95%), ARMAX(95%), BJ(96%), OE(96%), SS(93%)

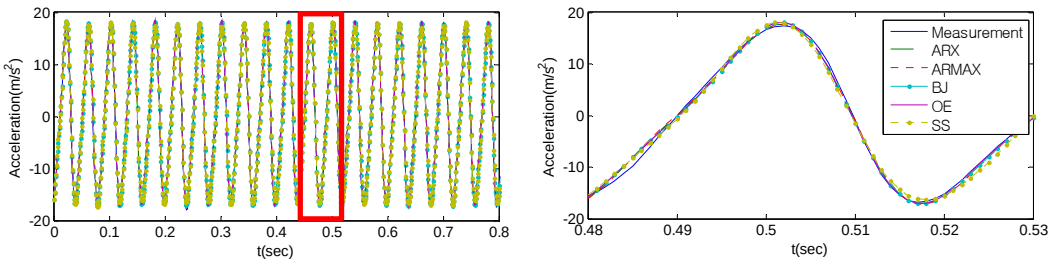

(c) 25Hz & 4.5kg: ARX(95%), ARMAX(95%), BJ(95%), OE(95%), SS(93%)

Figure 3.6 An example of black box system identification results at 25 Hz (subject # 16).

The fitting percentages were improved with comparison to the 10 Hz case as the applied frequency was increased (Figures 3.4-.3.6). The oscillation generated damping properties of the system was decreased. As a result, the nonlinearity of system was decreased, and the system gradually showed linear response. This fact was supported by the results of the 25 Hz case shown in Figure 3.6 (a)-(c).

The validation results for higher frequency (30-50 Hz) are included in Appendix A. The estimated models represented the measured data well, but the fitting percentage of the output was lower for 10 and 15 Hz input frequency and loaded condition. In the future study, it might be necessary to consider nonlinear black box model identification for the 10 and 15 Hz and loaded cases because of the observed nonlinearity of output acceleration.

3.4 Conclusions

The purpose of this study was to identify the transfer function of the black box models such as polynomial models and the state-space model and help to understand dynamic response of the foot and ankle exposed to vertical vibration. The estimated

polynomial model structures and the state-space model were able to fit well with the measured data. Generally, OE model resulted in the best fit. The observed nonlinearity of output acceleration affected the fitting percentage at the lower frequency and additional mass conditions. Because of the complexity of output acceleration patterns, the order of state-space model of the lower frequency and additional mass condition was higher than that of the higher frequency and without extra mass condition. This result is used as a guide for creating the grey box model of the foot and ankle in the next chapter. For the lower frequencies (10 and 15 Hz regardless of applied mass conditions) which is the fitting percentage is low, nonlinear black box model identification could be proposed for better estimation.

CHAPTER 4

Development of the dynamic model of the foot and ankle system exposed to vertical vibration

4.1 Introduction

Human body vibration has two contradicting characteristics. It has been shown by many researchers that the vibration exposure of the human body during everyday life physical activities is usually harmful and leads to wear of the articular joints such as the ankle, knee, hip, and spine; finally it causes joint degeneration [12, 14]. The advantage of human body vibration has been shown in other areas, like strengthening of muscle and bone [5-7]. Applying appropriate vibration, muscle strength is improved, and bone density is increased, which decreases the risk to osteoporosis.

The foot and ankle plays an important role as a foundation supporting the human body and absorbing impact loadings between the human body and the ground. It is a passive structure capable to store and release strain energy during dynamic loading such as walking and running. The capability of storing energy generally is expressed by an elastic material like springs. Various studies related to the foot and ankle have been performed in diverse areas such as structural stress analysis, clinical analysis, gait analysis, and dynamic analysis shock absorption. For better understanding of the absorption and propagation of the external vibration in the human body, the dynamic characteristics of the foot and ankle system have to be investigated as it is the entrance point of the external vibration.

The capability of the foot to store strain energy and return it as an elastic coil was demonstrated with the applied sinusoidal force [41, 42]. McMahon [41] described the passive spring behavior of the foot arch, storing, returning, and reducing the energy which muscle must absorb and the work which muscle did to accelerate the body in running. This simple concept of storing capacity of the foot was utilized as a two dimensional model of the foot in the sagittal plan, in which it has two rigid bodies connected by elastic spring. It showed a fundamental characteristic of the energy storage mechanism as a function of the calcaneal inclination [42]. A biomechanical model of the foot, a statically indeterminate structure supported by the head of five metatarsals and the heel in raised condition, was investigated [43]. Including the role of muscles, tendons, and ligaments, a biomechanical foot model was developed to show the mechanical principles and behavior of the anatomical foot structure [44]. The compression test with quasi-static axial loads was utilized to characterize the force distribution in relation to foot deformation [45]. The calcaneus was the main part to transfer approximately 63% of compression loads. The anterior foot was supposed to be the remaining portion of the tibial load. The mechanical property of dissected plantar fascia was measured under loading and the *in-vivo* study also was utilized to measure the height of the foot arch as the load increased [46]. It showed the measured elastic modulus of plantar fascia was 344.7×10^6 -827.4×10^6 N/m^2. Ligaments were extended at the initial loading but they became stiffer due to the increase of applied load. The tibial axial acceleration and ground reaction force during running were recorded to show the relationship between two values using the transfer functions and the frequency analysis [47]. Effective stiffness of the ankle and foot was specified as the inertial load and the elastic load through modeling

the ankle as a second order system [48]. Using a direct measurements technique, deformations and strains of the plantar fascia of the *in-vivo* during the midstance were measured to determine the elastic properties of the plantar fascia [35]. The average stiffness of plantar fascia was found to be 170±45 N/mm.

A complicated model of the foot and ankle has been realized in numerical simulation using Finite Element Methods. Cheung *et al.* [49] built a 3D Finite Element model on the basis of the coronal magnetic resonance images in which the model, including both skeletal and soft tissue components, gave the information of the internal stress and strain of the foot and ankle. They showed how the stiff soft tissue affected the plantar pressure distributions. The stress distribution of the foot structure at each phase during gait was presented by a three-dimensional Finite Element model [50].

System identification method is used to construct mathematical models or estimate unknown parameters of dynamic systems from measured input-output data. It has been utilized for biomechanical models because they are very complex and have a significant number of unknowns. Kim *et al.* [34] developed a mathematical model of heel strike transients during running. In order to identify unknown spring and damping constants the quasilinearization technique was used. A biomechanical model, which has two rigid bodies and viscoelastic models like a standard linear solid model and a Kelvin-Voigt model, was presented to show the load bearing mechanism of the foot during stance of gait [37]. As in the previous study, the unknown viscoelastic parameters were identified with the quasilinearizaiton method. It was found that the plantar fascia carried 14% of the total load on the foot. Fard *et al.*[51] identified the dynamics of the head-neck complex horizontally vibrated with developing a fourth-order mathematical model.

The coefficients of the mathematical model were identified by the frequency domain identification method, and the viscoelastic parameters of the head-neck complex were estimated with the optimization method.

4.2 The model of the foot and ankle

The characterization of the articulation and ligaments in the foot and ankle system is necessary to represent the shock and vibration absorption capability and the dynamic behavior of the foot and ankle. To characterize the ultimate strength of ligaments has been mainly studied to show individual failure of those ligaments, and some simplified models of the ligaments as springs (sometimes including dashpots) have been used to measure the elastic or viscoelastic constants. In addition, the experimental studies of the foot and ankle are generally restricted to the *in vitro* case. Owing to the complexity of the ankle and foot structures and experimental difficulties, computational methods were suggested to predict the load distribution and the internal stress and strain of the foot and ankle model [50, 52]. But the stiffness and the damping properties of the foot and ankle were not estimated since researches have used the mechanical properties from the previous experimental studies to analyze their structural characteristics. Moreover, the elastic or viscoelastic characteristics of the human foot and ankle joint have been studied [34-37, 41, 48], but no well-developed and characterized model was presented. The objective of this study was to investigate vibration absorbing behavior of the human ankle and foot and to develop a mathematical model capable to describe the attenuation and modification of an externally induced vibration by the foot and ankle joint.

The foot and ankle act as a shock and vibration absorber for supporting the whole body and propelling it during gait. It has two longitudinal arches: one is a medial longitudinal arch (runs across the calcaneus to the talus, navicular, three cuneiforms, and the heads of the first three metatarsals); the other one is a lateral longitudinal arch (starts from the calcaneus, go through the cuboid, and ends at the heads of the two lateral metatarsals). The medial longitudinal arch can be simplified as a simple truss structure because it is more dynamic compared to the lateral longitudinal arch. So, the human foot and ankle model has been developed as simplified two dimensional, planar models using the truss structure connected with springs [35-37]. Both ends of the truss are tied with the plantar aponeurosis, which supports the arched shape of the foot under loading. In these models, one rigid body consists of calcaneus and talus and the other rigid body includes navicular, cuneiforms, and metatarsals. Considering plantar aponeurosis connecting from the calcaneus to the metatarsophalangeal articulation, two rigid bodies are connected with one elastic spring or standard viscoelastic solid material model. The simplified models of these studies are shown in Figure 4.1: A, B, C: frictionless hinges; L: length of the rigid elements; α: inclination angle of the rigid elements; TS: tension spring; F: vertical load.

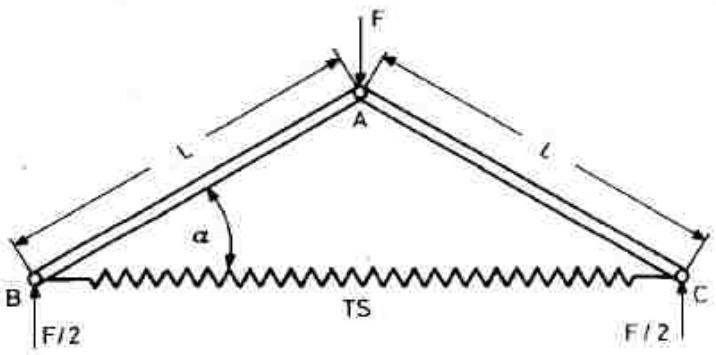

(a)

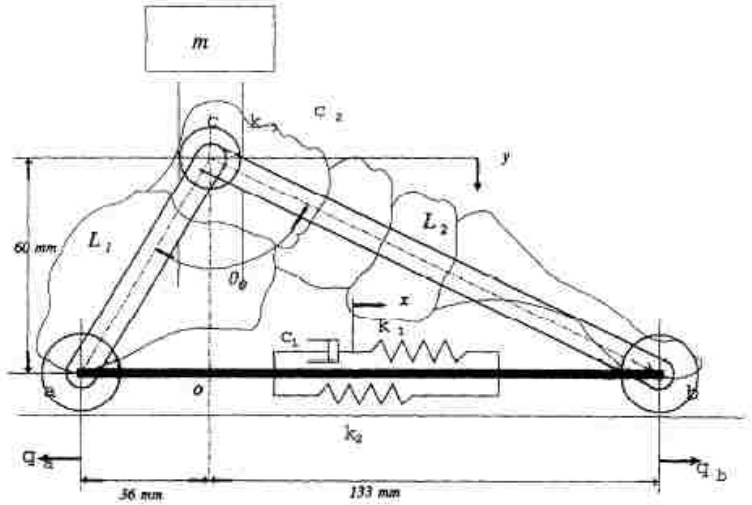

(b)

Figure 4.1 The simplified biomechanical models of foot ((a) [36] and (b) [37]).

Similarly to the other studies [35-37] a simplified truss structure was applied as the initial model of this study, but this study considered the mass of foot bones, more segments, the heel pad, and the ankle joint in the model. The medial arch was modeled as the truss which has five rigid bodies including the tibia as shown in Figure 4.2. The part of the forefoot in the medial arch (the metatarsals, the cuneiforms, and the navicular) was assumed to be three rigid bodies, and the hindfoot including the talus and the calcaneus were also modeled as a rigid body. The spring ligament, short plantar ligament, and long

plantar ligament between each linkage were modeled as a Kelvin-Voigt model. The connection between the end of calcaneus and metatarsal (the plantar aponeurosis) was expressed by a standard viscoelastic solid material model. The fat pad at the foot bottom and the articular joint between the talus and tibia were modeled with a Kelvin-Voigt model to represent the vibration absorbing capability.

The material properties of the front fat pad and heel fat pad were assumed to have the same values for model simplification. The center of mass of tibia was assumed in the middle of the rigid body, and it was assumed to move in the vertical direction only. Similarly, the centers of mass of each rigid body in the foot structure were assumed to be located on the midpoint of each bone.

In the geometrical view (Figure 4.2 (b)), the bottom surface of the foot is set as the harmonic displacement y_B at the base support, an output y_T is the displacement of the tibia, y_F is the base of the foot, θ is the angle of a rigid body, x is the displacement in the horizontal direction, L is the length of a rigid body, I is the moment of inertia of a rigid body, m is the mass of a rigid body, and the subscript $T, 1, 2, 3, 4$ are the tibia and each rigid body of the foot segments. The dynamic properties are as follows: k_F is the spring constant of the fat pad of the foot, c_F is the damping constant of the fat pad of foot, k_{11} and k_{12} are the spring constants and c_1 is the damping constant of the standard linear solid viscoelastic material for the plantar aponeurosis, k_2, k_3, k_4 and c_2, c_3, c_4 are the spring constants and damping constants of each joint, and k_T and c_T are the articular joints between the talus and tibia (Figure 4.2 (c)).

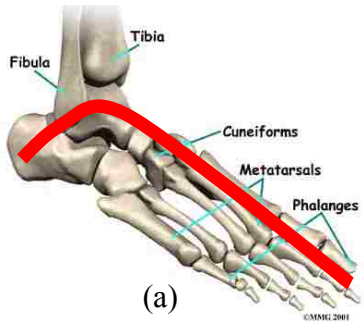

(a)

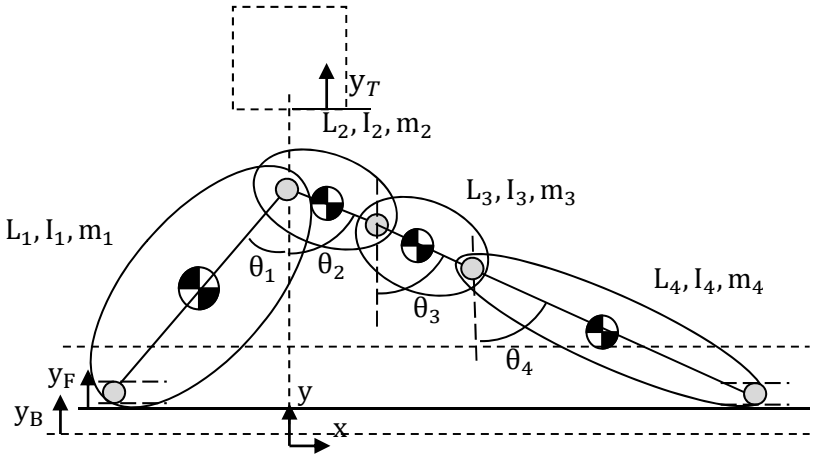

(b)

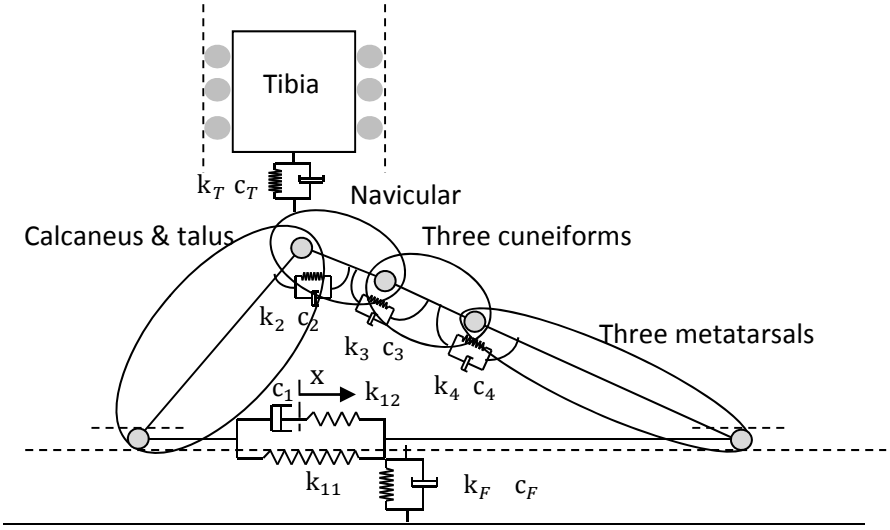

(c)

Figure 4.2 The model of the foot and ankle structure (a) 3d model [53], (b) geometry, and (c) dynamic properties.

The geometric and physical information of each rigid body, such as the length, angles, mass, moment of inertia of each rigid body, was obtained by an example of a subject's X-ray image and literature study [32, 54, 55]. The utilized geometric dimensions, masses, and moments of inertia are shown in Table 4.1. But the stiffness and the damping coefficients were left as unknown values.

Table 4.1 The constants of system.

Parameters	Rigid body				
	Tibia	1	2	3	4
m (kg)	2.36	0.133	0.014	0.025	0.043
L(m)	-	79.29e-3	14.74e-3	26.06e-3	65.27e-3
I (kg m^2)	-	28.00e-5	10.12e-7	14.13e-7	15.19e-6
θ (deg)	-	59.7	69.7	65.1	68.5

4.3 Equations of motion

The position of the tibia (m_T) is expressed in y direction since the movement of the tibia is assumed to be in the vertical direction.

$$R_T = y_T. \tag{4.1}$$

The position of the rigid body (m_1) combined the calcaneus and the talus is

$$R_{1x} = -\frac{L_1}{2}\sin(\theta_1(t)),$$

$$R_{1y} = y_F(t) + \frac{L_1}{2}\cos(\theta_1(t)). \tag{4.2}$$

The position of the navicular (m_2) is

$$R_{2x} = \frac{L_2}{2}\sin(\theta_2(t)),$$

$$R_{2y} = y_F(t) + \frac{L_2}{2}\cos(\theta_2(t)) + L_3\cos(\theta_3(t)) + L_4\cos(\theta_4(t)). \tag{4.3}$$

The position of the cuneiforms (m_3) is

$$R_{3x} = L_2\sin(\theta_2(t)) + \frac{L_3}{2}\sin(\theta_3(t)),$$

$$R_{3y} = y_F(t) + \frac{L_3}{2}\cos(\theta_3(t)) + L_4\cos(\theta_4(t)). \tag{4.4}$$

The position of the cuneiforms (m_4) is

$$R_{4x} = L_2\sin(\theta_2(t)) + L_3\sin(\theta_3(t)) + \frac{L_4}{2}\sin(\theta_4(t)),$$

$$R_{4y} = y_F(t) + \frac{L_4}{2}\cos(\theta_4(t)). \tag{4.5}$$

The system has a constraint as follows:

$$L_1\cos(\theta_1(t)) = L_2\cos(\theta_2(t)) + L_3\cos(\theta_3(t)) + L_4\cos(\theta_4(t)). \tag{4.6}$$

The angle θ_1 can be expressed from Eq. (4.6) as

$$\theta_1(t) = \cos^{-1}\left(\frac{L_2\cos(\theta_2(t)) + L_3\cos(\theta_3(t)) + L_4\cos(\theta_4(t))}{L_1}\right). \tag{4.7}$$

In a five-rigid body model, there are eight coordinates (x, y_B, , y_F, y_T, θ_1, θ_2, θ_3, and θ_4). Because this model has a holonomic constraint (the rheonomic constraint) as shown in Eq. (4.6), these coordinates could be reduced to seven. Two relative displacements (z_F is the relative displacement between the fat pad base and the bottom of

the foot bones and z_T is the relative displacement between the talus and the tibia) were defined to substitute several terms into the equations of motion

$$z_F = y_F - y_B,$$

$$z_T = y_T - (y_F + L_1 \cos(\theta_1(t))). \tag{4.8}$$

The kinetic energy (T), potential energy (U), and dissipation energy (D) can be obtained with the derived position vector. Total kinetic energy, potential energy, and dissipation energy are expressed in the following-form

$$T = \frac{1}{2} m_T \dot{R}_T{}^2 + \frac{1}{2}\sum_{i=1}^{4} m_i \dot{R}_{ix}{}^2 + \frac{1}{2}\sum_{i=1}^{4} m_i \dot{R}_{iy}{}^2 + \frac{1}{2}\sum_{i=1}^{4} I_i \dot{\Theta}_i{}^2,$$

$$U = \frac{1}{2} k_{11} \delta_{11}{}^2 + \frac{1}{2} k_{12} \delta_{12}{}^2 + \frac{1}{2}\sum_{i=2}^{3} k_i \delta_i{}^2 + \frac{1}{2} k_F \delta_F{}^2 + \frac{1}{2} k_T \delta_T{}^2,$$

$$D = \frac{1}{2}\sum_{i=1}^{4} c_i \dot{\delta}_i{}^2 + \frac{1}{2} c_F \dot{\delta}_F{}^2 + \frac{1}{2} c_T \dot{\delta}_T{}^2, \tag{4.9}$$

where i is the location of the centers of each mass and δ_{11}, δ_{12}, δ_F, and δ_T are the displacement for each spring and damping constant. The derived kinetic, potential, and dissipation energy are applied to Lagrange's equations

$$\frac{d}{dt}\left(\frac{\partial T}{\partial \dot{q}_j}\right) - \frac{\partial T}{\partial q_j} + \frac{\partial V}{\partial q_j} + \frac{\partial D}{\partial q_j} = Q_{j,} \qquad j = 1, 2, \cdots, 6 \tag{4.10}$$

where $j = 1, 2, \cdots, 6$ is the generalized coordinates, and Q_j is the conservative generalized force according to the generalized coordinates (x, z_F, z_T, θ_2, θ_3, and θ_4).

The derived nonlinear second order differential equations are as follows

$$\begin{pmatrix} A_{11} & A_{12} & A_{13} & A_{14} & A_{15} & A_{16} \\ Sym & A_{22} & A_{23} & A_{24} & A_{25} & A_{26} \\ Sym & Sym & A_{33} & A_{34} & A_{35} & A_{36} \\ Sym & Sym & Sym & A_{44} & A_{45} & A_{46} \\ Sym & Sym & Sym & Sym & A_{55} & A_{56} \\ Sym & Sym & Sym & Sym & Sym & A_{66} \end{pmatrix} \begin{Bmatrix} \ddot{z}_F \\ \ddot{z}_T \\ \ddot{\theta}_2 \\ \ddot{\theta}_3 \\ \ddot{\theta}_4 \\ \ddot{x} \end{Bmatrix} = \begin{bmatrix} B_1 \\ B_2 \\ B_3 \\ B_4 \\ B_5 \\ B_6 \end{bmatrix}, \tag{4.11}$$

where *Sym* denotes the symmetry of the matrix. All terms of the nonlinear second order differential equations are defined in Appendix B.

The derived nonlinear multi degrees of freedom model is a very complicated equation, and solving the problem numerically is a time consuming procedure. In order to reduce the calculation time for dynamic simulation, the geometric nonlinearities were simplified with the assumption that there is a small motion at the equilibrium position by considering only the first two terms of Taylor series expansion. The linearized equations of motion are obtained as follows:

$$\begin{pmatrix} M_{11} & M_{12} & M_{13} & M_{14} & M_{15} & M_{16} \\ Sym & M_{22} & M_{23} & M_{24} & M_{25} & M_{26} \\ Sym & Sym & M_{33} & M_{34} & M_{35} & M_{36} \\ Sym & Sym & Sym & M_{44} & M_{45} & M_{46} \\ Sym & Sym & Sym & Sym & M_{55} & M_{56} \\ Sym & Sym & Sym & Sym & Sym & M_{66} \end{pmatrix} \begin{Bmatrix} \ddot{z}_F \\ \ddot{z}_T \\ \ddot{\theta}_2' \\ \ddot{\theta}_3' \\ \ddot{\theta}_4' \\ \ddot{x} \end{Bmatrix}$$

$$= \begin{pmatrix} C_{11} & C_{12} & C_{13} & C_{14} & C_{15} & C_{16} \\ Sym & C_{22} & C_{23} & C_{24} & C_{25} & C_{26} \\ Sym & Sym & C_{33} & C_{34} & C_{35} & C_{36} \\ Sym & Sym & Sym & C_{44} & C_{45} & C_{46} \\ Sym & Sym & Sym & Sym & C_{55} & C_{56} \\ Sym & Sym & Sym & Sym & Sym & C_{66} \end{pmatrix} \begin{Bmatrix} \dot{z}_F \\ \dot{z}_T \\ \dot{\theta}_2' \\ \dot{\theta}_3' \\ \dot{\theta}_4' \\ \dot{x} \end{Bmatrix}$$

$$+ \begin{pmatrix} K_{11} & K_{12} & K_{13} & K_{14} & K_{15} & K_{16} \\ Sym & K_{22} & K_{23} & K_{24} & K_{25} & K_{26} \\ Sym & Sym & K_{33} & K_{34} & K_{35} & K_{36} \\ Sym & Sym & Sym & K_{44} & K_{45} & K_{46} \\ Sym & Sym & Sym & Sym & K_{55} & K_{56} \\ Sym & Sym & Sym & Sym & Sym & K_{66} \end{pmatrix} \begin{Bmatrix} z_F \\ z_T \\ \theta_2' \\ \theta_3' \\ \theta_4' \\ x \end{Bmatrix} + \begin{Bmatrix} Const1 \\ Const2 \\ Const3 \\ Const4 \\ Const5 \\ Const6 \end{Bmatrix}, \tag{4.12}$$

for the relative displacement of the fat pad (z_F),

$$M_{11} = m_T + m_1 + m_2 + m_3 + m_4,\ M_{12} = m_T,\ M_{13} = -\left(m_T + \frac{1}{2}m_1 + \frac{1}{2}m_2 \right) L_2 \sin\theta_{20},$$

$$M_{14} = -\left(m_T + \frac{1}{2}m_1 + m_2 + \frac{1}{2}m_3 \right) L_3 \sin\theta_{30},$$

$$M_{15} = -\left(m_T + \frac{1}{2}m_1 + m_2 + m_3 + \frac{1}{2}m_4 \right) L_4 \sin\theta_{40},\ M_{16} = 0,$$

$$C_{11} = -C_F,\ C_{12} = C_{13} = C_{14} = C_{15} = C_{16} = 0,$$

$$K_{11} = -k_F,\ K_{12} = K_{13} = K_{14} = K_{15} = K_{16} = 0,$$

$$Const1 = -M_{11}\ddot{y}_b,$$

for the relative displacement of the articular joint at ankle (z_T),

$$M_{22} = m_T,\ M_{23} = -m_T L_2 \sin\theta_{20},$$

$$M_{24} = -m_T L_3 \sin\theta_{30},\ M_{25} = -m_T L_4 \sin\theta_{40},\ M_{26} = 0,$$

$$C_{22} = -C_T,\ C_{23} = C_{24} = C_{25} = C_{26} = 0,$$

$$K_{22} = -k_T,\ K_{23} = K_{24} = K_{25} = K_{26} = 0,$$

$$Const2 = -M_{21}\ddot{y}_b,$$

for the angle of Navicular (θ_2),

$$M_{33} = \left\{\left(m_T + \frac{1}{4}m_1\frac{{L_1}^2}{E_{10}} + \frac{I_1}{E_{10}}\right)\left(L_2\sin\theta_{20}\right)^2 + \left(m_3 + m_4\right)\left(L_2\cos\theta_{20}\right)^2 + \frac{1}{4}m_2{L_2}^2 + I_2\right\},$$

$$M_{34} = \left(m_T + \frac{1}{4}m_1\frac{{L_1}^2}{E_{10}} + \frac{1}{2}m_2 + \frac{I_1}{E_{10}}\right)L_2\sin\theta_{20}L_3\sin\theta_{30} + \left(\frac{1}{2}m_3 + m_4\right)L_2\cos\theta_{20}L_3\cos\theta_{30},$$

$$M_{35} = \left(m_T + \frac{1}{4}m_1\frac{{L_1}^2}{E_{10}} + \frac{1}{2}m_2 + \frac{I_1}{E_{10}}\right)L_2\sin\theta_{20}L_4\sin\theta_{40} + \frac{1}{2}m_4L_2\cos\theta_{20}L_4\cos\theta_{40},$$

$$M_{36} = 0,$$

$$C_{33} = -\left[c_1\frac{\left(E_{20}L_1\sin\theta_{10}L_2\sin\theta_{20}\right)^2}{E_{10}} + c_2\left(\frac{L_2\sin\theta_{20}}{E_{10}} + 1\right)^2\right],$$

$$C_{34} = -\left[c_1\left(E_{20}L_1\sin\theta_{10}\right)^2 L_2\sin\theta_{20} + c_2\left(L_2\sin\theta_{20} + \sqrt{E_{10}}\right)\right]\frac{L_3\sin\theta_{30}}{E_{10}},$$

$$C_{35} = -\left[c_1\left(E_{20}L_1\sin\theta_{10}\right)^2 L_2\sin\theta_{20} + c_2\left(L_2\sin\theta_{20} + \sqrt{E_{10}}\right)\right]\frac{L_4\sin\theta_{40}}{E_{10}},$$

$$C_{36} = c_1L_1\sin\theta_{10}L_2\sin\theta_{20}\frac{E_{20}}{\sqrt{E_{10}}},$$

$$K_{33} = -\left\{ \begin{array}{l} k_{11}\left[\begin{array}{l} -2L_1 \sin\theta_{10} L_2{}^2 \sin\theta_{20} \cos\theta_{20} \dfrac{E_{20}}{\sqrt{E_{10}}} + \left(L_2 \cos\theta_{20}\right)^2 \\ +E_{20}\left(L_1 \sin\theta_{10}\right)^2 L_2 \cos\theta_{20} - \left(L_1 \sin\theta_{10} L_2 \sin\theta_{20}\right)^2 \\ +\sqrt{E_{10}} L_1 \sin\theta_{10} L_2 \sin\theta_{20} \end{array} \right] \\ +k_{12} L_2{}^2 \cos\theta_{20}{}^2 + k_2 \dfrac{\left(L_2 \sin\theta_{20} + \sqrt{E_{10}}\right)^2}{\sqrt{E_{10}}} + k_3 \end{array} \right\},$$

$$K_{34} = -\left\{ \begin{array}{l} k_{11}\left(-L_1 \sin\theta_{10} - \dfrac{E_{20}}{\sqrt{E_{10}}} \right) L_1 \sin\theta_{10} L_2 \sin\theta_{20} L_3 \sin\theta_{30} \\ +k_2 L_3 \sin\theta_{30} \left(\dfrac{L_2 \sin\theta_{20} + \sqrt{E_{10}}}{E_{10}} \right) - k_3 \end{array} \right\},$$

$$K_{35} = -\left\{ \begin{array}{l} k_{11}\left(-L_1 \sin\theta_{10} - \dfrac{E_{20}}{\sqrt{E_{10}}} \right) L_1 \sin\theta_{10} L_2 \sin\theta_{20} L_4 \sin\theta_{40} \\ +k_2 L_4 \sin\theta_{40} \dfrac{L_2 \sin\theta_{20} + \sqrt{E_{10}}}{E_{10}} \end{array} \right\},$$

$$K_{36} = k_{12} L_2 \cos\theta_{20},$$

$$Const3 = k_{11} L_1 \sin\theta_{10} \left(L_1 \sin\theta_{10} L_2 \sin\theta_{20} E_{20} - L_2 \cos\theta_{20} \sqrt{E_{10}} \right) + M_{31} \ddot{y}_b,$$

for the angle of three Cuneiforms (θ_3),

$$M_{44} = \left(m_T + \frac{1}{4} m_1 L_1{}^2 \frac{1}{E_{10}} + m_2 + \frac{I_1}{E_{10}} \right) \left(L_3 \sin\theta_{30} \right)^2 + m_4 \left(L_3 \cos\theta_{30} \right)^2 + \frac{1}{4} m_3 L_3{}^2 + I_3,$$

$$M_{45} = \left(m_T + \frac{1}{4} m_1 L_1{}^2 \frac{1}{E_{10}} + m_2 + \frac{1}{2} m_3 + \frac{I_1}{E_{10}} \right) L_3 sin\theta_{30} L_4 \sin\theta_{40} + \frac{1}{2} m_4 L_3 \cos\theta_{30} L_4 \cos\theta_{40},$$

$$M_{46} = 0,$$

$$C_{44} = -\left[c_1 \left(L_1 \sin\theta_{10} L_3 \sin\theta_{30} \right)^2 \frac{{E_{20}}^2}{E_{10}} + c_2 \frac{\left(L_3 \sin\theta_{30} \right)^2}{E_{10}} + c_3 \right],$$

$$C_{45} = -\left[c_1 \left(E_{20} L_1 \sin\theta_{10} \right)^2 L_3 \sin\theta_{30} + c_2 L_3 \sin\theta_{30} \right] \frac{L_4 \sin\theta_{40}}{E_{10}},$$

$$C_{46} = c_1 L_1 \sin\theta_{10} L_3 \sin\theta_{30} \frac{E_{20}}{\sqrt{E_{10}}},$$

$$K_{44} = -\left\{ \begin{array}{l} k_{11} \left(-L_3 \sin\theta_{30} + E_{20} \right) \left(L_1 \sin\theta_{10} \right)^2 L_3 \sin\theta_{30} \\ + k_2 \left(L_3 \sin\theta_{30} \right)^2 \frac{1}{E_{10}} + k_3 + k_4 \end{array} \right\},$$

$$K_{45} = -\left[-k_{11} \left(L_1 \sin\theta_{10} \right)^2 L_3 \sin\theta_{30} L_4 \sin\theta_{40} + k_2 L_3 \sin\theta_{30} L_4 \sin\theta_{40} \frac{1}{E_{10}} - k_4 \right],$$

$$K_{46} = 0,$$

$$Const4 = -k_{11} \left(L_1 \sin\theta_{10} \right)^2 L_3 \sin\theta_{30} E_{20} + M_{41} \ddot{y}_b,$$

for the angle of Metatarsals (θ_4),

$$M_{55} = \left(m_T + \frac{1}{4} m_1 {L_1}^2 \frac{1}{E_{10}} + m_2 + m_3 + \frac{I_1}{E_{10}} \right) \left(L_4 \sin\theta_{40} \right)^2 + \frac{1}{4} m_4 {L_4}^2 + I_4, \quad M_{56} = 0,$$

$$C_{55} = -\left[c_1 \left(L_1 \sin\theta_{10} L_4 \sin\theta_{40} \right)^2 \frac{{E_{20}}^2}{E_{10}} + c_2 \left(L_4 \sin\theta_{40} \right)^2 \frac{1}{E_{10}} + c_4 \right],$$

$$C_{56} = c_1 L_1 \sin\theta_{10} L_4 \sin\theta_{40} \frac{E_{20}}{\sqrt{E_{10}}},$$

$$K_{55} = -\left\{ \begin{array}{l} k_{11} \left(-\left(L_1 \sin\theta_{10} L_4 \sin\theta_{40} \right)^2 + \left(L_1 \sin\theta_{10} \right)^2 L_4 \sin\theta_{40} E_{20} \right) \\ + k_2 \left(L_4 \sin\theta_{40} \right)^2 \frac{1}{E_{10}} + k_4 \end{array} \right\}, \; K_{56} = 0,$$

$$Const5 = -k_{11} \left(L_1 \sin\theta_{10} \right)^2 L_4 \sin\theta_{40} E_{20} + M_{51} \ddot{y}_b,$$

for the displacement of the standard solid linear model of plantar aponeurosis (x),

$$M_{66} = 0,$$

$$C_{66} = c_1,$$

$$K_{66} = k_{12}.$$

The nonlinear output acceleration at the Medial Malleolus can be derived from Eq (4.8) as following:

$$y_{out} = z_T(t) + (z_F(t) + y_b(t) + L_2\cos(\theta_2) + L_3\cos(\theta_3) + L_4\cos(\theta_4),$$

$$\begin{aligned} \ddot{y}_{out} &= \ddot{z}_T(t) + \ddot{z}_F(t) + \ddot{y}_b(t) - L_2\cos(\theta_2)\dot{\theta}_2^{\,2} - L_2\sin(\theta_2)\ddot{\theta}_2 \\ &\quad - L_3\cos(\theta_3)\dot{\theta}_3^{\,2} - L_3\sin(\theta_3)\ddot{\theta}_3 - L_4\cos(\theta_4)\dot{\theta}_4^{\,2} - L_4\sin(\theta_4)\ddot{\theta}_4. \end{aligned} \tag{4.13}$$

The linearized output equation is

$$\ddot{y}_{out} = \ddot{z}_T(t) + \ddot{z}_F(t) + \ddot{y}_b(t) - L_2\sin(\theta_{20})\ddot{\theta}_2 - L_3\sin(\theta_{30})\ddot{\theta}_3 - L_4\sin(\theta_{40})\ddot{\theta}_4. \tag{4.14}$$

4.4 Simplification of dynamic equations

The system of linearized dynamic equations for the five-rigid body model was still complex and expensive in the computational cost since it had a large number of unknown parameters to estimate. In order to obtain a more effective and simplified model, the sensitivity analysis was employed to find influential parameters of the system. The general purpose of the sensitivity analysis is to analyze how the variation of parameters influences the output of a dynamic system. It has been utilized in the area of complex mathematical models for dynamical systems such as mechanical systems, biological systems and so on. Kim *et al*. [56] performed a parameter sensitivity analysis to analyze the effects of the variation of parameters to a piston pump system. The exact

nonlinear mathematical model of the piston pump was represented by fourth order dynamic model with order reduction of the model. In biological systems, modeling with nonlinear ordinary differential equations (ODEs) is a useful method to understand its signal transduction network and metabolism models in spite of the complexity with many parameters. The simplification of those complicated models was obtained with parameter sensitivity analysis [57].

In this study, a sensitivity analysis could provide the possible reduction of the number of unknown parameters. Consequently, it could improve dynamic models and reduce the calculation time. Considering the state and parameter vector of a dynamic system

$$X = [x_1\, x_2 \cdots x_i]^T,$$
$$\alpha = [\alpha_1\, \alpha_1 \cdots \alpha_j]^T, \tag{4.15}$$

a nonlinear dynamic equation with a state-space form is

$$\dot{X} = f(X, \alpha, u, t), X(t_0) = X_0, \tag{4.16}$$

where u is the input vector, and X_0 is the initial state vector at $t = 0$. The sensitivity vector was obtained by a Taylor series expansion

$$x_i\left(\alpha_j + \Delta\alpha_j, t\right) = x_i\left(\alpha_j, t\right) + \sum_{j=1}^{m} \frac{\partial x_i}{\partial \alpha_j}\Delta\alpha_j + \frac{1}{2}\sum_{k=1}^{m}\sum_{j=1}^{m} \frac{\partial^2 x_i}{\partial \alpha_k \partial \alpha_j}\Delta\alpha_k\Delta\alpha_j + \cdots, \tag{4.17}$$

where $\partial x_i / \partial \alpha_j$ are the first order sensitivity functions and $\partial^2 x_i / \partial \alpha_k \partial \alpha_j$ are the second order sensitivity functions [56, 57]. The first order sensitivity vectors ($s_{i,j} = \partial x_i / \partial \alpha_j$) were utilized in this study as shown in Eq (4.18) [56, 57]

$$S = \frac{\partial X}{\partial \alpha} = \begin{bmatrix} s_{1,1} & s_{1,1} & \cdots & s_{1,j} \\ s_{2,1} & s_{2,2} & \cdots & s_{2,j} \\ \vdots & \vdots & \ddots & \vdots \\ s_{i,1} & s_{i,2} & \cdots & s_{i,j} \end{bmatrix}. \tag{4.18}$$

The sensitivity matrix was calculated with the direct differential method as follows:

$$\frac{d}{dt}\frac{\partial X}{\partial \alpha_j} = J \cdot S_j + F_j,\ S_j(0) = S_0, \tag{4.19}$$

where J is Jacobian matrices of $f(x, \alpha, u, t)$ with respect to the states (x_i), S_j is the first order sensitivity vector with respect to the jth parameter (α_j), and F_j is Jacobian matrices of $f(x, \alpha, u, t)$ with respect to the jth parameter (α_j) [56, 57]

$$J = \frac{\partial f}{\partial X} = \begin{bmatrix} \frac{\partial f_1}{\partial x_1} & \frac{\partial f_1}{\partial x_2} & \cdots & \frac{\partial f_1}{\partial x_n} \\ \frac{\partial f_2}{\partial x_1} & \frac{\partial f_2}{\partial x_2} & \cdots & \frac{\partial f_2}{\partial x_n} \\ \vdots & \vdots & \ddots & \vdots \\ \frac{\partial f_n}{\partial x_1} & \frac{\partial f_n}{\partial x_2} & \cdots & \frac{\partial f_n}{\partial x_n} \end{bmatrix},\ S_j = \frac{\partial X}{\partial \alpha_j} = \begin{bmatrix} s_{1,j} \\ s_{2,j} \\ \vdots \\ s_{n,j} \end{bmatrix},\ F_j = \frac{\partial f}{\partial \alpha_j} = \begin{bmatrix} \frac{\partial f_1}{\partial \alpha_j} \\ \frac{\partial f_2}{\partial \alpha_j} \\ \vdots \\ \frac{\partial f_n}{\partial \alpha_j} \end{bmatrix}.$$

The system of differential equations from Eq (4.16) and (4.19) was solved by numerical integration, and the results of sensitivity were compared with the following dynamic relative sensitivities [56, 57]

$$RS_{i,j} = \frac{1}{N}\sqrt{\sum_{k=1}^{N} \left|\overline{s}_{i,j}(k)\right|^2}, \tag{4.20}$$

where k is the time instance, N is the total number of sampling points, and $\overline{s}_{i,j}$ is the relative sensitivity defined as follows [56, 57]

$$\overline{s}_{i,j} = \frac{\partial x_i / x_i}{\partial \theta_j / \theta_j} = \frac{\partial x_i}{\partial \theta_j}\frac{\theta_j}{x_i}. \tag{4.21}$$

The calculation of the sensitivity function and relative sensitivity were performed by tssolve.m Matlab program [58].

For the selection of parameters, random numbers were chosen in the specific ranges for each parameter based on some literatures [35, 37, 59] (Table 4.2). The initial conditions for all states were fixed as zero.

Table 4.2 The range of parameters for sensitivity analysis.

Parameter	Range
Spring constants (k_{l1}, k_{l2}, k_2, k_3, k_4, k_T, k_F)	$1\times10^4 \le$ parameters $\le 3\times10^6$
Damping constants (c_1, c_2, c_3, c_4, c_T, c_F)	$1\times10^2 \le$ parameters $\le 3\times10^3$

The parameter sensitivity results are shown in Figure 4.3. The resulting relative sensitivities for 30 random cases are shown in Figure C.1. The higher relative sensitivity values among parameters were shown in four parameters: k_T, c_T, k_F, and c_F. This means that in the developed five-rigid body model, the movement of segments of the foot arch is very small and the role of the ligament sustaining arch to absorb the external vibration could be ignored. In addition, the sensitivity analysis results demonstrated that the dominant part generating the nonlinearity of output accelerations at the Medial Malleolus was the fat pad of the foot (k_F and c_F), and the articular joint including a number of ligaments between the talus and the tibia (k_T and c_T).

However, the measured output at the Medial Malleolus is not following the sinusoidal input vibration with distorted accelerations. Therefore, the derived model should include any nonlinear behavior parts. The nonlinearity of the foot and ankle

system could be explained with the nonlinear material properties of the heel pad and articular joint, which have been shown in studies about fat pads, ligaments, tendons, or soft tissues.

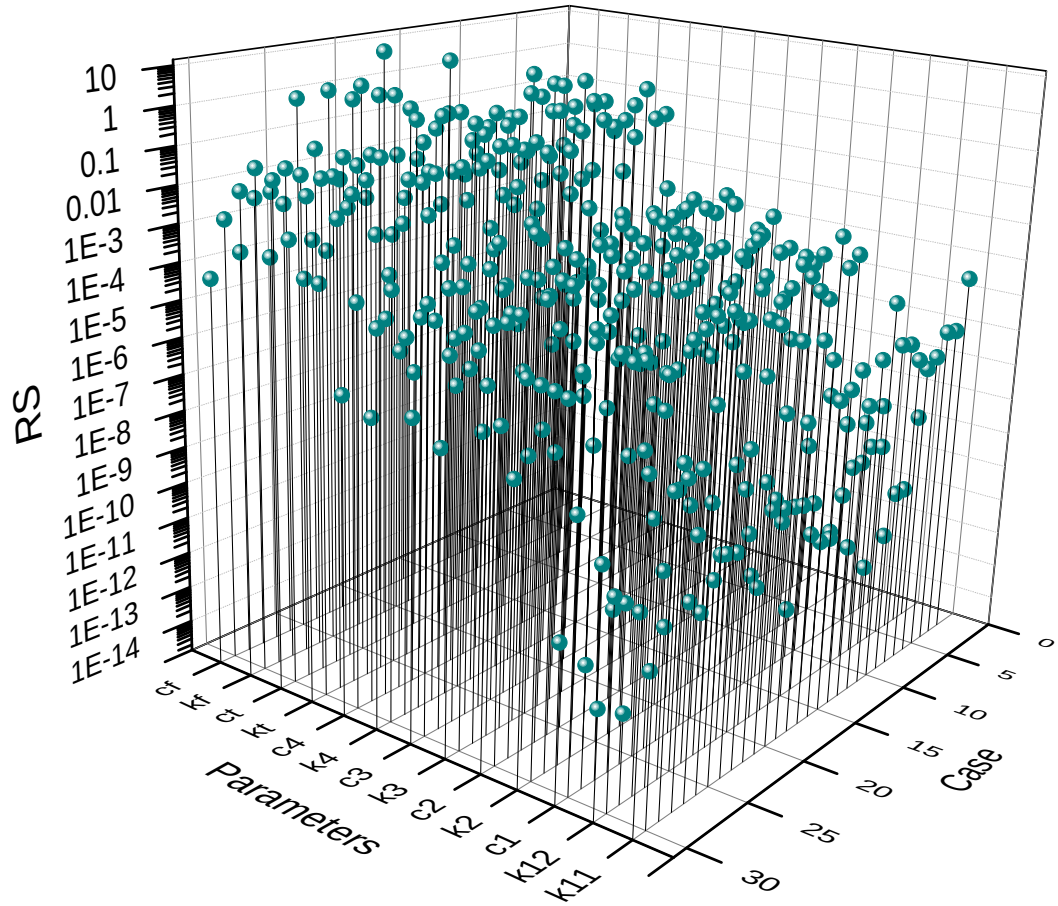

Figure 4.3 The relative sensitivity of parameters.

There are three mechanical properties to represent the heel pad and soft tissue: a quasi-linear viscoelastic model [60], the combination of a nonlinear spring and a nonlinear damper [61], and the linear spring and nonlinear damper [62] in the previous

studies. The quasi-linear viscoelastic theory is described with two functions of strain and time [60]

$$\sigma(t) = \int_0^t G(t-\tau') \frac{\partial \sigma^{(e)}\left[\varepsilon(\tau')\right]}{\partial \varepsilon} \frac{\partial \varepsilon}{\partial \tau'} d\tau',$$

$$G(t) = \frac{1 + \int_0^\infty S(\tau) e^{-t/\tau} d\tau}{1 + \int_0^\infty S(\tau) d\tau},$$

$$\sigma^{(e)}(\varepsilon) = A(e^{B\varepsilon} - 1),$$

$$S(\tau) = \left\{ \begin{array}{l} \frac{c_1}{\tau} \text{ for } \tau_1 \le \tau \le \tau_2 \\ 0 \text{ for } \tau_1 \le \tau \le \tau_2 \end{array} \right\}, \tag{4.22}$$

where σ is the stress, $G(t)$ is the reduced relaxation function, $\sigma^{(e)}(\varepsilon)$ is the elastic function, $\varepsilon(t)$ is the strain, A and B are the elastic constants, $S(\tau)$ is the relaxation spectrum, c_1 is the amplitude of the viscous effect, and τ_1 and τ_2 are the frequency limits of the relaxation spectrum. The force transferred through the heel pad was modeled with a nonlinear spring and a nonlinear damper (Eq. 4.23)

$$F = j\varepsilon^k + l\varepsilon^m \left|\dot{\varepsilon}\right|^k, \tag{4.23}$$

where j, k, l, m and n are the constants, ε is the strain, and $\dot{\varepsilon}$ is the strain rate [61]. Gefen *et al.* [62] used a modified Kelvin-Voigt model with a linear spring and a nonlinear damper for the heel pad model as follows

$$F = -E\varepsilon_c - \eta\varepsilon_c\dot{\varepsilon}_c, \tag{4.24}$$

where ε_c, $\dot{\varepsilon}_c$ are the strain and strain rate, respectively, and E, η are the constants for the spring and damper.

In this study, the combination of a linear spring and nonlinear damping constants based on Eq. (4.24) was employed for a model of the fat pad of the foot and talocrural joint. The utilized nonlinear damping model was defined by

$$c = c_1 e^{-c_2 x} \cos\left(c_3 x\right), \tag{4.25}$$

where c_1, c_2 and c_3 are constants, and x is the relative displacement between the bottom surface and top surface of the fat pad or joint.

A two degrees of freedom model with linear springs and nonlinear dashpot was selected as a more simple and reasonable model as shown in Figure 4.4. The equations of motion derived with Lagrange's equations are as follows:

$$\begin{aligned} m_S \ddot{y}_1 + c_T\left(\dot{y}_1 - \dot{y}_2\right) + k_T\left(y_1 - y_2\right) &= 0, \\ m_F \ddot{y}_2 - c_T\left(\dot{y}_1 - \dot{y}_2\right) - k_T\left(y_1 - y_2\right) + c_F\left(\dot{y}_2 - \dot{y}_0\right) + k_F\left(y_2 - y_0\right) &= 0, \end{aligned} \tag{4.26}$$

where m_S is the mass of the shank, m_F is the mass of the foot, y_1, y_2 and y_0 are the displacements at the Medial Malleolus, the bottom of the foot bones, and the base respectively, k_T and c_T are the spring and damping constants for the ankle joint between the tibia and foot bones respectively, and k_F and c_F are the spring and damping constants for the fat pad below the foot bones respectively.

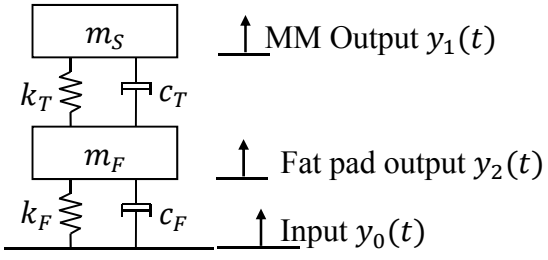

Figure 4.4 Two degrees of freedom model with linear springs and nonlinear damping.

The following relative displacement was defined and applied to the equations of motion

$$z_1 = y_1 - y_2,\ z_2 = y_2 - y_0,$$

$$m_S \ddot{y}_1 + c_T \dot{z}_1 + k_T z_1 = 0,$$

$$m_F \ddot{y}_2 - c_T \dot{z}_1 - k_T z_1 + c_F \dot{z}_2 + k_F z_2 = 0. \tag{4.27}$$

Using several relationships of the relative displacement, the equations of motion were modified

$$y_1 = z_1 + y_2,\ y_2 = z_2 + y_0,$$

$$m_S \left(\ddot{z}_1 + \ddot{z}_2 + \ddot{y}_0 \right) + c_T \dot{z}_1 + k_T z_1 = 0,$$

$$m_F \left(\ddot{z}_2 + \ddot{y}_0 \right) - c_T \dot{z}_1 - k_T z_1 + c_F \dot{z}_2 + k_F z_2 = 0. \tag{4.28}$$

The final equations of motion are

$$\ddot{z}_1 = \frac{1}{m_F}\left(c_F \dot{z}_2 - c_T \dot{z}_1 - k_T z_1 + k_F z_2 \right) - \frac{1}{m_S}\left(c_T \dot{z}_1 + k_T z_1 \right),$$

$$\ddot{z}_2 = \frac{1}{m_F}\left(c_T \dot{z}_1 - c_F \dot{z}_2 + k_T z_1 - k_F z_2 \right) - \ddot{y}_0. \tag{4.29}$$

The state-space form of the derived equations is

$$\begin{Bmatrix} \dot{x}_1 \\ \dot{x}_2 \\ \dot{x}_3 \\ \dot{x}_4 \end{Bmatrix} = \begin{bmatrix} 0 & 0 & 1 & 0 \\ 0 & 0 & 0 & 1 \\ -\dfrac{\left(m_S + m_F\right)k_T}{m_S m_F} & \dfrac{k_F}{m_F} & -\dfrac{\left(m_S + m_F\right)c_T}{m_S m_F} & \dfrac{c_F}{m_F} \\ \dfrac{k_T}{m_F} & -\dfrac{k_F}{m_F} & \dfrac{c_T}{m_F} & -\dfrac{c_F}{m_F} \end{bmatrix} \begin{Bmatrix} x_1 \\ x_2 \\ x_3 \\ x_4 \end{Bmatrix} + \begin{bmatrix} 0 \\ 0 \\ 0 \\ -1 \end{bmatrix} \ddot{y}_0, \tag{4.30}$$

where

$$x_1 = z_1,\ x_2 = z_2,\ x_3 = \dot{x}_1 = \dot{z}_1,\ x_4 = \dot{x}_2 = \dot{z}_2.$$

Because major transmissibility of vibration occurred at the Medial Malleolus as shown in Chapter 2, the acceleration at the Medial Malleolus was considered for the output. From Eq (4.27), the observation which is the output at the Medial Malleolus can be derived as follows:

$$\ddot{y}_1 = -\frac{1}{m_S}\left(c_T x_3 + k_T x_1\right). \tag{4.31}$$

The selected combination of linear spring constants and nonlinear damping constants (Eq 4.18) were utilized for the derived model. The nonlinear damping constants c_T and c_F are as follows:

$$c_T = c_{11} e^{-c_{12} x_1} \cos\left(c_{13} x_1\right),$$

$$c_F = c_{21} e^{-c_{22} x_2} \cos(c_{23} x_2). \tag{4.32}$$

The equations of motion can be expressed as a nonlinear SISO (single input and single output) state-space form

$$\dot{x}(t) = F\left(t, x(t), u(t), \alpha\right),\ x(t_0) = x_0,$$

$$y(t) = H\left(t, x(t), u(t), \alpha\right), \tag{4.33}$$

where F is a nonlinear function for states, H is a nonlinear function of outputs, t is the current time, u is the input vector, and α is a vector of parameters.

4.5 Parameter estimation

In the derived equations for the foot and ankle, several constants (k_T, k_F, c_T, and c_F) were left as unknown constants since it is hard to measure them directly. Those

unknown parameters and initial conditions were estimated using the derived equations and measurements.

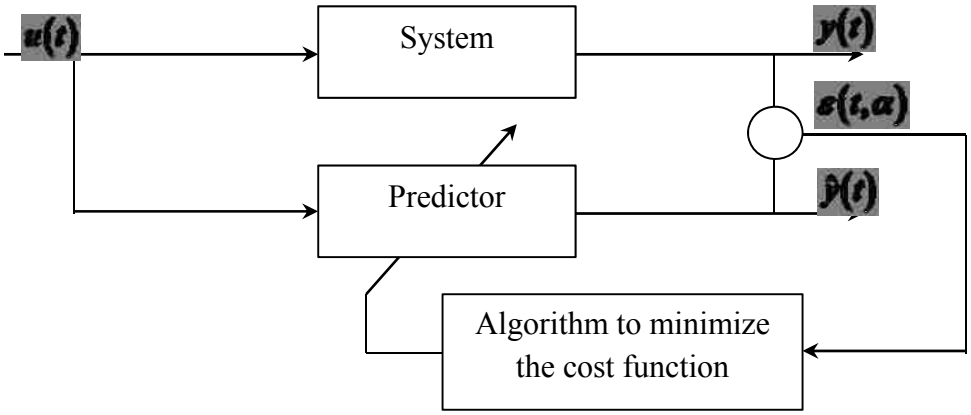

Figure 4.5 The process of the parameter estimation [9].

The estimating system was represented with the derived nonlinear SISO state-space equations (Eq (4.33)). The Prediction Error Method (PEM) was utilized for the parameters estimation, and the flow diagram of the estimation procedures are shown in Figure 4.5. The experimental results were obtained from the data from Chapter 2 which measured the input and output acceleration at the base plate and Medial Malleolus respectively. In the predictor, the derived equations of motion were solved with initial guess values for unknown parameters using ODE 45 (Runge-Kutta 45 ordinary differential equations solver in Matlab). After solving ODEs, the estimated output ($\hat{y}(t)$) was compared with the measured output ($y(t)$) and, the prediction error ($\varepsilon(t,\alpha)$) was calculated. The prediction error and the cost function, which is a quadratic function of parameters (α), are as follows:

$$\varepsilon(t,\alpha) = y(t,\alpha) - \hat{y}(t),$$

$$V_N(\theta) = \frac{1}{N}\sum_{t=1}^{N}\left(\varepsilon(t,\alpha)\right)^2. \tag{4.34}$$

The cost function (objective function; nonlinear grey box model) was minimized with the trust-region reflective Newton method of nonlinear least-squares (Optimization Toolbox of Matlab 2011a) [63]. The general formulation of nonlinear least-squares is defined by

$$\min_x \|F(x)\|_2^2 = \min_x \sum_i F_i^2(x) \tag{4.35}$$

with constraints such that $lb \le x \le ub$, where x is a vector, $F(x)$ is a function of a vector, and lb, ub are the lower and upper boundaries respectively [64]. The trust-region reflective Newton method is a kind of search method. The trust region is defined as the neighborhood N (n space) around a point x which approximates the behavior of a function F with a simple function q. In here, the function q is the quadratic function derived by the first two terms of the Taylor approximation of F at the point x. The minimization of function $F(x)$ was computed with a trial step using the trust-region subproblem defined by [63]

$$\min_s \{q(s), s \in N\}. \tag{4.36}$$

If $F(x+s) < F(x)$, the current point is updated as a new point ($x+s$), and if $F(x+s) > F(x)$, the current point is not changed and the trust-region was updated with the reduced region. The trial step is repeated to find the minimization value [64].

The trust-region-reflective method can be developed more from Eq (4.36) and described by

$$\min_{\|D_s\| \le r} \left\{ \frac{1}{2} s^T H s + s^T g \right\} \tag{4.37}$$

where D_s is a diagonal scaling matrix, r is the radius of the two-dimensional subspace (s), g is the gradient of F at the current point x, H is the Hessian matrix of F at the current point x, and $\|.\|$ is the 2-norm [63]. Solving Eq (4.37) is performed by the computation of a full eigensystem and a Newton process applied to the following equation

$$\frac{1}{r} - \frac{1}{\|s\|} = 0. \tag{4.38}$$

The two-dimensional subspace s is defined with the linear space spanned by s_1 and s_2. The s_1 is the direction of gradient of g, and s_2 is a solution to (an approximate Newton direction)

$$H \cdot s_2 = -g \tag{4.39}$$

or a direction of negative curvature [64]

$$s_2^T \cdot H \cdot s_2 < 0. \tag{4.40}$$

The process of minimization with the trust-region reflective method is summarized with the following steps [63]:

1. Defining the two-dimensional trust-region subproblem.
2. Solve Eq (4.37) to determine the trial step s.
3. If $F(x+s) < F(x)$, x is updated as $x + s$.

4. Update r.

These steps are repeated until the minimization is converged.

The criterion for the optimization was defined with the trace of the weighted prediction error matrix represented as follows:

$$\text{trace}\left(E' * E * W\right), \tag{4.41}$$

where E represents the prediction error matrix and W is a positive semi-definitive symmetric matrix [63]. Since the weighted matrix W was assumed with an identity matrix, Eq (4.41) was simplified as the traditional least-sum-of-squared-error.

In order to give constraints for some parameters, measurement results from other literatures were utilized. The stiffness of the heel pad has been measured in several conditions such as compression or vibration. *In vitro* vibration tests [59, 64], the stiffness was around 1160 kN/m at body weight, and it was not dependent on the applying frequency. The measured stiffness with *in vivo* impact test was about 150 kN/m at body weight loading and increased as the frequency was increased [64]. Even though a study showed the stiffness was dependent on the location of foot bottom [60], in this study, the material properties of the front fat pad and heel fat pad were assumed as the same values for the simplified model. Based on this information, k_F was constrained in the range of 3000-10e5 N/m for the estimation procedure.

In the derived equations, the masses of foot and shank were calculated by the anthropometric data [32]: the foot mass is 0.0145 × total body mass, and the shank mass is 0.0465 × total body mass. The other parameters to express mechanical properties such as spring constants and damping constants were estimated with the parameter estimation methods mentioned above.

The estimation of the unknown parameters has been done with the grey box parameter estimation (System Identification toolbox of Matlab 2011a) [9]. Since the optimization convergence for the parameter estimation is very dependent on the initial guess value, the temporary set of the initial guess values was selected for the trial error method. The fitting percentage between the measurement and estimation was calculated with Eq (3.20).

4.6 Results

As an estimation example, the results of subject # 16 were shown in Figures 4.6-4.14. The poor fitting results were shown as the initial guess value was tested, but the estimated model through the optimization process was well-matched with the experimental results. At lower frequencies from 10 to 20 Hz, the fitting percentage between the experimental results and the estimation results was less than comparing with the higher frequencies since the experimental results at those frequency ranges had more nonlinearity.

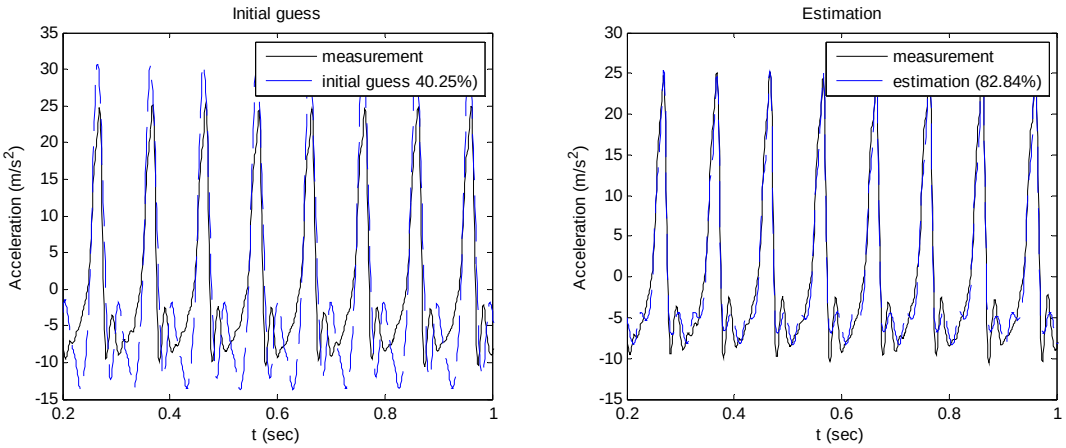

(a) 10 Hz without an extra mass

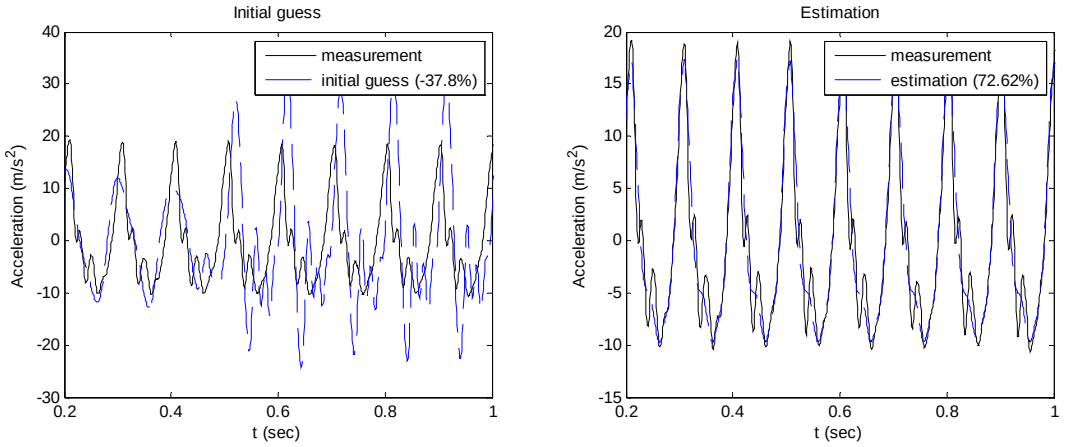

(b) 10 Hz with 2.3 kg mass

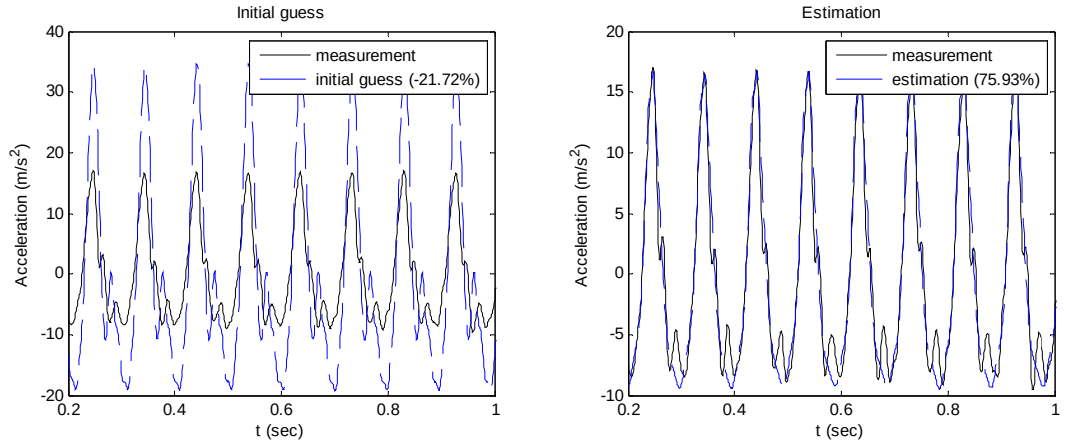

(c) 10 Hz with 4.5 kg mass

Figure 4.6 The estimated results according to the applied mass at 10 Hz (Subject # 16).

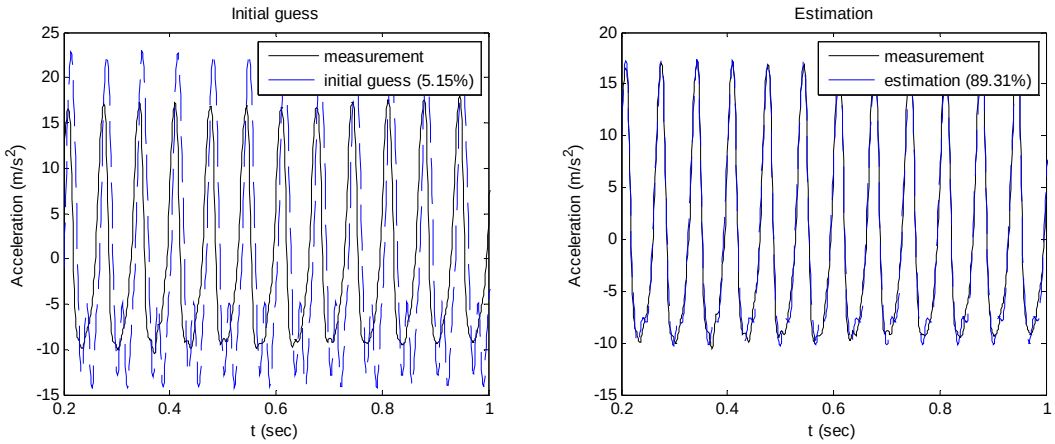

(a) 15 Hz without an extra mass

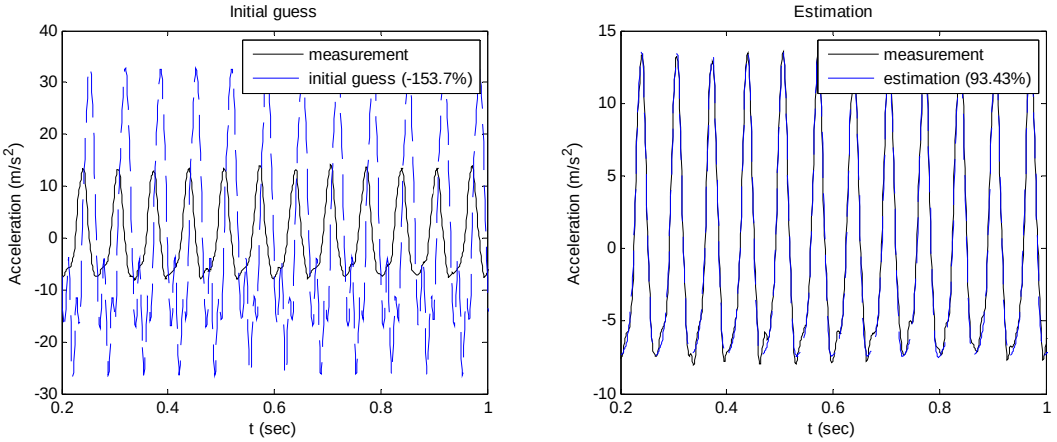

(b) 15 Hz with 2.3 kg mass

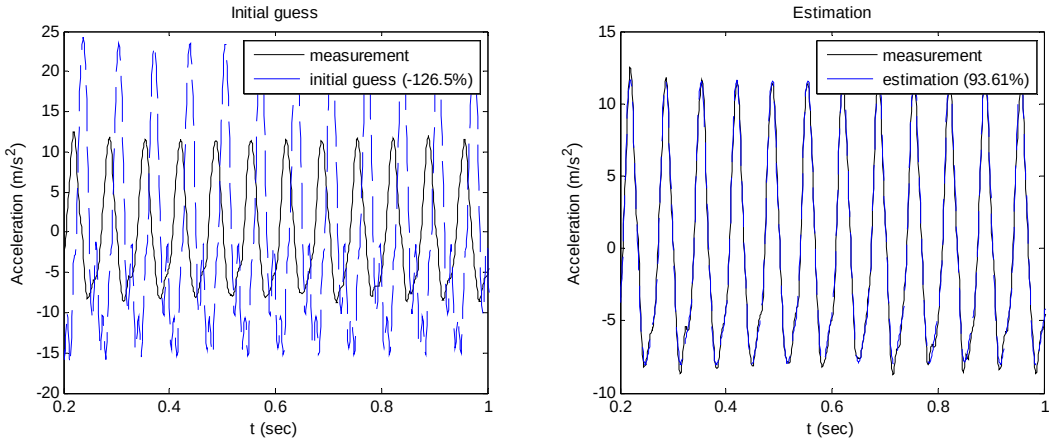

(c) 15 Hz with 4.5 kg mass

Figure 4.7 The estimated results according to the applied mass at 15 Hz (Subject # 16).

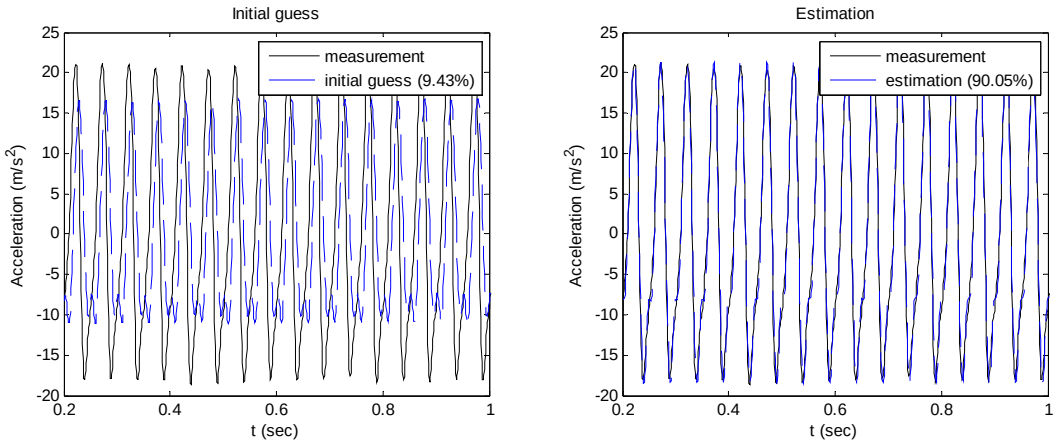

(a) 20 Hz without an extra mass

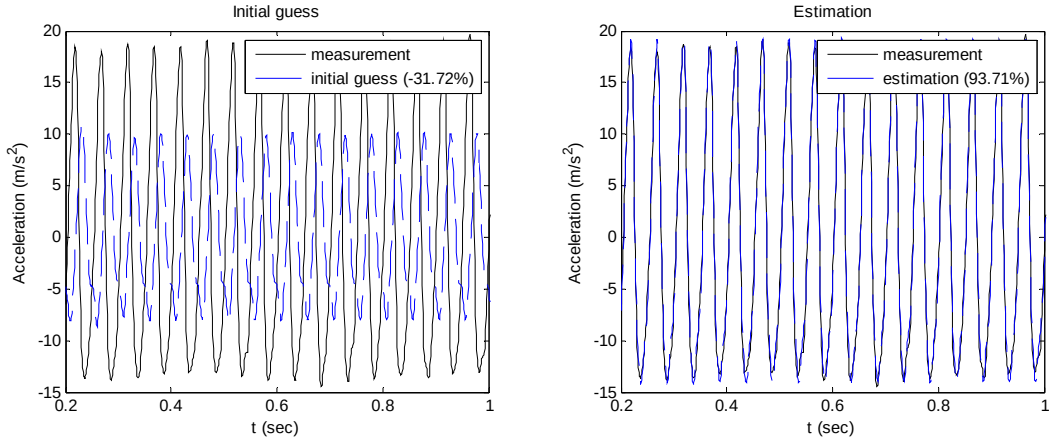

(b) 20 Hz with 2.3 kg mass

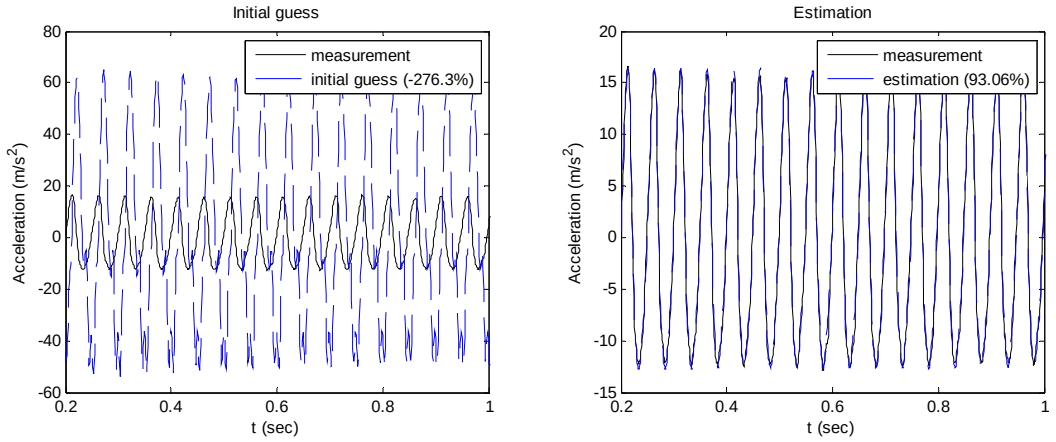

(c) 20 Hz with 4.5 kg mass

Figure 4.8 The estimated results according to the applied mass at 20 Hz (Subject # 16).

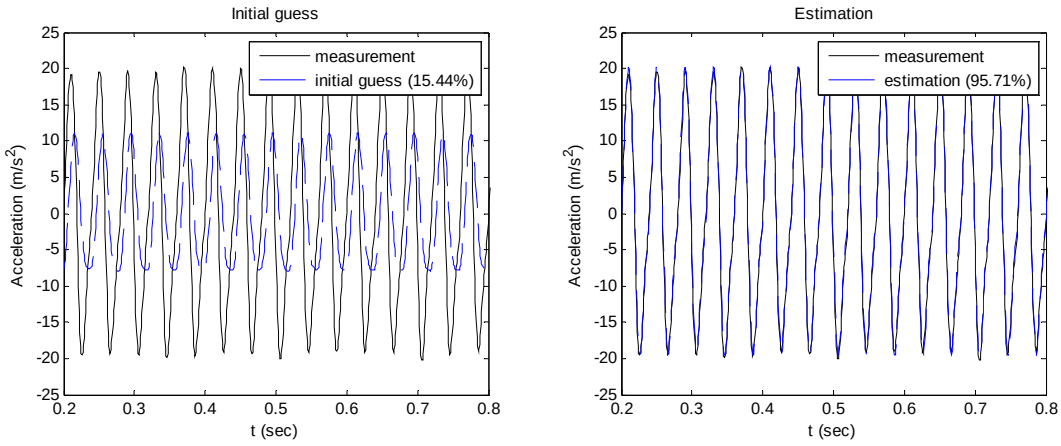

(a) 25 Hz without an extra mass

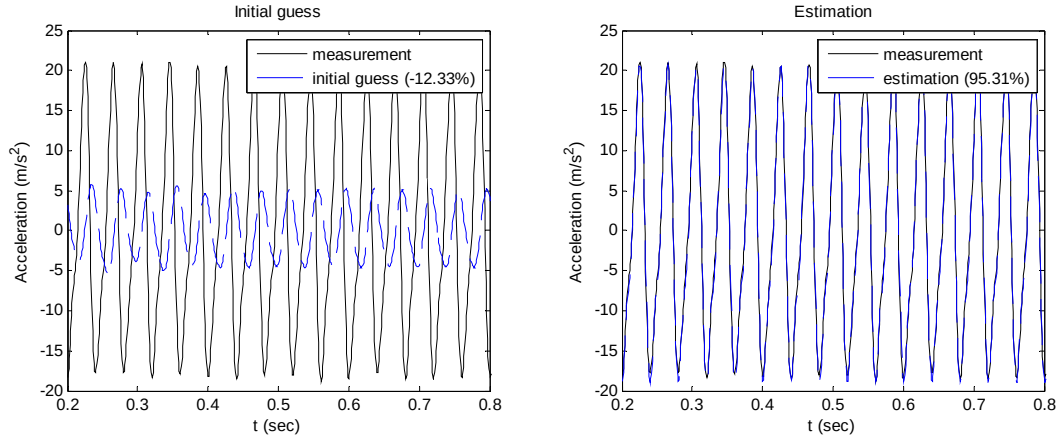

(b) 25 Hz with 2.3 kg mass

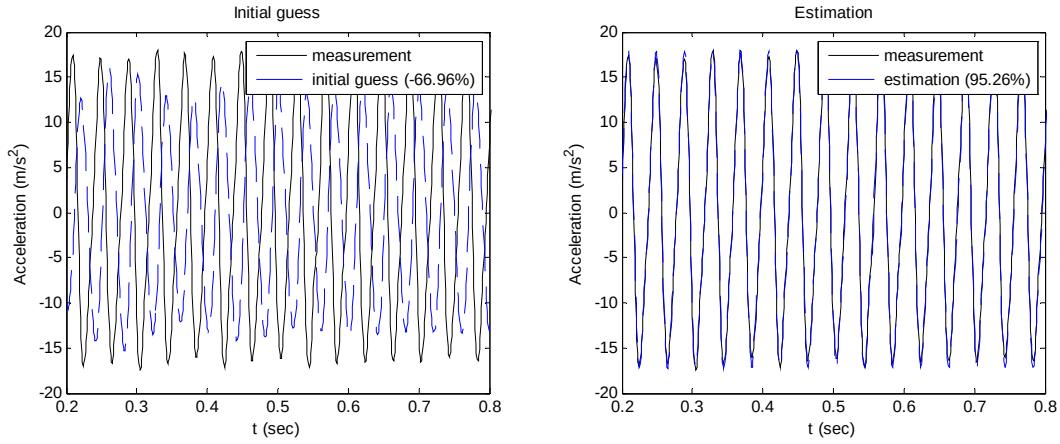

(c) 25 Hz with 4.5 kg mass

Figure 4.9 The estimated results according to the applied mass at 25 Hz (Subject # 16).

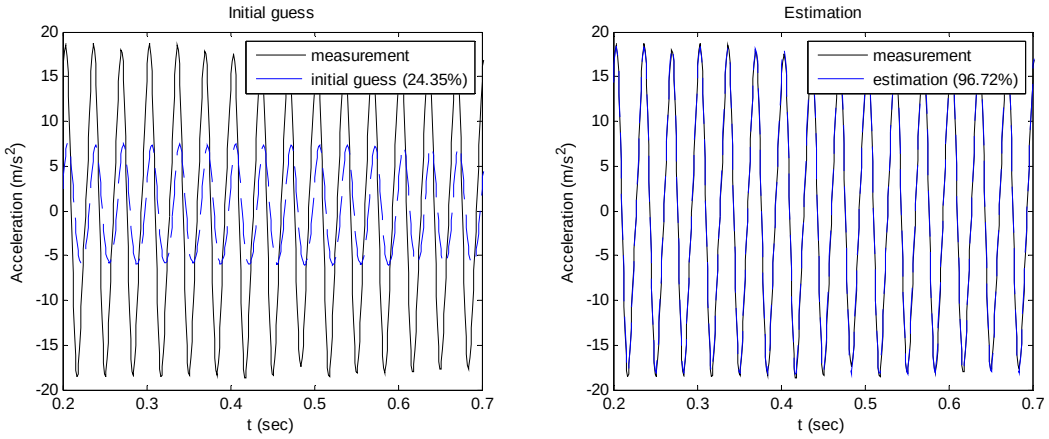

(a) 30 Hz without an extra mass

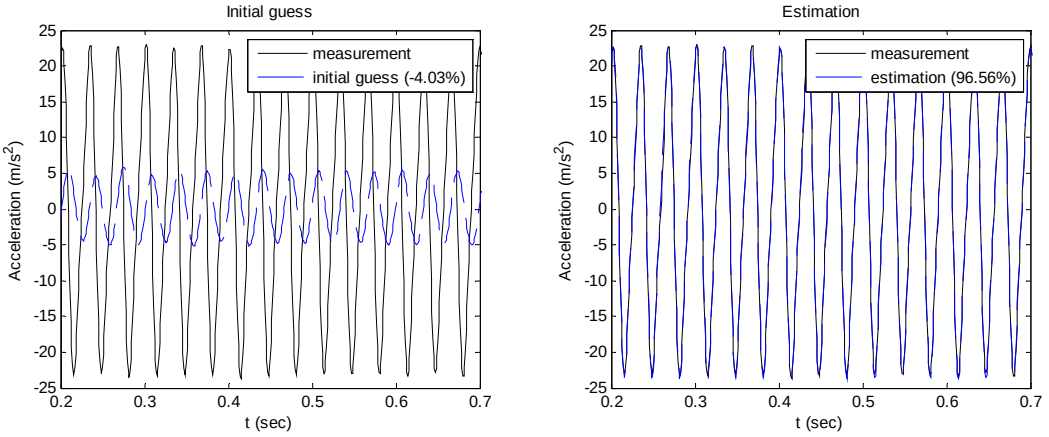

(b) 30 Hz with 2.3 kg mass

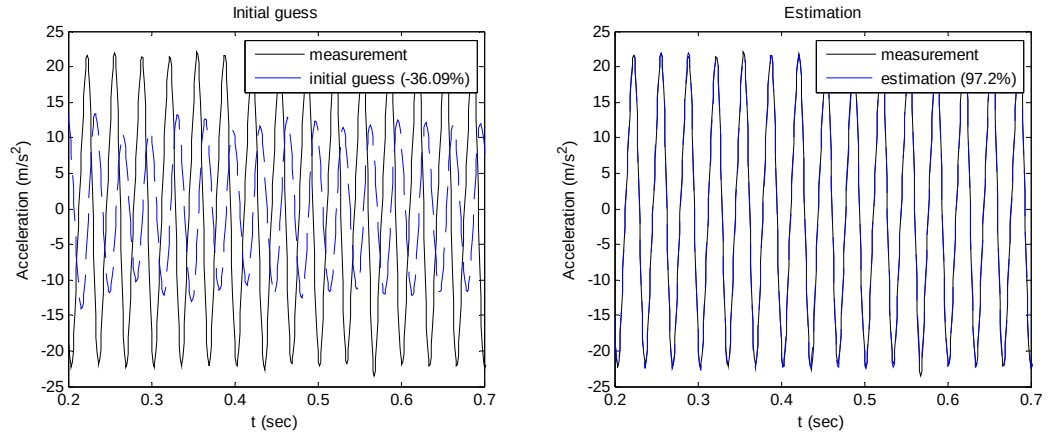

(c) 30 Hz with 4.5 kg mass

Figure 4.10 The estimated results according to the applied mass at 30 Hz (Subject # 16).

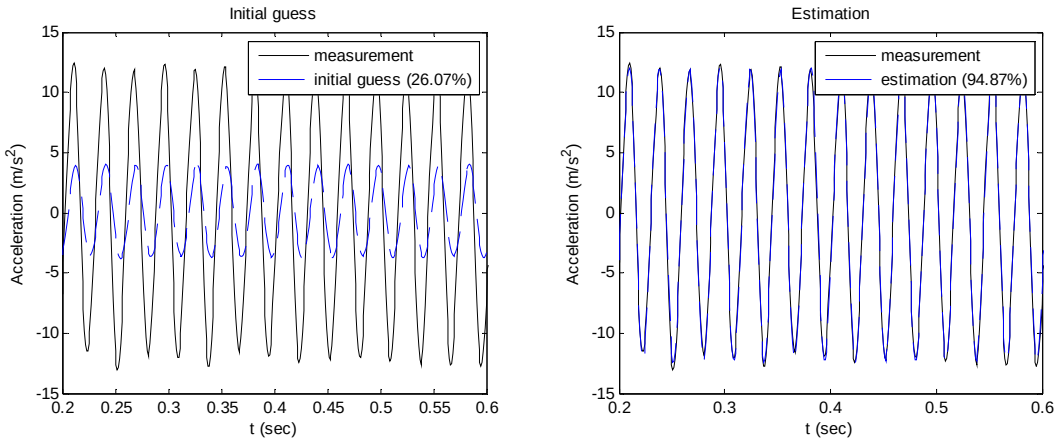

(a) 35 Hz without an extra mass

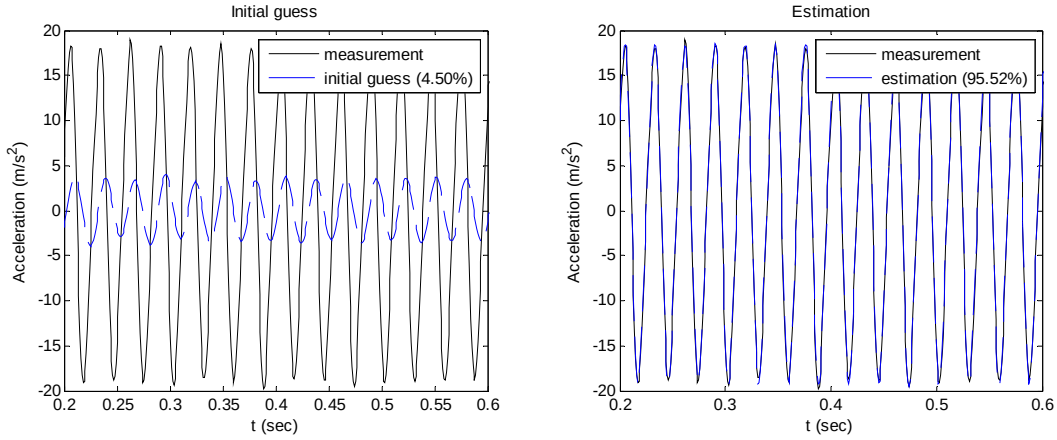

(b) 35 Hz with 2.3 kg mass

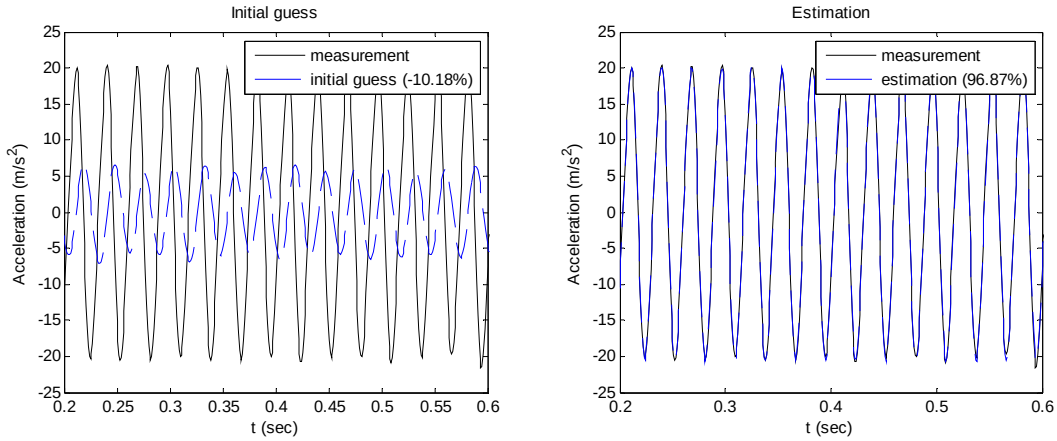

(c) 35 Hz with 4.5 kg mass

Figure 4.11 The estimated results according to the applied mass at 35 Hz (Subject # 16).

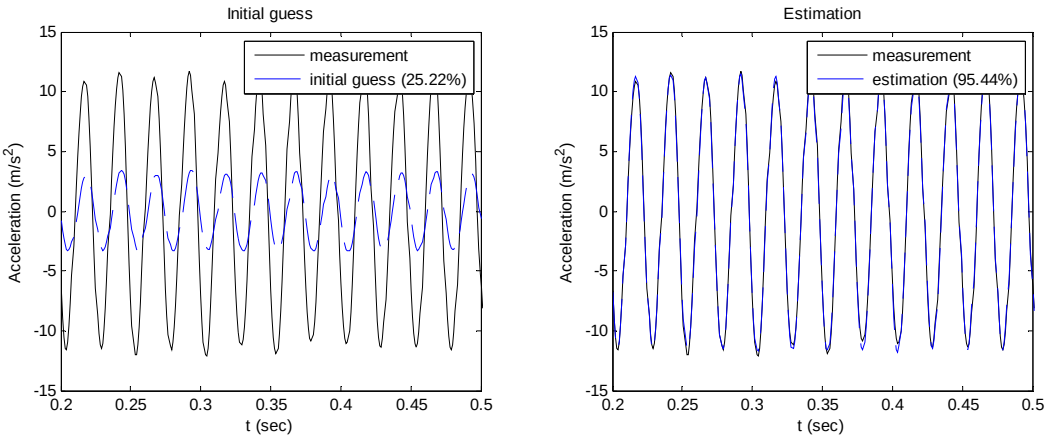

(a) 40 Hz without an extra mass

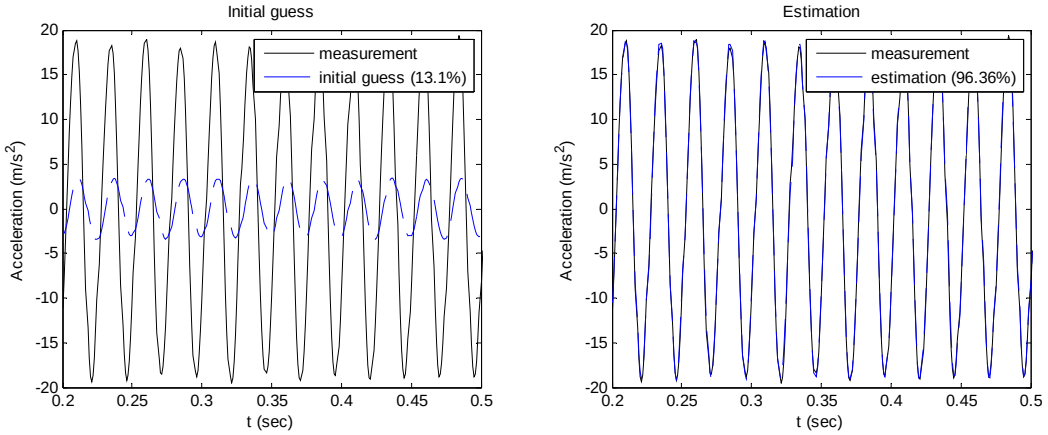

(b) 40 Hz with 2.3 kg mass

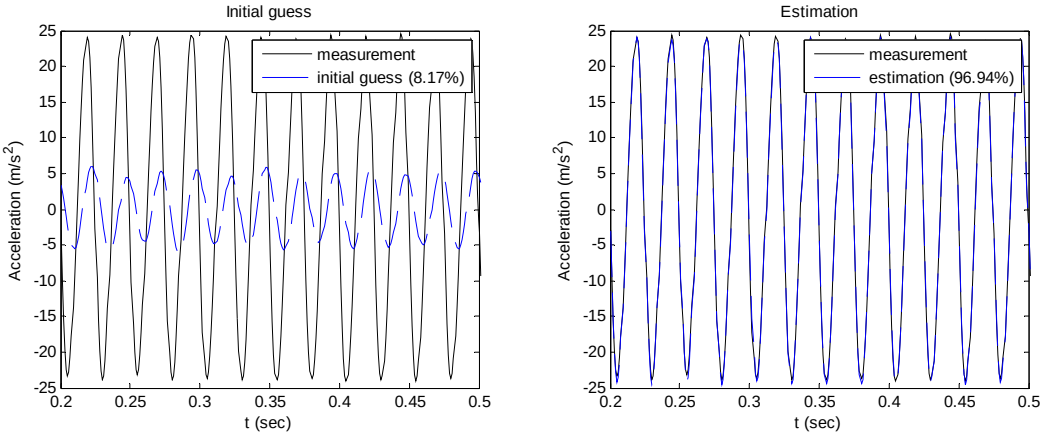

(c) 40 Hz with 4.5 kg mass

Figure 4.12 The estimated results according to the applied mass at 40 Hz (Subject # 16).

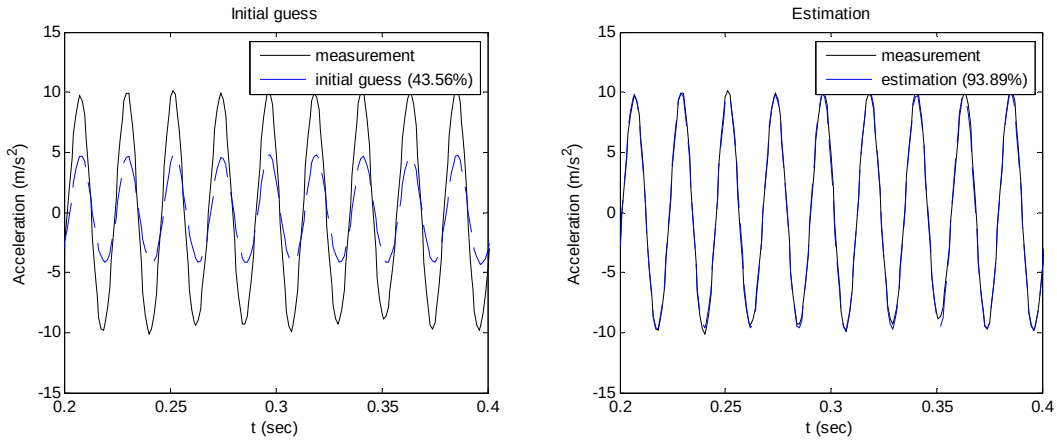

(a) 45 Hz without an extra mass

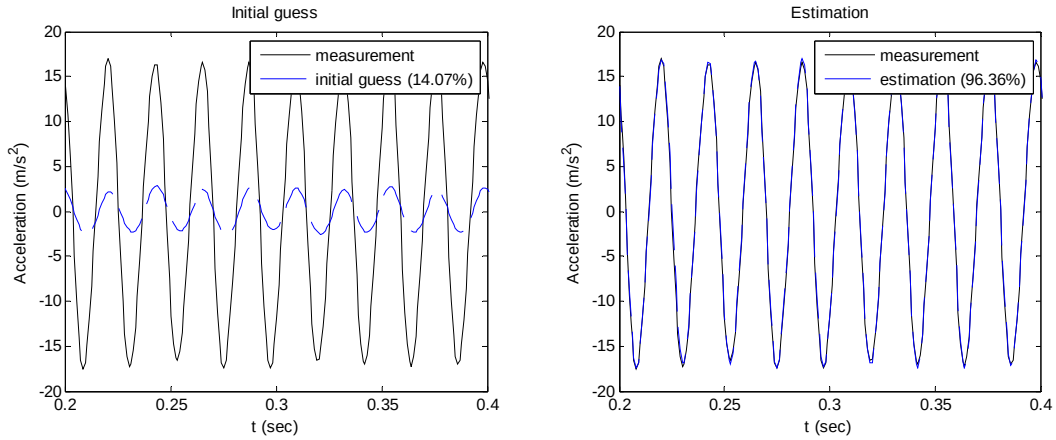

(b) 45 Hz with 2.3 kg mass

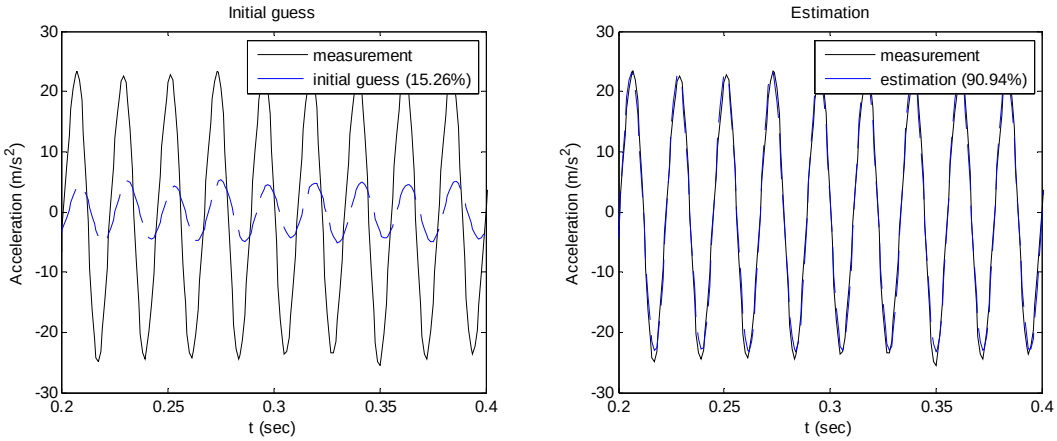

(c) 45 Hz with 4.5 kg mass

Figure 4.13 The estimated results according to the applied mass at 45 Hz (Subject # 16).

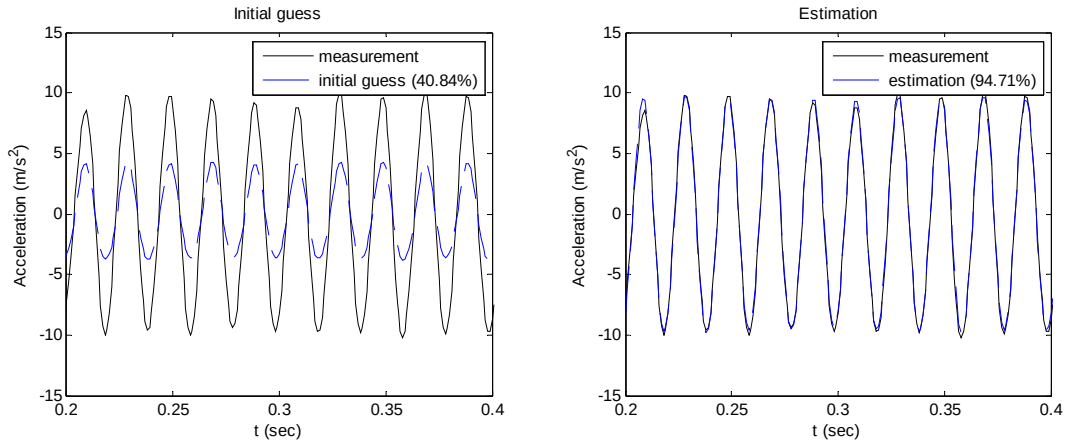

(a) 50 Hz without an extra mass

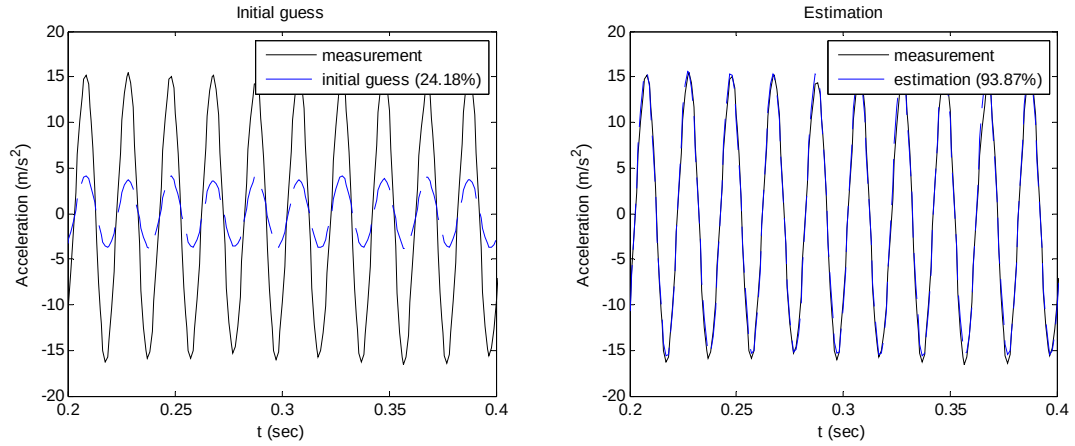

(b) 50 Hz with 2.3 kg mass

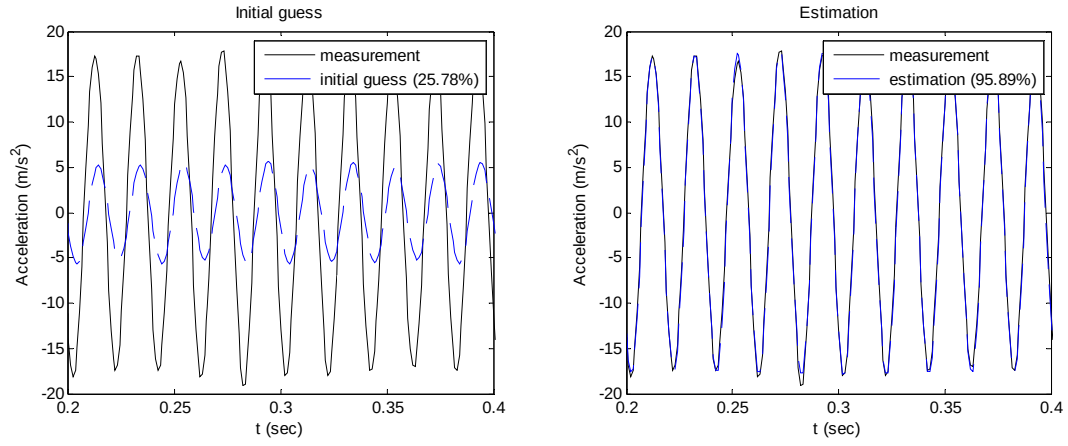

(c) 50 Hz with 4.5 kg mass

Figure 4.14 The estimated results according to the applied mass at 50 Hz (Subject # 16).

Based the estimated results of a subject (Subject # 16) the energy dissipation and damping characteristics were analyzed with the hysteresis behavior. The hysteric loops were presented with the force and the relative displacement relationship according to frequencies in Figures 4.15-4.17. The force between the tibia and talus (T) and between the bottom of bones and the fat pad (F) were calculated with the following equation

$$F_T = k_T x_T + c_T \dot{x}_T,$$

$$F_F = k_F x_F + c_F \dot{x}_F, \tag{4.42}$$

where c_T, c_F are defined in Equation (4.25), x is the relative displacement, and $\dot{x}$ is the relative velocity. The relative displacement and velocity were obtained by solving the ordinary differential equations.

The force-displacement was analyzed as functions of the input frequency and applied mass at the talocrural joint and fat pad model. In this hysteresis loop analysis (Figures 4.15-4.17), the area of the enclosed loop in the force-displacement graph means the total energy dissipated by the nonlinear viscoelastic model. The large dissipated energy, the enclosed area of the force-displacement graph, was observed in the fat pad viscoelastic material with comparison to the talocrural joint ((a) and (b) of Figures 4.15-17). The effect of the applied mass was manifest in both the fat pad and talocrural joints.

Without-mass case (Figure 4.15)

The dissipation energy of the talocrural joint was nonlinear, but it was changed linearly, like a spring, after 20 Hz (Figure 4.15 (a)). The fat pad dissipated input energy more in compression than that of the talocrural joint (Figure 4.15 (b)). The dissipation energy of the fat pad became the highest at 15 Hz and gradually decreased with the frequency increase. The major portion of work done by the input vibration was the fat

pad area since the enclosed area of the talocrural joint in force displacement was smaller compared to the fat pad model.

With-mass case (2.3 kg and 4.5 kg mass; Figure 4.16 and 17)

The shape of the enclosed area in the hysteresis loop was changed according to the external mass conditions. In the case with 2.3 kg mass, the small area of dissipation energy of the talocrural joint was observed in compression over 40 Hz (Figure 4.16 (a)). With increase of the mass (4.5 kg mass), the enclosed area of the force-displacement at the talocrural joint disappeared, and therefore dissipation energy of the talocrural joint could be ignored (Figure 4.17 (a)). The force-displacement of the fat pad showed that the lower frequencies had the relationship between higher displacement and lower force, and the higher frequencies had the relationship between lower displacement and higher force (Figure 4.16 (b)).

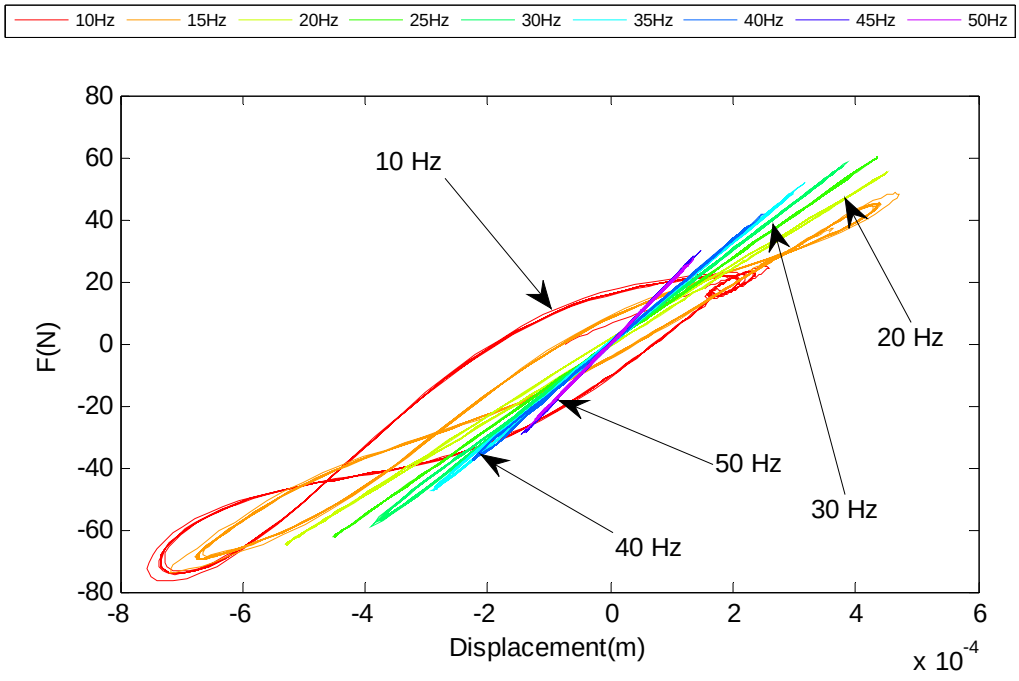

(a) The talocrural joint

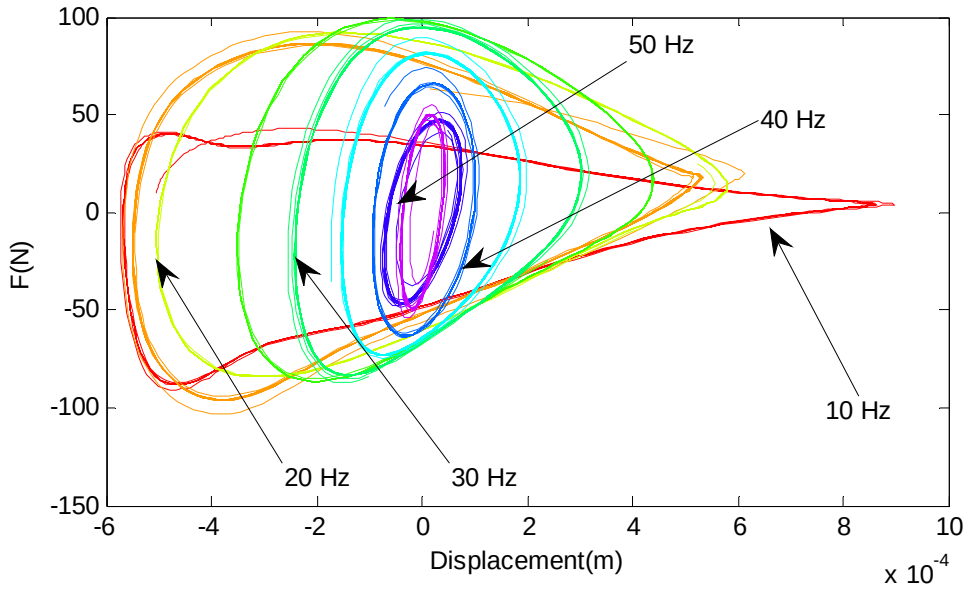

(b) The foot fat pad

Figure 4.15 Hysteresis behavior (force vs. displacement plot) of the estimated model without an extra mass.

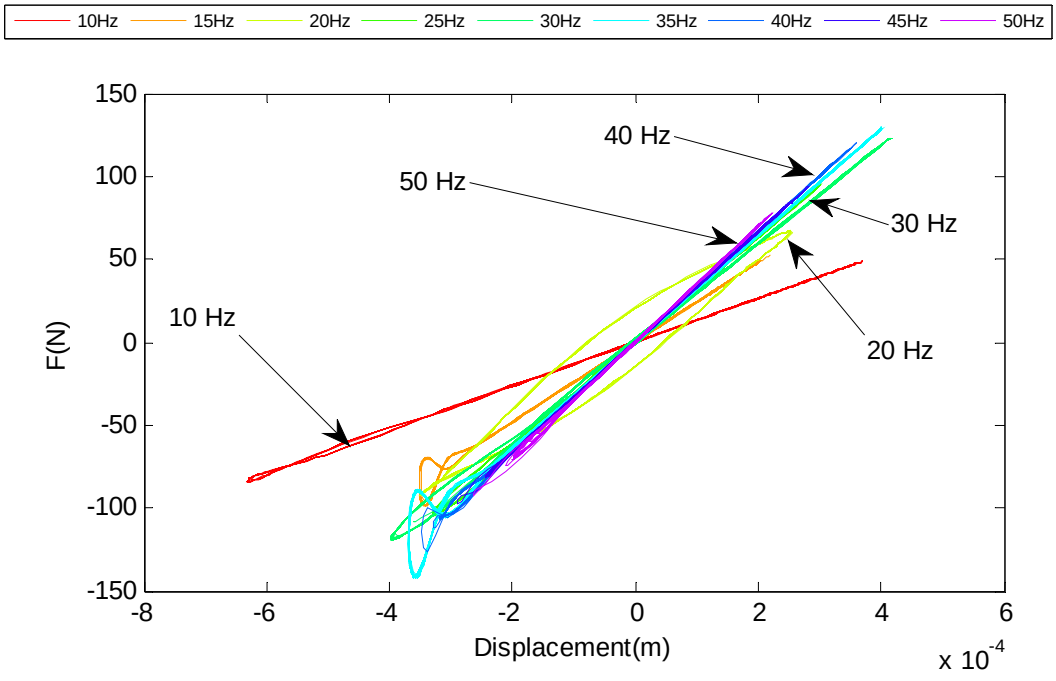

(a) The talocrural joint

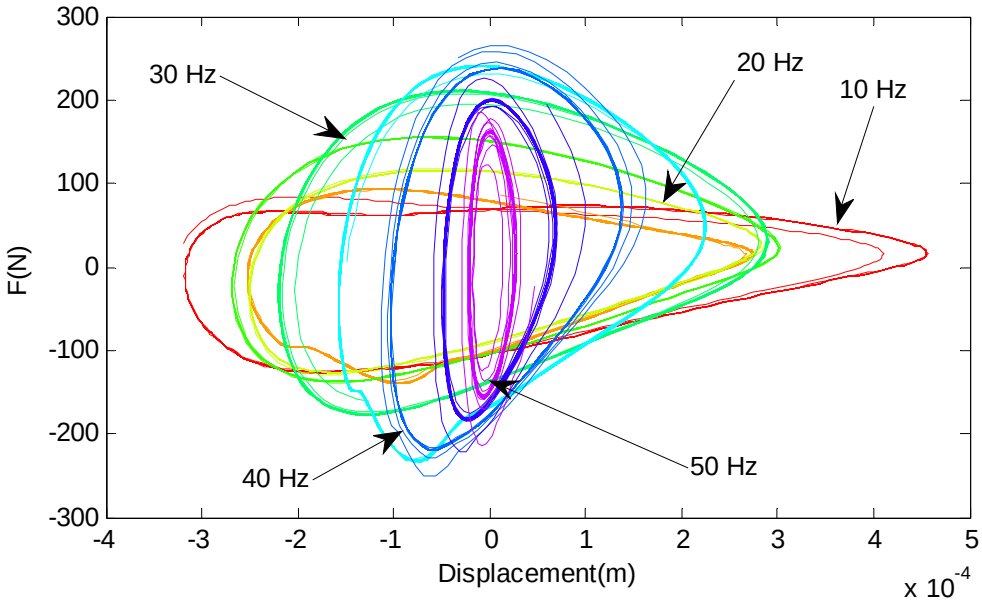

(b) The foot fat pad

Figure 4.16 Hysteresis behavior (force vs. displacement plot) of the estimated model with 2.3 kg mass.

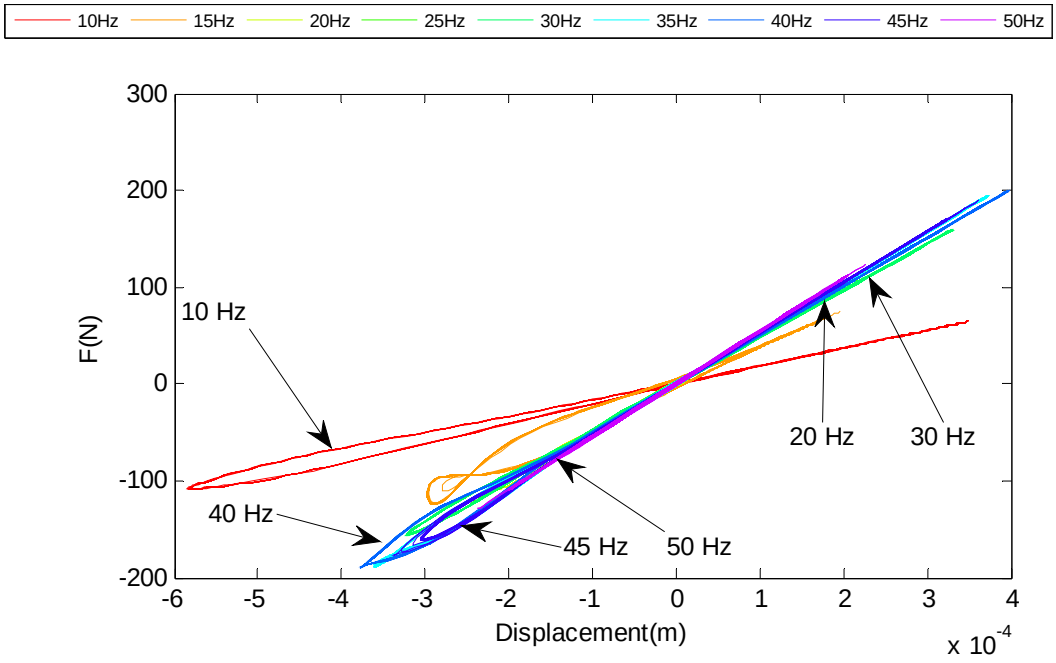

(a) The talocrural joint

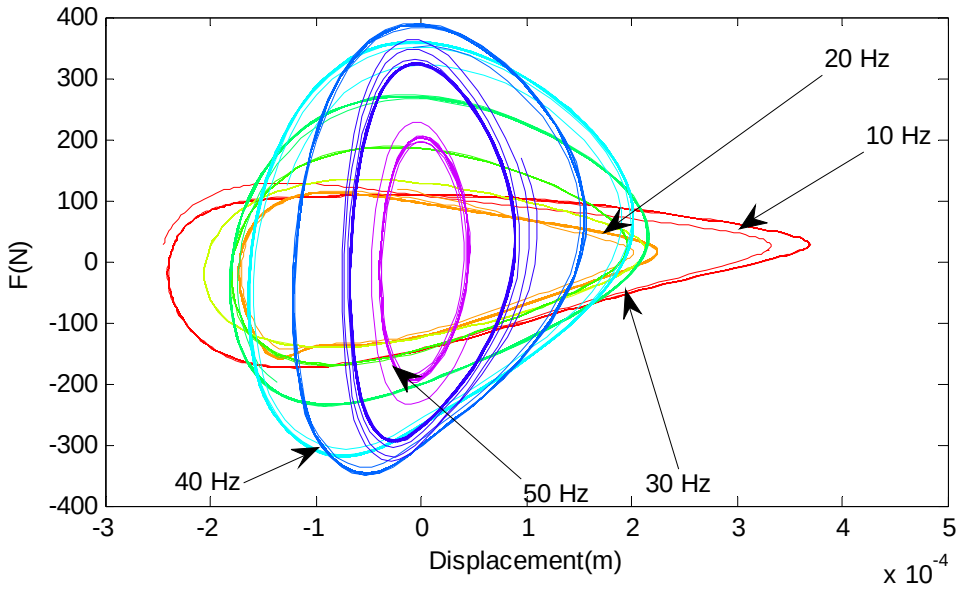

(b) The foot fat pad

Figure 4.17 Hysteresis behavior (force vs. displacement plot) of the estimated model with 4.5 kg mass.

The results of the parameter estimation showed that the estimated parameters (k_T, k_F, c_{11}, c_{12}, c_{13}, c_{21}, c_{22}, and c_{23}) of the derived equation (Eq (4.30) and (4.31)) varied according to the physical properties of the subjects as the output acceleration was different with each subject. The outlier data in the estimated parameters of 18 subjects were defined and removed with the box and whisker plot: the outliers were larger or smaller than 1.5×IQR (interquartile range $Q_3 - Q_1$, where Q_3 is the median of the upper half of the data set and Q_1 is the median of the lower half of the data set). The evaluations of outliers in the estimated parameters were shown in Figures D.1-D.3.

The spline fitted mean values of estimated parameters were calculated and compared with each mass case according to the frequencies. The estimated parameters for the joint between the tibia and talus (k_T, c_{11}, c_{12}, and c_{13}) are shown in Figures 4.18-4.21. The spring constant (k_T) of the talocrural joint was increased as the frequency and the applied mass was increased (Figure 4.18). The difference between the without-mass and the with-mass cases was small at 10 Hz, but it increased after 15 Hz. The amplitude of the damping constant (c_{11}) of the talocrural joint with mass showed higher value at lower frequency and decreased with the increase of frequency (Figure 4.19). The other constants (c_{12} and c_{13}) did not have a significant variation between without-mass and with-mass case (Figure 4.20 and 4.21). The damping capability of the talocrural joint was dependent on the spring constant (k_T) and the damping constant (c_{11}).

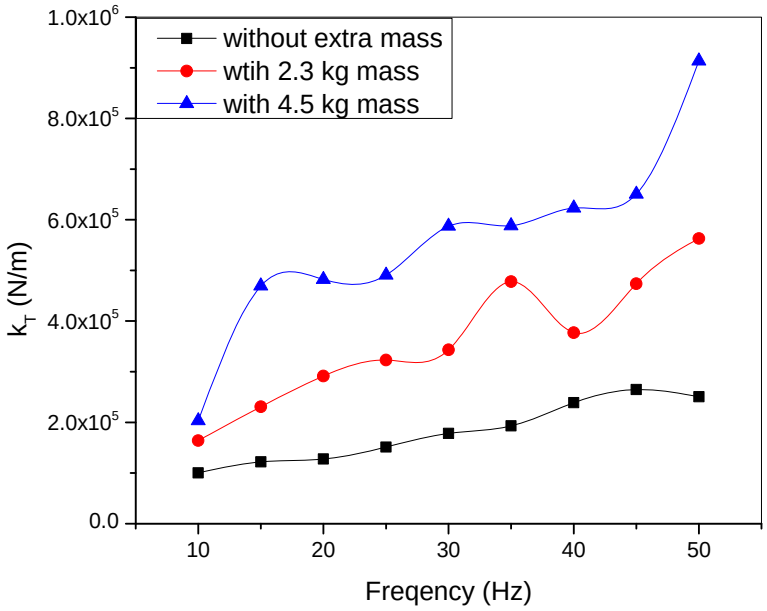

Figure 4.18 The mean value of the spring constants (k_T) of the talocrural joint.

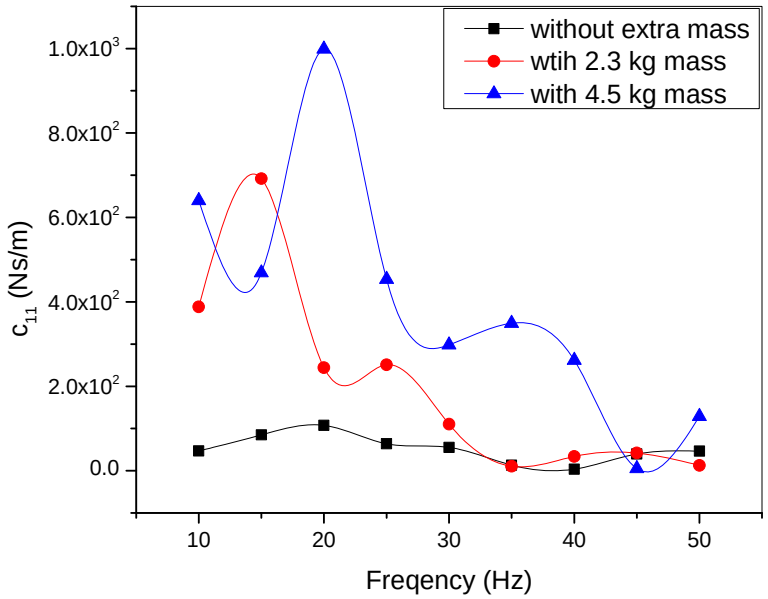

Figure 4.19 The mean value of the damping constants (c_{11}) of the talocrural joint.

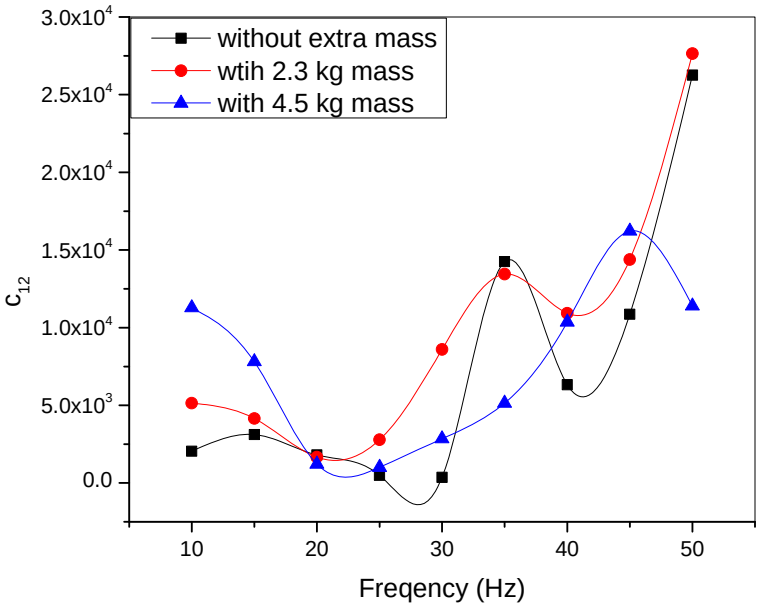

Figure 4.20 The mean value of the damping constants (c_{12}) of the talocrural joint.

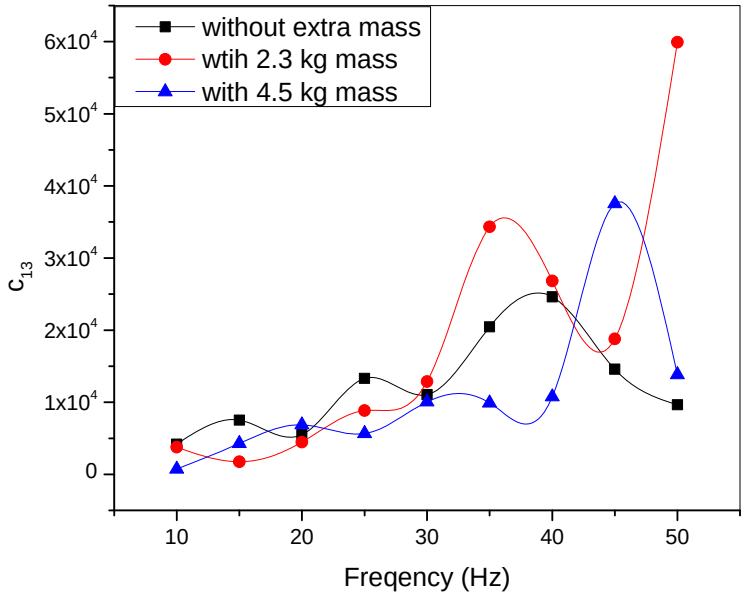

Figure 4.21 The mean value of the damping constants (c_{13}) of the talocrural joint.

Based on the estimated parameters, the talocrural joint was softer and had more damping at lower frequencies. The increase of mass and frequency made it stiffer and less damping. As a consequence, external vibration was transferred to the whole body since the vibration absorbing capability of the talocrural joint was decreased.

Similar to the talocrural joint, the increase of frequency and the applied mass influenced the spring constant (k_F) of the fat pad, which increased linearly as shown in Figure 4.22. It was supported by the experimental result in which the stiffness of the fat pad increased as the applied frequency was increased [60]. The k_F was increased gradually with lower slope compared to the slope of k_T.

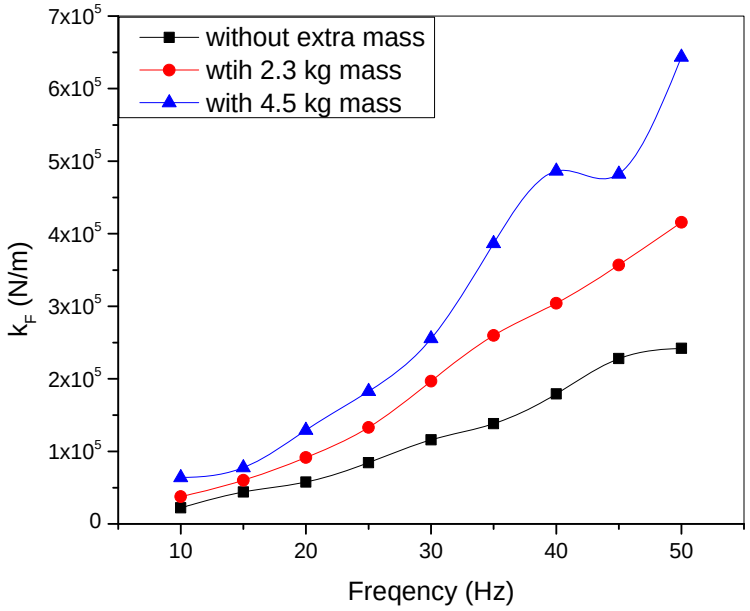

Figure 4.22 The mean value of the spring constants (k_F) of the foot fat pad.

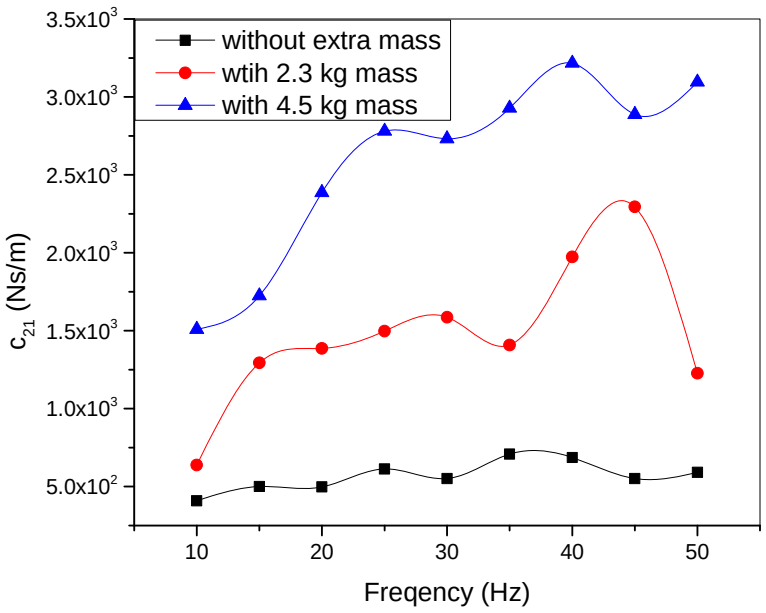

Figure 4.23 The mean value of the damping constants (c_{21}) of the foot fat pad.

The reverse trend was shown in the damping constant (c_{21}) of the fat pad compared to the damping constant (c_{11}) of the talocrural joint; c_{21} was increased with the frequency and the applied mass increase (Figure 4.23). Moreover, c_{21} had a higher magnitude than c_{11}. The increase of damping value followed the stiffness increase. This result shows that both the joint and the fat pad have different damping capabilities in lower and higher frequency ranges. The damping properties of the talocrural joint and the fat pad increased as the stiffness was increased in 10 - 15 Hz. As input frequency was increased, the fat pad represented a major portion of the damping capacity since the talocrural joint showed rigid body behavior (higher stiffness and lower damping).

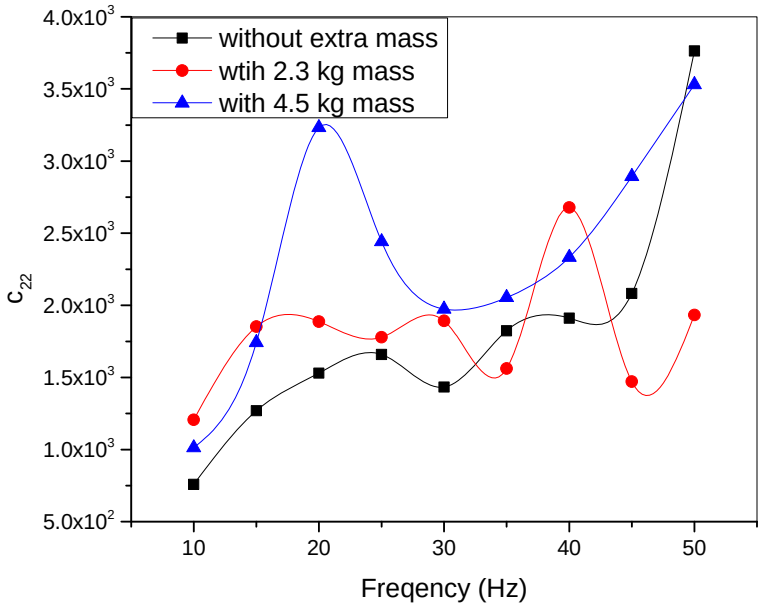

Figure 4.24 The mean value of the damping constants (c_{22}) of the foot fat pad.

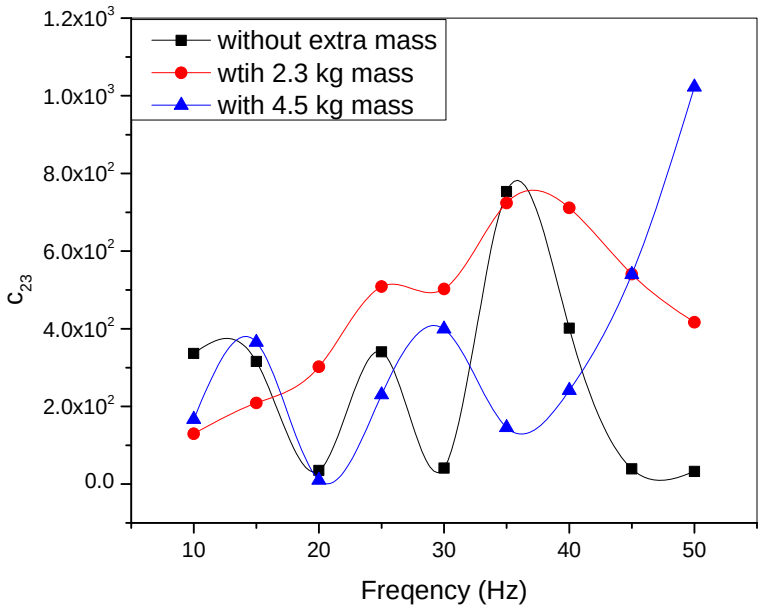

Figure 4.25 The mean value of the damping constants (c_{23}) of the foot fat pad.

There was no clear difference according to the applied frequency and mass in the damping constants c_{22} and c_{23} of the fat pad (Figure 4.24 and 4.25). Since two damping constants (c_{22} and c_{23}) were employed to control phase difference and acceleration slope of the output acceleration, they played a significant role in expressing the acceleration as the nonlinear acceleration output.

4.7 Conclusion

The medial arch of the foot and ankle was modeled with the complicated truss structure. It was utilized to express the vibration absorbing capability of the foot and ankle system. The equations of motion were derived with Lagrange's equations. However, there were some problems such as the complexity and expense in calculation to solve the derived equations. The sensitivity analysis was applied to find the sensitive parameters with respect to the states so that the complicated model was simplified as a two degrees of freedom model. The nonlinear damping constants were employed to express the nonlinearity of the measured acceleration at the fat pad and ankle joint. The viscoelastic parameters of the fat pad and ankle joint were estimated by trust region reflective Newton optimization method.

The simulations with estimated parameters were well-matched with the experimental data approximately 70-90 percentage fitting. The hysteresis loop analysis calculated with estimated constants showed the nonlinearity of the fat pad and talocrural joint as the damping values were proposed to follow the nonlinear output acceleration. Generally, the higher vibration absorbing capability was observed at the fat pad from the

hysteresis loop analysis since the dissipation energy of the talocrural joint was smaller than that of the fat pad. When the mass was applied to the system, the force was increased and displacement decreased as the function of frequency. This means that the foot and ankle system is more stressful with the increase of frequency if it has an additional load. The comparison between this study and other studies [59, 60, 65] in the force-displacement relationship of the fat pad showed a significant difference. This difference might be caused by the different type of input forces and loading conditions. However, the trend of estimated acceleration was similar to the stress results of viscoelastic models for ligaments under sinusoidal strain history [66].

The estimated spring and damping constants were compared as the function of frequency and the applied mass. Two viscoelastic parts (the talocrural joint and fat pad) were stiffer as the frequency was increased regardless of the applied mass conditions. For the talocrural joint, the damping properties were decreased with the frequency increase while the fat pad was more damping at higher frequencies. Based on this result, the vibration absorbing capability indicated that the talocrural joint and fat pad absorbed the vibration at lower frequencies. However, the increase of frequency caused the decrease of the vibration absorbing capability of the talocrural joint, and the vibration was absorbed more at the fat pad. The other damping constants (c_{12}, c_{13}, c_{22}, and c_{23}) were only involved with the phase delay and slope of the output acceleration without a clear trend.

CHAPTER 5

Modal analysis of a spread single bone cell using the Finite Element Method

5.1 Introduction

The structural behavior of bone cells under mechanical loadings is important to understand how forces are transferred to bone cells and influence bone cell growth. In order to demonstrate the relationship between bone formation and the type of stimulation, mechanical stimulation to bone cells has been widely investigated using experimental and numerical studies. For experimental measurements of bone cells exposed to mechanical stimuli, compression force, stretching, fluid shear stress, and vibration have been used as mechanical stimulation in the many studies [67-71]. Among those studies, several studies, which utilized vibration as mechanical stimulation, have investigated the frequency range and amplitude of the vibration optimal for the growth of bone cells [69-71].

Several elements, such as structural components, mechanical properties, and input loading types have to be considered in computational modeling of cells for better understanding of the response of bone cells to mechanical stimuli. Cell elements, such as cytoplasm, nucleus, membrane and the internal cytoskeleton (microtubules and microfilaments) have been generally employed for cell models. A spreading chick embryo fibroblast cell adhered to a substrate was modeled with three dimensional geometrical images [72, 73]. It included an elliptical nucleus, a dome shape cytoplasm covered with a membrane, and an internal cytoskeleton structure composed of a

tensegrity model. The tensegrity model consists of six struts, twenty-four cables, and twelve common nodes for microtubules, microfilaments, and actin filaments respectively. Nodal positions of the tensegrity model were adjusted to mimic a spreading cell shape. For focal adhesion sites, three nodes were constrained with three translation axes at the substrate surface. The nonlinear structural behavior of cells such as prestressed effects, strain hardening, variable compliance of the cell and the influence of mechanical property of cytoplasm were observed [72]. Using the same model, the response of bone cells with fluid shear stress and substrate strain loading were compared [73]. The deformation results showed that fluid flow shear stress resulted in a large vertical motion of the bone cell, the substrate strain generated deformation on the cell attachments. The additional results showed that the deforming effect of fluid flow shear stress was larger and more effective than the substrate strain loading case and that both mechanical stimuli played an independent role.

A brain cell under impact loading was analyzed to examine the effect of several mechanical properties and model structures such as with or without cytoskeleton model [74]. A round brain cell in suspension was modeled as tensegrity model (prestressed cytoskeleton), continuum model (cytoplasm, nucleus, and membrane), and combined model. The viscoelastic behavior was applied to the cytoskeleton and continuum system respectively to study its influence on the dynamic response. They showed that tensegrity and continuum model with viscoelastic characteristics affected the dynamic response, such as displacement fluctuation and deflection change, and concluded that a combined model of tensegrity and continuum system would be good to analyze the prestressed cytoskeleton structure in the time domain.

The cell strain distribution exposed to mechanical stimulation was investigated with the experimental method of Atomic Force Microscopy (AFM) and numerical simulation with Finite Element Method (FEM) and Computational Fluid Dynamics (CFD) [75]. Cell profiles and material property maps obtained by AFM were utilized to perform numerical simulations such as substrate stretch, fluid flow shear, intermittent hydrostatic pressure, microbead twisting, and micropipette poking. Measured small volume on the substrate was applied to the model of a cell and isotropic, linear elastic material properties were used. The effect of diverse mechanical stimuli, material property changes, Poisson ratio changes, the direction of application of stimulus, and fluid flow parameters were investigated.

In this work, the Finite Element modal analysis has been performed to find the natural frequency and mode shapes of a spreading bone cell model utilizing the ANSYS 12.1. This study reveals the dependence of natural frequency on cell shapes and Young's moduli of an adherent cell. These results are expected to serve as a reference in order to select the optimum frequency of the external vibrating loading in the future experimental research.

5.2 Modeling

In the bone cell culturing process, bone cells are adhering and spreading on a culturing plate after being seeded. The adhered shapes are various as shown in Figure 5.1 (a). In order to model an adherent cell, the geometry information was obtained from microscopy images [76, 77]. The ellipsoid shape and the height of a cell was selected

from Figure 5.1 (b) and (c). A bone cell adhered on the cell culture plate was considered as a simplified adherent ellipsoidal dome shape (Figure 5.2).

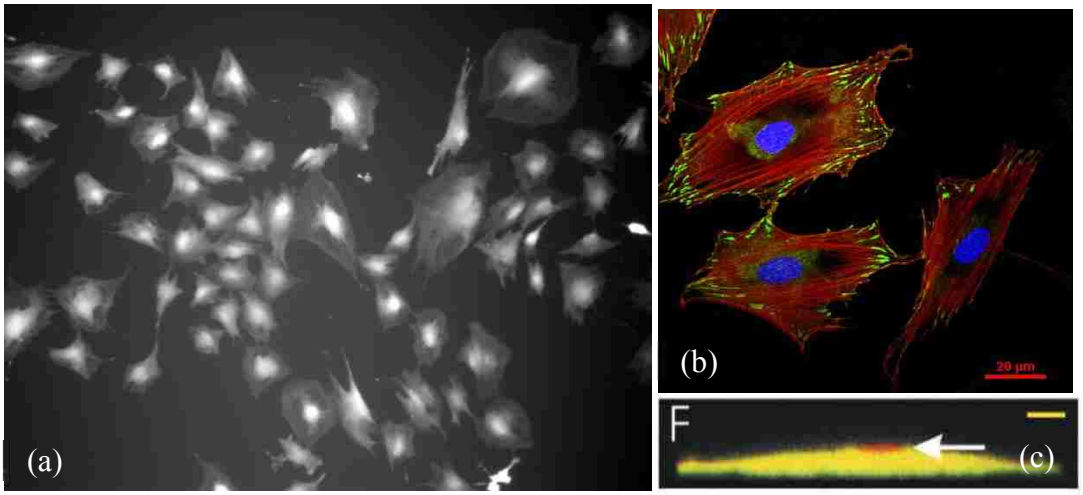

Figure 5.1 Culturing cells (a) various shapes of cells (b) ellipsoid shape of cells [76] (c) cross section of a cell [77].

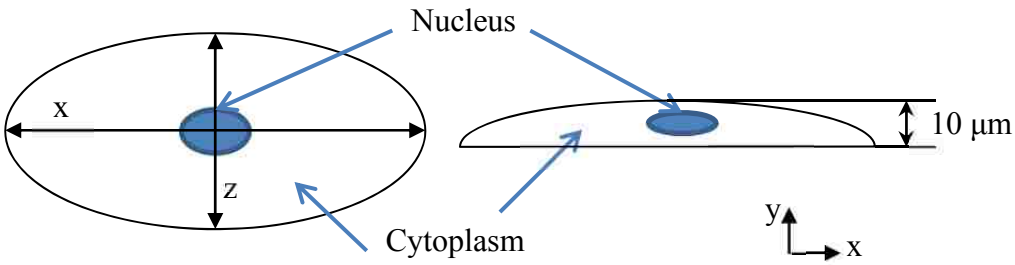

Figure 5.2 The simplified ellipsoid dome model of a cell.

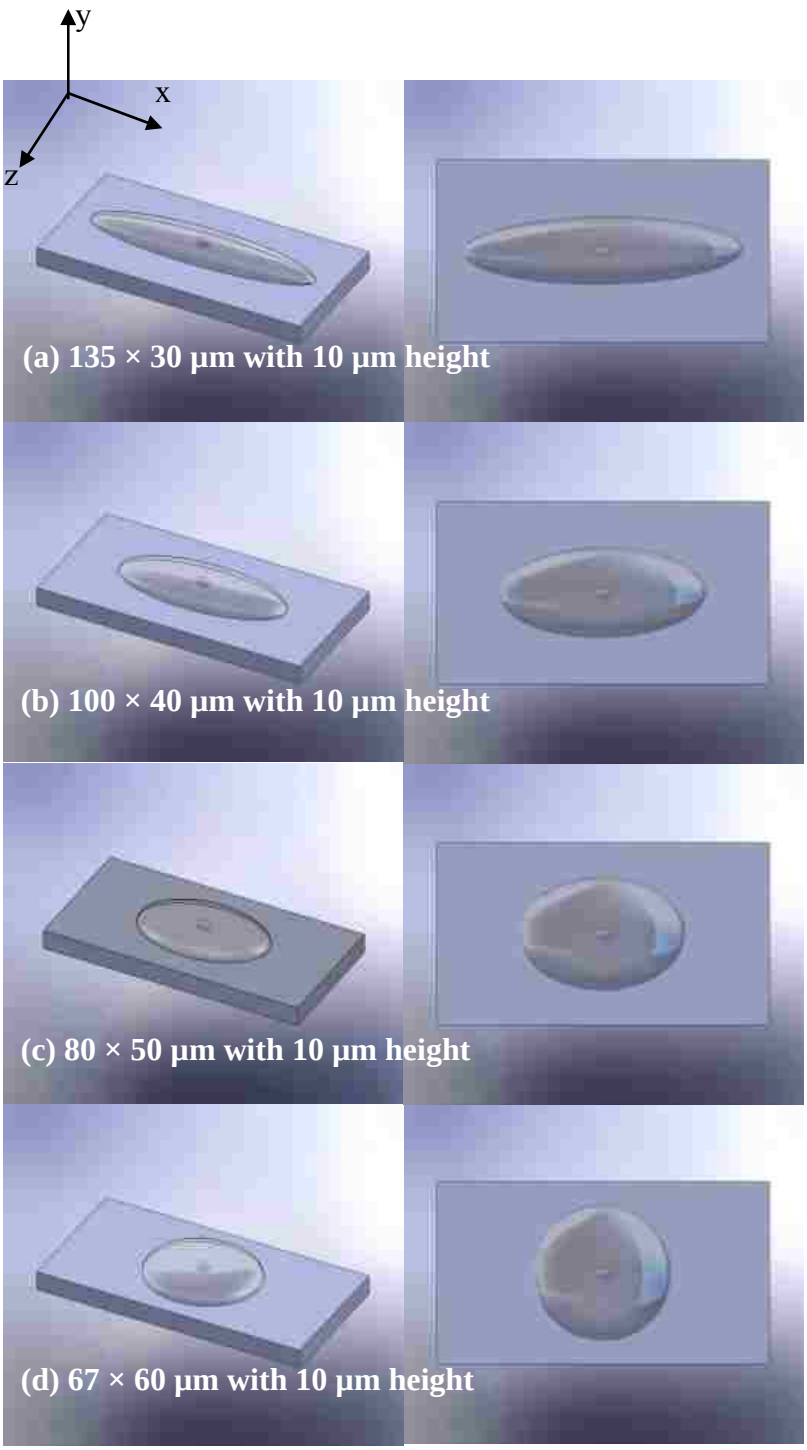

Figure 5.3 The four types of ellipsoidal dome shape models.

On the basis of available cell images the dimensions of adherent ellipsoidal dome structures were selected with the long (x) and short (z) axes equal to 135×30, 100×40, 80×50, and 67×60 μm with 10 μm height (y) (Figure 5.3). Even though the shape was changed, the volume of cytoplasm of all shapes was fixed as 1.9×10^{-14} m^3. The nucleus was also modeled as an ellipsoid with 8×5×5 μm (x×z×y) size, and its volume was 1.05×10^{-16} m^3. The center of the nucleus was floating at 4.5 μm from the base. In this study, the details of microtubules, microfilament, and cell membrane were ignored, and the cells were modeled as structures composed of cytoplasm and nucleus.

Several numerical studies [72, 73, 74] of cells exposed to mechanical stimuli utilized mechanical properties as shown in Table 5.1. Moreover, since the elastic modulus is significantly dependent on the cell type and the measurement method, several cases of the elastic moduli (30, 100, 500, 1000, 5000, and 15000 Pa) were selected for cytoplasm, and Poisson's ratio was selected as 0.37 based on these studies [72, 74]. The elastic modulus and Poisson's ratio of nucleus were selected to be 400 Pa and 0.37. The densities of cytoplasm and nucleus were calculated using the volume and mass of a typical human tissue cell [78]. They are 1.25×10^{-7} kg/m^3 for cytoplasm and nucleus.

For creating the Finite Element model, the ten-node (SOLID 187) high-order tetrahedral element was used to mesh cytoplasm and nucleus (Figure 5.4) [79]. Table 5.2. presents the mechanical properties utilized for the finite element analysis.

Table 5.1 Utilized material properties in cell modeling.

	Cell type	Model Components									
		Cytoplasm		Nucleus		Membrane		Microtubules		Microfilaments	
		*E (Pa)	**υ	E (Pa)	υ	E (Pa)	υ	E (Pa)	υ	E (Pa)	υ
[74]	Brain cell	100	0.37	400	0.37	10^3		1.2×10^9	0.3	2.6×10^9	0.3
[75]	Osteoblasts	10^3	0.3	N/A	N/A	N/A	N/A	N/A	N/A	N/A	N/A
[72]	Chick embryo fibroblast cell	100	0.37	400	0.37	10^3	0.3	1.2×10^9	0.3	2.6×10^9	0.3
[73]	Bone cells	100	0.37	400	0.37	10^3	0.3	1.2×10^9	0.3	2.6×10^9	0.3

*Elastic modulus, **Poisson's ratio.

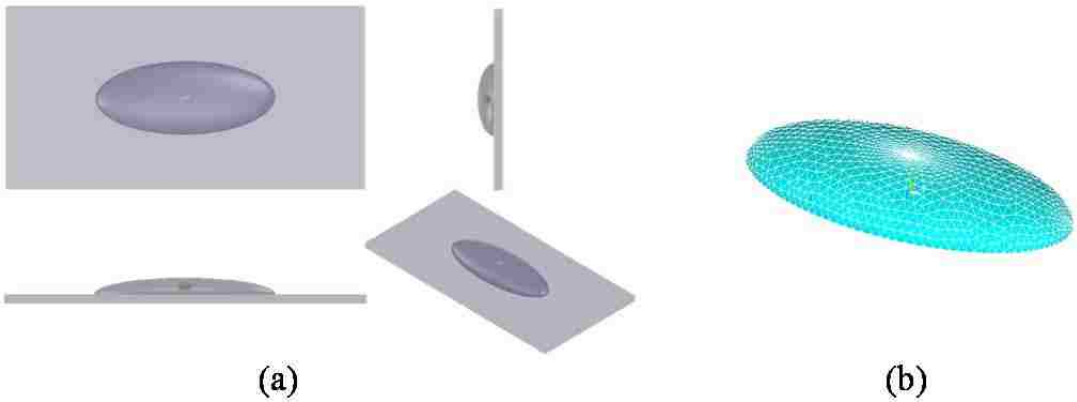

Figure 5.4 A spread bone cell model in culturing condition (a) an example (100×40 μm) of three-dimensional model, and (b) an example of the finite element mesh model.

Table 5.2 Material properties of each cellular component.

	Cytoplasm	Nucleus
Elastic Modulus (Pa)	30, 100, 1000, 5000, 10000	400
Poisson's ratio	0.37	0.37
Density (kg/m^3)	1.25e-7	1.27e-7

5.3 Modal analysis

The vibration characteristics of an adhered bone cell, such as the natural frequency and mode shapes, were calculated by the Finite Element modal analysis. Considering the single degree of freedom model, the general equation of motion is

$$[M]\{\ddot{x}\}+[C]\{\dot{x}\}+[K]\{x\}=\{F(t)\} \tag{5.1}$$

where $[M]$, $[C]$, $[K]$, and $\{F(t)\}$ are a mass matrix, damping matrix, spring matrix, and external force vector respectively. For modal analysis, Eq (5.1) was assumed as undamped free vibration and can be written as follows

$$[M]\{\ddot{x}\}+[K]\{x\}=0. \tag{5.2}$$

If the system undergoes a simple harmonic motion $\left(\{x\}=\{\Phi\}\sin(\omega t)\right)$, the following equation can be obtained:

$$\left([K]-\omega^2[M]\right)\{\Phi\}=0 \tag{5.3}$$

where ω^2 is eigenvalue, ω is frequency, and $\{\Phi\}$ is eigenvector [80].

The eigenvalues represent the natural frequency of the model, and the eigenvector represent the mode shape of the model. In this study, the eigenvalues were obtained by the Block Lanczos method that is a powerful method to calculate eigenvalues and eigenvectors for a given system [81]. Generally, a cell has a damping effect with its viscoelastic characteristics. But the damping effects were assumed be very small and ignored since the shape of a spread cell is very thin comparative to the in plane size. The bottom area of the model was constrained in translational x, y, and z directions. The number of modes to extract was chosen as ten in the range between 0 and 100 Hz.

5.4 Results

The solution of Finite Element analysis presented eigenvalues and eigenvectors. The extracted eigenvalues and eigenvectors represented the natural frequencies and corresponding mode shapes. The effect of cell shapes on the natural frequency was analyzed using an elastic modulus of 100 Pa. The first five modes for each shape among the extracted ten modes are shown in Figures 5.5-5.8. The mode shapes had similar trends although the mode shapes of some cases (the first mode of 80×50 μm, and the fourth and fifth mode of 135×30 μm) were different. The first and second modes showed one direction oscillation respectively in z and x directions. All shapes were oscillating in the same direction (z and x directions respectively for the first and second mode) (Figure 5.5, 5.6, and 5.8 (a)) while the opposite direction oscillation was observed in the shape of 80×50 μm (Figure. 5.7 (a)). The nucleus inside cytoplasm also followed the oscillation of cytoplasm. The third and fourth modes had two direction oscillations in z or x direction. In mode three, twisting oscillation about the y axis has been observed at the center part of the cytoplasm because of two opposite oscillations, and the nucleus was rotating about the y axis (Figures 5.5-5.8 (c)). The fourth mode was generating compression in the center area since two x direction oscillations were moving to the center simultaneously (Figures 5.5-5.8 (d)).

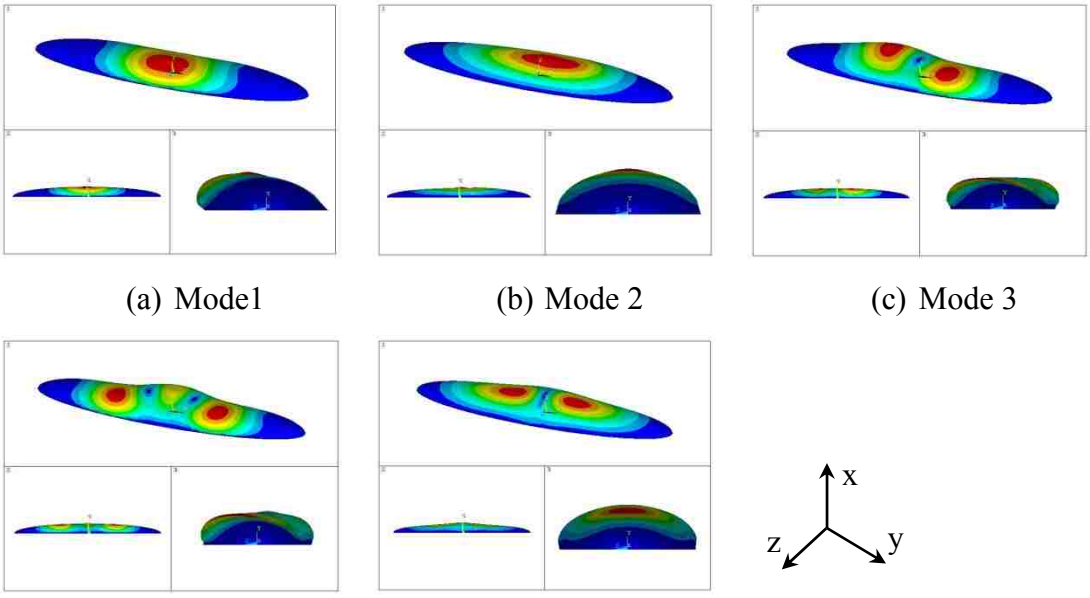

(a) Mode1 (b) Mode 2 (c) Mode 3

(d) Mode 4 (e) Mode 5

Figure 5.5 The modal analysis results for 135×30 μm with10 μm height and 100 Pa Young's modulus shape.

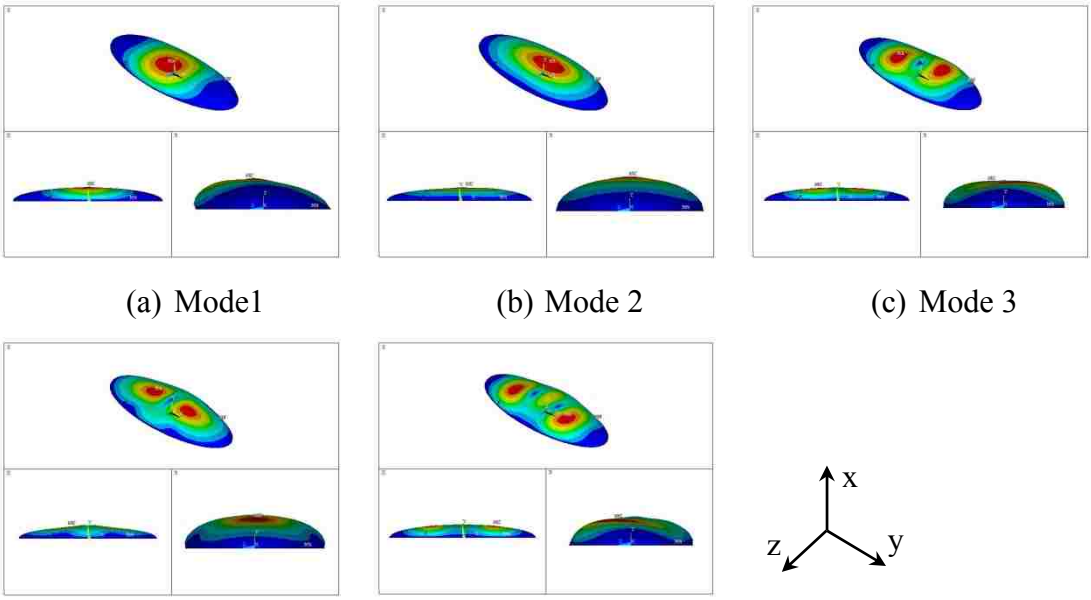

(a) Mode1 (b) Mode 2 (c) Mode 3

(d) Mode 4 (e) Mode 5

Figure 5.6 The modal analysis results for 100×40 μm with10 μm height and 100 Pa Young's modulus shape.

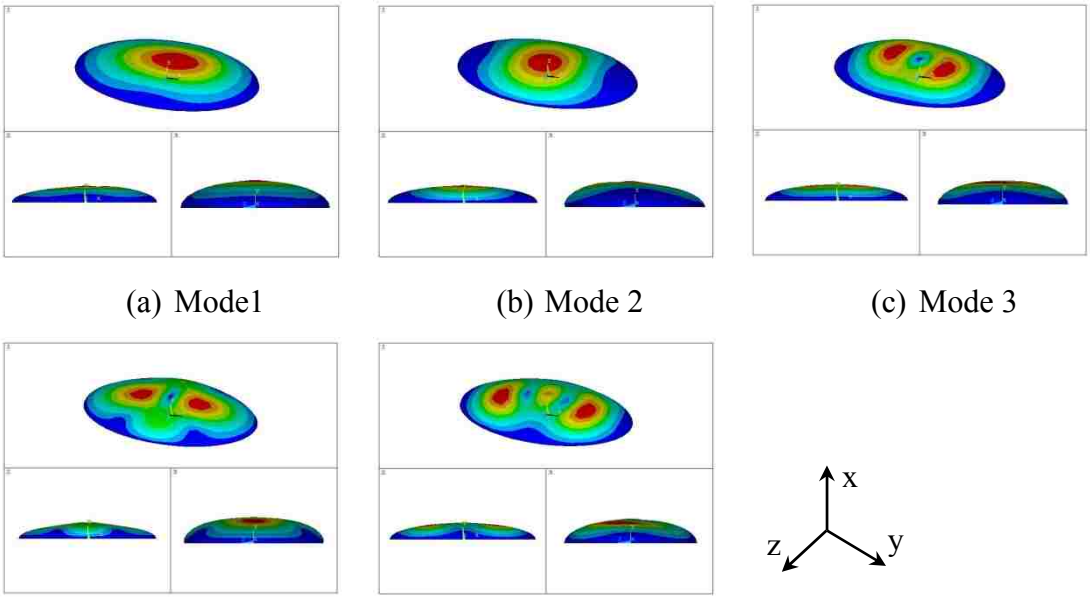

(a) Mode1 (b) Mode 2 (c) Mode 3

(d) Mode 4 (e) Mode 5

Figure 5.7 The modal analysis results for 80×50 μm with10 μm height and 100 Pa Young's modulus shape.

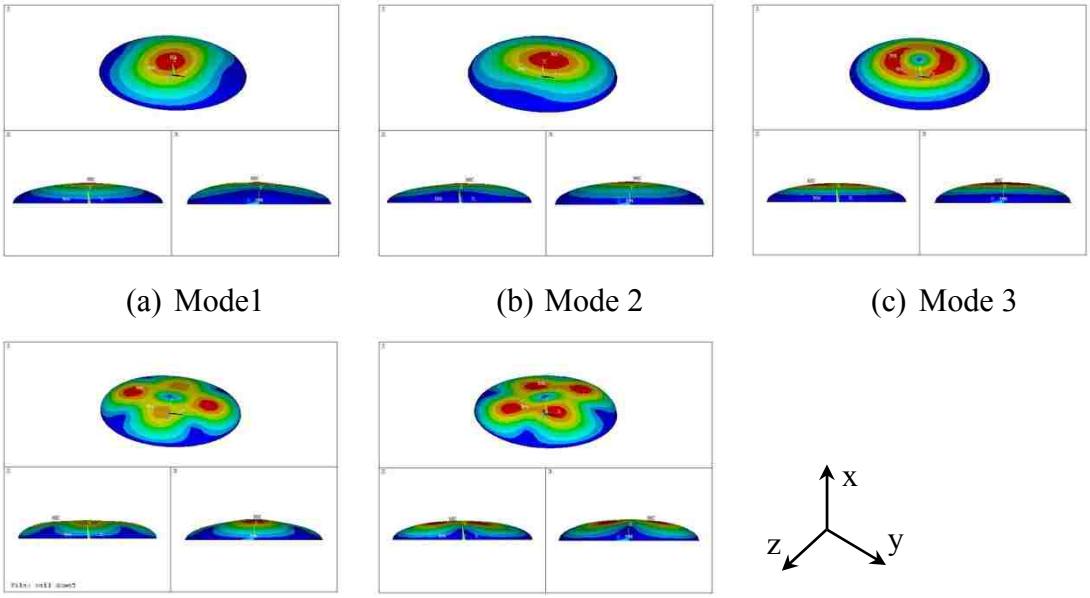

(a) Mode1 (b) Mode 2 (c) Mode 3

(d) Mode 4 (e) Mode 5

Figure 5.8 The modal analysis results for 67×60 μm with10 μm height and 100 Pa Young's modulus shape.

The variations of the natural frequency for each mode have shown slight differences among ellipsoidal shapes of the model. However, the natural frequencies as the function of an adhered cell shapes were in the similar range with the mean value from mode 1 to 10 of 18-25 Hz (Figure 5.9). The natural frequency of the first and second mode is 18.07 (±0.08) and 18.15 (±0.03) Hz. Above mode 3, the narrower the spreading shape is, the lower the natural frequency is.

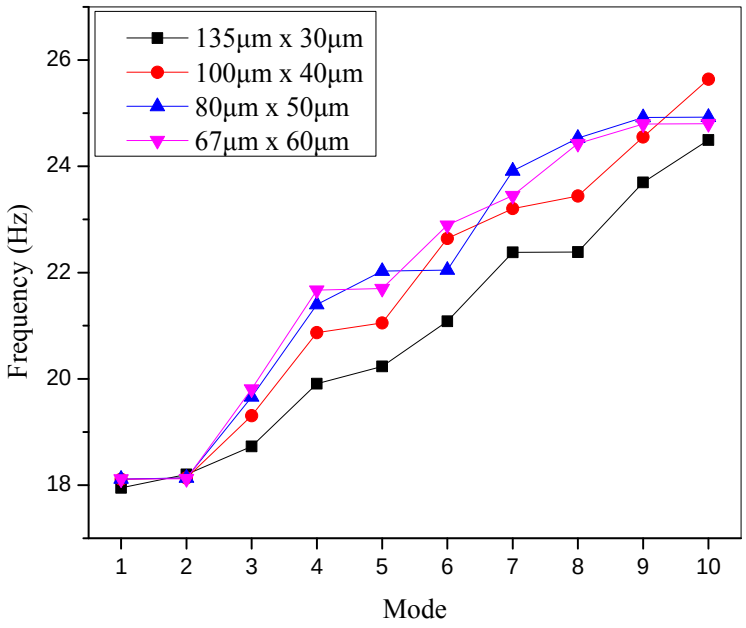

Figure 5.9 The natural frequencies of an adhered cell model in the function of spread shapes.

As mentioned in the previous section, the measured elastic moduli of cells have values in a wide range. The natural frequency according to the elastic modulus when the area of a cell is 100×40 μm is shown in Figure 5.10. As the elastic modulus is increased, the natural frequency is increased.

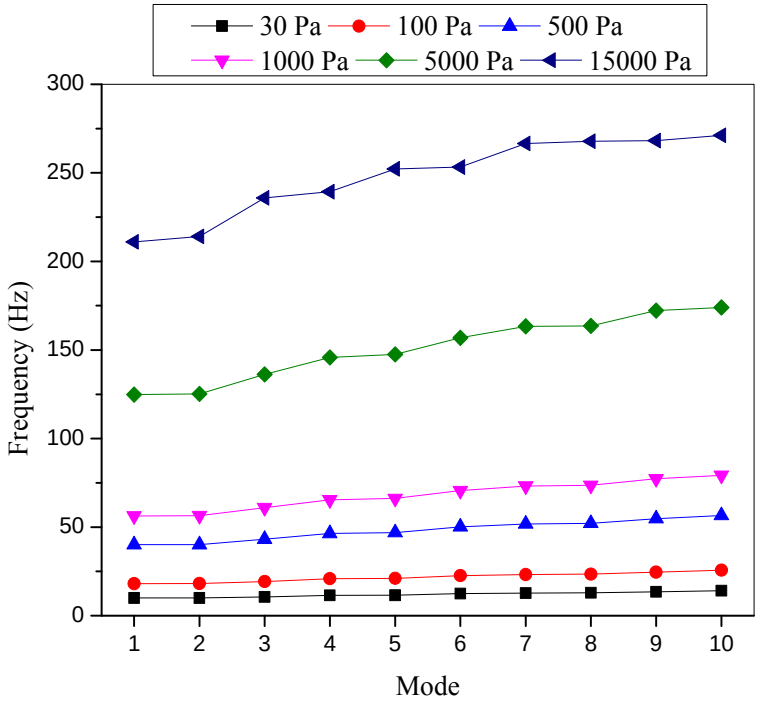

Figure 5.10 The natural frequencies of an adhered cell model in the function of the elastic modulus.

5.5 Discussion and conclusion

The dynamic characteristics of a bone cell in culturing conditions were analyzed using the finite element modal analysis. An ellipsoidal dome shape was utilized to model a bone cell adhered to a culture plate. Due to variations in the adherent cell shape, several ellipsoidal sizes were compared to evaluate the relationship between cell adherent shapes and the natural frequency. Several elastic moduli of cytoplasm were also tested since the mechanical property of cell components also has a large variation.

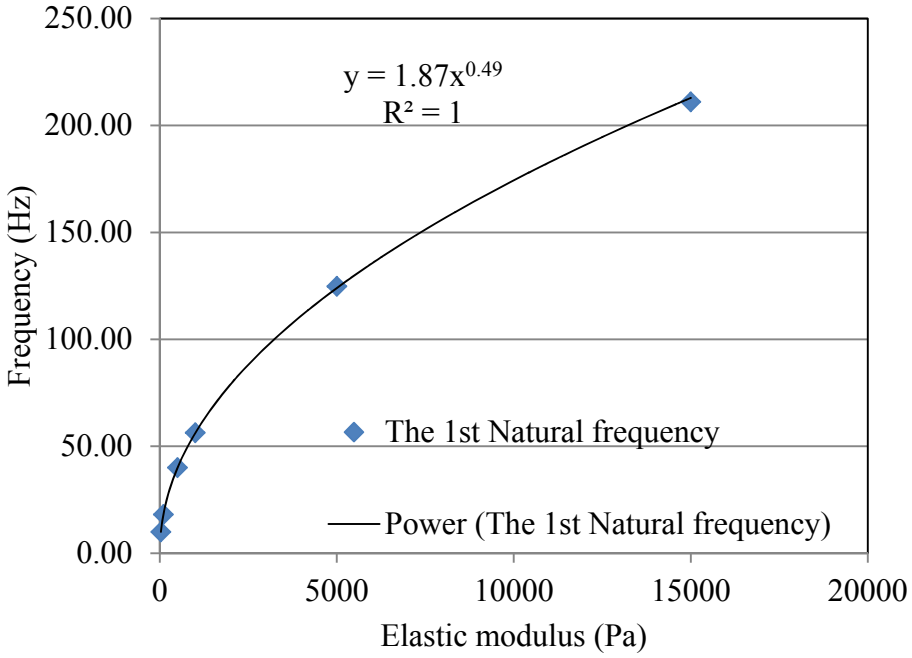

Figure 5.11 The calculated first natural frequency as the function of elastic modulus.

The result of this study showed that the natural frequency is in the range of 10-211 Hz. It does not depend on the cell shape, but it was affected by the Young's modulus. These results were compared to two studies that reported the natural frequency of a suspending single cell (Baker's yeast cell) [82, 83]. The result of this study shows a big difference with the natural frequency measured by Pelling *et al*. [82] 0.8-1.6 kHz and the calculated natural frequency by Molavi *et al*. [83] 137.7-525.7 kHz. This difference can be contributed to the different conditions and mechanical properties of studies. An adhered cell model has a different structure and vibration characteristics compared to the suspended cell. The elastic moduli in this study (30-15,000 Pa), based on other computational studies, is a very small value compared to the value (0.75 MPa) used in

other studies [82, 83]. Considering the fact that the natural frequency is proportional to the square root of the elastic modulus, the first natural frequencies extracted as the function of the elastic modulus were fitted with the power law, and the data fitted equation according to the elastic modulus was obtained (Figure 5.11). Consequently, the calculated first natural frequency of an adhered cell model with 0.75 MPa was 1.4 kHz. It demonstrates that the results of this study are close to the natural frequency measured by Pelling *et al*. [82].

The experimental studies measuring the effect of vibration amplitudes and frequencies have shown that several optimal values were beneficial for cell growth [70, 71]. Rosenberg *et al.* [69] found that the optimal vibration for osteoblast proliferation was at 20 Hz frequency with 0.5±0.1 m/s^2. Shikata *et al*. [70] showed that the vibration frequency at 50 Hz with 0.5 g caused 4.5 times higher ALP gene expression than that of the non-vibrating case. In those studies, the optimum frequency helping to stimulate and grow bone cells was around 20-60 Hz. Based on this study and two studies [69, 70], it is supposed that the frequency of applied vibration close to the natural frequency has to be beneficial for the growth of the bone cell.

CHAPTER 6

Conclusion and future work

Vibration transfer to whole body may have harmful or beneficial effects, depending on its magnitude, frequency and repetition rate. In order to understand the effect of whole body vibration, the foot and ankle system was investigated in the view of the starting point of whole body vibration. The study of an adherent cell on a culturing plate with the Finite Element modal analysis was carried out to provide some information about the relationship between vibration and bone growth.

The dynamic response and model of the foot and ankle system exposed to vertical vibration was demonstrated with vibration transmissibility measurement, black box system identification, and dynamic model development. Chapter 2 presented the experimental results of the vibration transmissibility and phase delay between input (Base) and output (Medial Malleolus and Tibial Tuberosity). The vibration absorbing capability of the foot and ankle system was measured as the function of applied mass and posture conditions of the system. The results are as follows:

- The transmission of the external vibration to whole body was closely related to the vibration absorbing capability of the foot and ankle since the major transmissibility happened at the foot and ankle.
- The transmissibility depended on the applied frequency and mass conditions. As the applied frequency was increased, the transmissibility was gradually decreased. The applied mass increased the stiffness of the foot and ankle and resulted in the increase of the resonant frequency from 20 to 30-40 Hz with the increase of the additional

mass. This means that the overweight or obese persons can get more vibration transmission to the whole body when they are exposed to higher frequency (30-40 Hz), the overweight and obesity can lead a potential injurious effect since the resonant frequency of overweight and obese persons is close to the major frequency range of heel strike during gait.

The system identification based on black box modes was utilized to understand the dynamic characteristics of the foot and ankle system in Chapter 3. The identification of black box model was selected as a convenient method to model the complicated foot and ankle system without considering prior information.

- Black box system identification provided the characteristics of the dynamic model and guided the development of the dynamic model in the future.
- The utilized linear polynomial models and state-space model showed good identification performance (60-98%). The identification error was observed in the nonlinear behavior of the measured acceleration.
- The estimation results also presented that the identification of the foot and ankle system with linear models had a limitation at the lower frequency (10-15 Hz) regardless of the applied mass condition because of the nonlinear behavior of output. Therefore, nonlinear black box system identification was suggested for better estimation performance. The results of black box system identification (state-space model) gave a guide (2-8 order state-space model) for the future development of the grey box model.

Chapter 4 demonstrated the development procedure of the dynamic model of the foot and ankle system to understand the vibration absorbing capability of the foot and

ankle with the estimated parameters. Previously, the concept of the truss structure was applied to represent the medial arch of the foot and ankle. In this study, a more realistic model of the medial arch was proposed and developed to represent the dynamic model of the foot and ankle system. It consisted of the five-rigid body including the tibia and viscoelastic parts. The forefoot in the medial arch was expressed with three-rigid body (three metatarsals, the cuneiforms, and the navicular). The hindfoot consisting of the talus and calcaneus was modeled a rigid body. The joints between rigid bodies were represented by the viscoelastic model. The viscoelastic model of the plantar aponeurosis, fat pad of foot, and talus joint were also included in the five-rigid body model. Lagrange's equation was utilized to derive the equations of motion for the model. The derived equation was linearized with Taylor series expansion since the motion at the operating point was very small. However, the linearized equations showed a problem related to the expensive computing cost. Through the parameter sensitivity analysis, the viscoelastic material of the fat pad and talocrural joint were defined as more sensitive parameters with respect to the states. Consequently, the derived equations were simplified as two degrees of freedom model including two viscoelastic parts (the fat pad and talocrural joint). Nonlinear behavior of the foot and ankle system shown in Chapter 3 was compensated by nonlinear damping properties. Unknown parameters of the dynamic model were estimated by the parameter estimation method (optimization algorithm) by fitting the experimental data. The estimated parameters demonstrated the following about the behavior of the foot and ankle system:

- The fat pad and talocrural joint possess the major vibration absorbing capability of the foot and ankle, the fat pad dissipated more energy than the talocrural joint.

- The applied mass and frequency increase affected the stiffness increase at the ankle joint and fat pad.
- The derived model could be utilized to estimate the viscoelastic material model at the talocrural joint and fat pad when the input and output vibration is measured at the given system.

As a micro scale study of whole body vibration, the dynamic characteristics of cells adhered to the culturing plate were investigated to understand the relationship between vibration and bone growth in Chapter 5. The Finite Element modal analysis was employed to extract the natural frequencies and mode shapes of an adhered cell. An ellipsoidal dome shape was modeled for an adhered bone cell to the culture plate. Four types of ellipsoidal sizes were considered to analyze the effect of the cell adhered shape since there are variations in the adherent shape of cells in reality. Based on the variation of mechanical properties from the literature survey, several elastic moduli of cytoplasm were applied to find the effect of the elastic modulus on the natural frequency. Through the Finite Element modal analysis, the natural frequencies and mode shapes were obtained and compared with other studies.

- The oscillating patterns of an adhered cell were described using the mode shapes.
- The results of the Finite Element modal analysis showed that the natural frequencies (18-25 Hz) were very similar to each other regardless of the adhered shape of cells.
- The variation of the elastic modulus affected the variation of the natural frequency (10-211 Hz).
- The comparison between the calculated natural frequency and the optimal vibration (20-60 Hz) for bone cell growth reported in other experimental studies showed that

the natural frequency was supposed to be closely related to the optimal vibration frequency for bone cell growth.

For future work, the frequency range will be increased to measure the transmissibility below 10 Hz input vibration. Various vibration amplitude and random vibration needs to be considered as an input for general vibration transmissibility of the foot and ankle system. The experiment of vibration transmission in standing condition will be considered to give better understanding of the effect of whole body vibration.

The nonlinear black box model system identification will be performed for the nonlinear behavior of the output acceleration and compared with the results of linear black box models. The derived model will be tested with other conditions, such as various frequencies, loading conditions, after obtaining the input and output vibration.

The tensegrity model including a cytoskleton structure will be utilized for the detail model of cells. A more realistic material model will be considered to express viscoelastic material properties of cells.

References

[1] Isman, R. E., Inman, V. T., and Poor, P., 1969, "Anthropometric studies of the human foot and ankle," Bulletin of prosthetics research, 11, pp. 97-108.

[2] O'Rahilly, Müller, Carpenter & Swenson, "Basic Human Anatomy", http://www.dartmouth.edu/~humananatomy/part_3/chapter_17.html

[3] http://xprojkt.blogspot.com/2010/10/foot-arches-reasoning-medicine-ii.html.

[4] "Whole body vibration," http://en.wikipedia.org/wiki/Whole_body_vibration.

[5] Rittweger, J., Beller, G., and Felsenberg, D., 2000, "Acute physiological effects of exhaustive whole-body vibration exercise in man," Clinical physiology, 20(2), pp. 134-142.

[6] Torvinen, S., Kannus, P., Sievänen, H., H JÄRVINEN, T. A., Pasanen, M., Kontulainen, S., N JÄRVINEN, T. L., Järvinen, M., Oja, P., and Vuori, I., 2002, "Effect of four-month vertical whole body vibration on performance and balance," Medicine & Science in Sports & Exercise, 34(9), p. 1523.

[7] Verschueren, S. M. P., Roelants, M., Delecluse, C., Swinnen, S., Vanderschueren, D., and Boonen, S., 2004, "Effect of 6 Month Whole Body Vibration Training on Hip Density, Muscle Strength, and Postural Control in Postmenopausal Women: A Randomized Controlled Pilot Study," Journal of bone and mineral research, 19(3), pp. 352-359.

[8] Ljung, L., 1999, System identification, Wiley Online Library.

[9] Ljung, L., and MathWorks, I., 2007, System Identification Toolbox 7: User's Guide, MathWorks, Incorporated.

[10] Folman, Y., Wosk, J., Voloshin, A., and Liberty, S., 1986, "Cyclic impacts on heel strike: a possible biomechanical factor in the etiology of degenerative disease of the human locomotor system," Archives of Orthopaedic and Trauma Surgery, 104(6), pp. 363-365.

[11] Holt, K. G., Wagenaar, R. C., Kubo, M., Lafiandra, M. E., and Obusek, J. P., 2005, "Modulation of Force Transmission to the Head While Carrying a Backpack Load at Different Walking Speeds," Journal of Biomechanics, 38(8), pp. 1621-1628.

[12] Radin, E. L., Burr, D. B., Caterson, B., Fyhrie, D., Brown, T. D., and Boyd, R. D., 1991, "Mechanical Determinants of Osteoarthrosis," Semin Arthritis Rheum, 21(3 Suppl 2), pp. 12-21.

[13] Radin, E. L., Martin, R. B., Burr, D. B., Caterson, B., Boyd, R. D., and Goodwin, C., 1984, "Effects of Mechanical Loading on the Tissues of the Rabbit Knee," J Orthop Res, 2(3), pp. 221-34.

[14] Radin, E. L., Swann, D. A., Paul, I. L., and Mcgrath, P. J., 1982, "Factors Influencing Articular Cartilage Wear in Vitro," Arthritis & Rheumatism, 25(8), pp. 974-980.

[15] Voloshin, A., and Wosk, J., 1982, "An in Vivo Study of Low Back Pain and Shock Absorption in the Human Locomotor System," Journal of Biomechanics, 15(1), pp. 21-27.

[16] Wosk, J., and Voloshin, A., 1981, "Wave Attenuation in Skeletons of Young Healthy Persons," Journal of Biomechanics, 14(4), pp. 261-263, 265-267.

[17] Panjabi, M. M., Andersson, G. B., Jorneus, L., Hult, E., and Mattsson, L., 1986, "In Vivo Measurements of Spinal Column Vibrations," J Bone Joint Surg Am, 68(5), pp. 695-702.

[18] Matsumoto, Y., and Griffin, M., 1998, "Movement of the Upper-Body of Seated Subjects Exposed to Vertical Whole-Body Vibration at the Principal Resonance Frequency," Journal of Sound and Vibration, 215(4), pp. 743-762.

[19] Matsumoto, Y., and Griffin, M., 1998, "Dynamic Response of the Standing Human Body Exposed to Vertical Vibration: Influence of Posture and Vibration Magnitude," Journal of Sound and Vibration, 212(1), pp. 85-107.

[20] Harazin, B., and Grzesik, J., 1998, "The Transmission of Vertical Whole-Body Vibration to the Body Segments of Standing Subjects," Journal of Sound and Vibration, 215(4), pp. 775-787.

[21] Paddan, G., and Griffin, M., 1998, "A Review of the Transmission of Translational Seat Vibration to the Head," Journal of Sound and Vibration, 215(4), pp. 863-882.

[22] Hinz, B., and Seidel, H., 1987, "The Nonlinearity of the Human Body's Dynamic Response During Sinusoidal Whole Body Vibration," Industrial health, 25(4), pp. 169.

[23] Mansfield, N., Holmlund, P., and Lundstrom, R., 2001, "Apparent Mass and Absorbed Power During Exposure to Whole-Body Vibration and Repeated Shocks," Journal of Sound and Vibration, 248(3), pp. 427-440.

[24] Aruin, A., and Zatsiorsky, V., 1984, "Biomechanical Characteristics of Human Ankle-Joint Muscles," European journal of applied physiology and occupational physiology, 52(4), pp. 400-406.

[25] Bawa, P., and Stein, R., 1976, "Frequency Response of Human Soleus Muscle," Journal of neurophysiology, 39(4), pp. 788-793.

[26] Wu, X., Rakheja, S., and Boileau, P. E., 1999, "Analyses of Relationships between Biodynamic Response Functions," Journal of Sound and Vibration, 226(3), pp. 595-606.

[27] Shin, K., and Hammond, J. K., 2008, Fundamentals of Signal Processing for Sound and Vibration Engineers, Wiley.

[28] Kiiski, J., Heinonen, A., Järvinen, T. L., Kannus, P., and Sievänen, H., 2008, "Transmission of Vertical Whole Body Vibration to the Human Body," Journal of Bone and Mineral Research, 23(8), pp. 1318-1325.

[29] Matsumoto, Y., and Griffin, M., 2000, "Comparison of Biodynamic Responses in Standing and Seated Human Bodies," Journal of Sound and Vibration, 238(4), pp. 691-704.

[30] Nokes, L. D. M., Williams, J. H., Fairclough, J. A., Mintowtczyz, W. J., and Mackie, I. G., 1984, "A Literature-Review of Vibrational Analysis of Human Limbs," Ieee Transactions on Biomedical Engineering, 31(2), pp. 187-192.

[31] Thorby, D., 2008, Structural Dynamics and Vibration in Practice: An Engineering Handbook, Butterworth-Heinemann.

[32] Winter, D. A., 2009, Biomechanics and Motor Control of Human Movement, John Wiley & Sons Inc.

[33] Wei, L., and Griffin, M., 1998, "Mathematical models for the apparent mass of the seated human body exposed to vertical vibration," Journal of Sound and Vibration, 212(5), pp. 855-874.

[34] Kim, W., Voloshin, A. S., and Johnson, S. H., 1994, "Modeling of heel strike transients during running," Human Movement Science, 13(2), pp. 221-244.

[35] Gefen, A., 2003, "The in vivo elastic properties of the plantar fascia during the contact phase of walking," Foot and Ankle International, 24(3), pp. 238-244.

[36] Simkin, A., and Leichter, I., 1990, "Role of the calcaneal inclination in the energy storage capacity of the human foot—a biomechanical model," Medical and Biological Engineering and Computing, 28(2), pp. 149-152.

[37] Kim, W., and Voloshin, A. S., 1995, "Role of plantar fascia in the load bearing capacity of the human foot," Journal of biomechanics, 28(9), pp. 1025-1033.

[38] Czop, P., and Wszołek, G., 2010, "Advanced model structures applied to system identification of a servo-hydraulic test rig," ISSUES, 1, p. 2.

[39] Yaacob, S., and Mohamed, F., 1998, "Black-box modelling of the induction motor," IEEE, pp. 883-886.

[40] Mohamed, F. A., and Koivo, H., 2004, "Modelling of induction motor using non-linear neural network system identification," IEEE, pp. 977-982 vol. 972.

[41] McMahon, T. A., 1987, "The spring in the human foot," Nature, 325, pp. 108-109.

[42] Ker, R. F., Bennett, M., Bibby, S., Kester, R., and Alexander, R. M. N., 1987, "The spring in the arch of the human foot."

[43] Salathé Jr, E. P., Arangio, G. A., and Salathé, E. P., 1986, "A biomechanical model of the foot," Journal of biomechanics, 19(12), pp. 989-1001.

[44] Salathe, E. P., and Arangio, G., 2002, "A biomechanical model of the foot: the role of muscles, tendons, and ligaments," Journal of biomechanical engineering, 124, p. 281.

[45] Masson, C., Thollon, L., Cesari, D., and Brunet, C., 2006, "Effects of static high compression on human foot-ankle: biomechanical response and injuries," Surgical and Radiologic Anatomy, 28(1), pp. 46-53.
[46] Wright, D., and Rennels, D., 1964, "A study of the elastic properties of plantar fascia," The Journal of Bone and Joint Surgery (American), 46(3), pp. 482-492.
[47] Lafortune, M. A., Henning, E., and Valiant, G. A., 1995, "Tibial shock measured with bone and skin mounted transducers," Journal of biomechanics, 28(8), pp. 989-993.
[48] Granata, K., Wilson, S., Massimini, A., and Gabriel, R., 2004, "Active stiffness of the ankle in response to inertial and elastic loads," Journal of Electromyography and Kinesiology, 14(5), pp. 599-609.
[49] Cheung, J. T. M., Zhang, M., Leung, A. K. L., and Fan, Y. B., 2005, "Three-dimensional finite element analysis of the foot during standing--a material sensitivity study," Journal of biomechanics, 38(5), pp. 1045-1054.
[50] Gefen, A., Megido-Ravid, M., Itzchak, Y., and Arcan, M., 2000, "Biomechanical analysis of the three-dimensional foot structure during gait: a basic tool for clinical applications," Journal of biomechanical engineering, 122, p. 630.
[51] Fard, M. A., Ishihara, T., and Inooka, H., 2003, "Dynamics of the head-neck complex in response to the trunk horizontal vibration: modeling and identification," Journal of biomechanical engineering, 125, p. 533.
[52] Actis, R. L., Ventura, L. B., Smith, K. E., Commean, P. K., Lott, D. J., Pilgram, T. K., and Mueller, M. J., 2006, "Numerical simulation of the plantar pressure distribution in the diabetic foot during the push-off stance," Medical and Biological Engineering and Computing, 44(8), pp. 653-663.
[53] eOrthopod, 2012, http://www.eorthopod.com/.
[54] Webber, C., and Kennett, T., 1976, "Bone density measured by photon scattering. I. A system for clinical use," Physics in medicine and biology, 21, p. 760.
[55] Hata, M., Nango, A., Niki, H., Hayafune, Y., and Kato, A., 1997, "Volume of tarsal bones in congenital clubfoot," Journal of orthopaedic science, 2(1), pp. 3-9.
[56] Kim, S., Cho, H., and Lee, C., 1987, "A parameter sensitivity analysis for the dynamic model of a variable displacement axial piston pump," ARCHIVE: Proceedings of the Institution of Mechanical Engineers, Part C: Mechanical Engineering Science 1983-1988 (vols 197-202), 201(43), pp. 235-243.
[57] Yue, H., Brown, M., Knowles, J., Wang, H., Broomhead, D. S., and Kell, D. B., 2006, "Insights into the behaviour of systems biology models from dynamic sensitivity and identifiability analysis: a case study of an NF-κB signalling pathway," Mol. BioSyst., 2(12), pp. 640-649.
[58] Attarian, A., 2009, "tssolve.m," http://www.gnu.org/licenses/gpl.html.
[59] Bennett, M., and Ker, R., 1990, "The mechanical properties of the human subcalcaneal fat pad in compression," Journal of anatomy, 171, p. 131.

[60] Ledoux, W. R., and Blevins, J. J., 2007, "The compressive material properties of the plantar soft tissue," Journal of biomechanics, 40(13), pp. 2975-2981.
[61] Scott, S. H., and Winter, D. A., 1993, "Biomechanical model of the human foot: kinematics and kinetics during the stance phase of walking," Journal of biomechanics, 26(9), p. 1091.
[62] Gefen, A., Megido-Ravid, M., and Itzchak, Y., 2001, "In vivo biomechanical behavior of the human heel pad during the stance phase of gait," Journal of biomechanics, 34(12), pp. 1661-1665.
[63] MathWorks, I., 2012, Matlab R2012a Optimization Toolbox User's Guide, The Math Works.
[64] Miller-Young, J. E., Duncan, N. A., and Baroud, G., 2002, "Material properties of the human calcaneal fat pad in compression: experiment and theory," Journal of biomechanics, 35(12), pp. 1523-1531.
[65] Pain, M. T. G., and Challis, J. H., 2001, "The role of the heel pad and shank soft tissue during impacts: a further resolution of a paradox," Journal of biomechanics, 34(3), pp. 327-333.
[66] Provenzano, P., Lakes, R., Corr, D., and Vanderby, R., 2002, "Application of nonlinear viscoelastic models to describe ligament behavior," Biomechanics and modeling in mechanobiology, 1(1), pp. 45-57.
[67] Brown, T. D., 2000, "Techniques for mechanical stimulation of cells in vitro: a review," Journal of biomechanics, 33(1), pp. 3-14.
[68] Hasegawa, S., Sato, S., Saito, S., Suzuki, Y., and Brunette, D., 1985, "Mechanical stretching increases the number of cultured bone cells synthesizing DNA and alters their pattern of protein synthesis," Calcified tissue international, 37(4), pp. 431-436.
[69] Rosenberg, N., Levy, M., and Francis, M., 2002, "Experimental model for stimulation of cultured human osteoblast-like cells by high frequency vibration," Cytotechnology, 39(3), pp. 125-130.
[70] Shikata, T., Shiraishi, T., Morishita, S., Takeuchi, R., and Saito, T., 2008, "Effects of Amplitude and Frequency of Mechanical Vibration Stimulation on Cultured Osteoblasts," Journal of System Design and Dynamics, 2(1), pp. 382-388.
[71] Tanaka, S. M., 1999, "A new mechanical stimulator for cultured bone cells using piezoelectric actuator," Journal of biomechanics, 32(4), pp. 427-430.
[72] McGarry, J., and Prendergast, P., 2004, "A three-dimensional finite element model of an adherent eukaryotic cell," Eur Cell Mater, 7, pp. 27-33.
[73] McGarry, J. G., Klein-Nulend, J., Mullender, M. G., and Prendergast, P. J., 2005, "A comparison of strain and fluid shear stress in stimulating bone cell responses—a computational and experimental study," The FASEB journal, 19(3), pp. 482-484.

[74] Abolfathi, N., Karami, G., and Ziejewski, M., 2008, "BIOMECHANICAL CELL MODELLING UNDER IMPACT LOADING," International Journal of Modelling and Simulation 2008, 28(5).
[75] Charras, G. T., and Horton, M. A., 2002, "Determination of cellular strains by combined atomic force microscopy and finite element modeling," Biophysical journal, 83(2), pp. 858-879.
[76] http://www.nanofunction.org/single-cell-mechanobiology.
[77] Charras, G. T., and Horton, M. A., 2002, "Single cell mechanotransduction and its modulation analyzed by atomic force microscope indentation," Biophysical journal, 82(6), pp. 2970-2981.
[78] Freitas, R. A., 1999, Nanomedicine, volume I: Basic capabilities, Landes Bioscience Georgetown, TX.
[79] ANSYS Element Reference, ANSYS Inc, 2009.
[80] ANSYS Theory Reference for the Mechanical APDL and Mechanical Applications, ANSYS Inc., 2009
[81] ANSYS Structural Analysis Guide, ANSYS Inc., 2009.
[82] Pelling, A. E., Sehati, S., Gralla, E. B., Valentine, J. S., and Gimzewski, J. K., 2004, "Local nanomechanical motion of the cell wall of Saccharomyces cerevisiae," Science, 305(5687), pp. 1147-1150.
[83] Zarandi, M. M., Bonakdar, A., and Stiharu, I., "Investigations on Natural Frequencies of Individual Spherical and Ellipsoidal Bakery Yeast Cells."

APPENDIX A

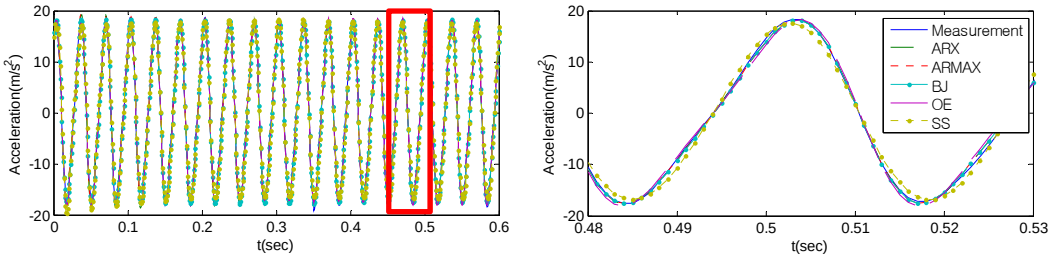

(a) 30 Hz & 0 kg: ARX(92%), ARMAX(94%), BJ(96%), OE(95%), SS(87%)

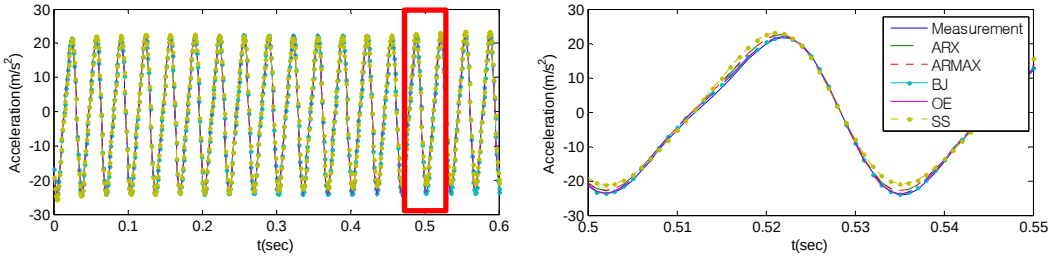

(b) 30 Hz & 2.3 kg: ARX(957%), ARMAX(95%), BJ(97%), OE(97%), SS(87%)

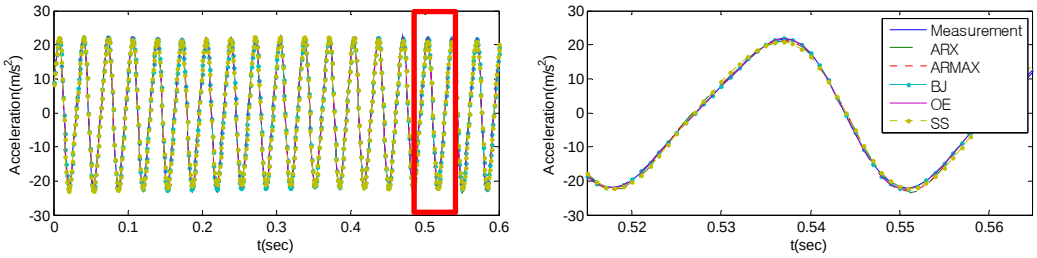

(c) 30 Hz & 4.5 kg: ARX(95%), ARMAX(96%), BJ(96%), OE(95%), SS(93%)

Figure A.1 An example of black box system identification results at 30 Hz (subject # 16)

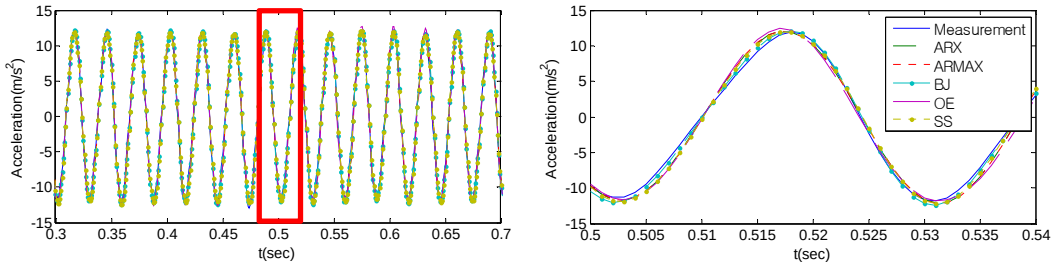

(a) 35 Hz & 0 kg: ARX(95%), ARMAX(96%), BJ(96%), OE(95%), SS(93%)

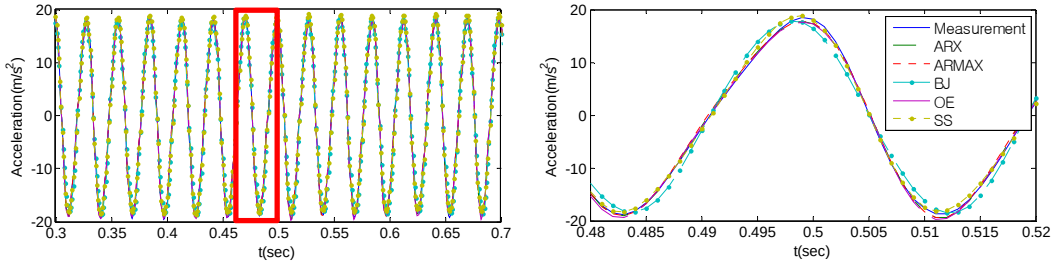

(b) 35 Hz & 2.3 kg: ARX(97%), ARMAX(97%), BJ(887%), OE(97%), SS(94%)

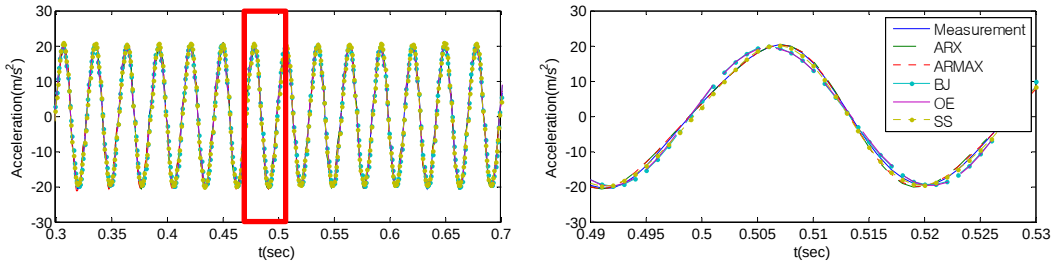

(c) 35 Hz & 4.5 kg: ARX(94%), ARMAX(90%), BJ(89%), OE(89%), SS(93%)

Figure A.2 An example of black box system identification results at 35 Hz (subject # 16)

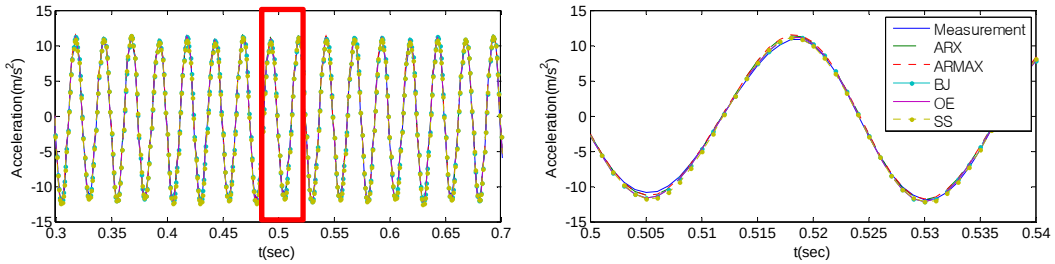

(a) 40 Hz & 0 kg: ARX(94%), ARMAX(94%), BJ(95%), OE(95%), SS(93%)

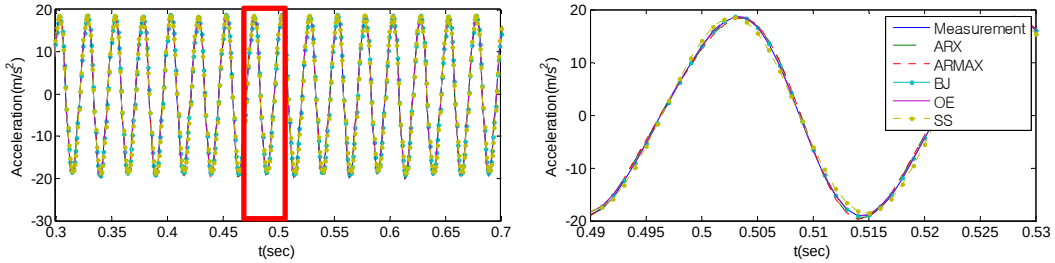

(b) 40 Hz & 2.3 kg: ARX(96%), ARMAX(95%), BJ(97%), OE(97%), SS(93%)

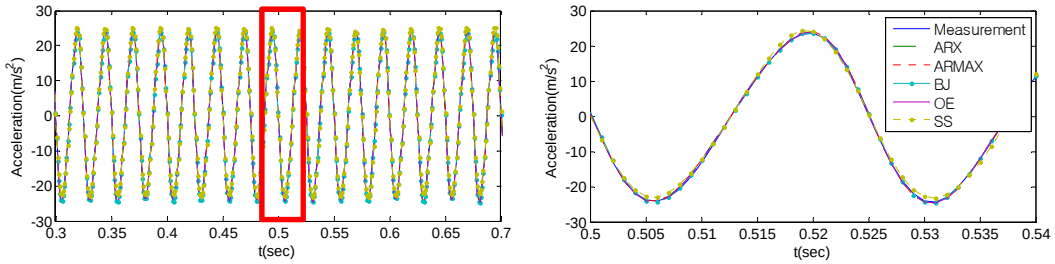

(c) 40 Hz & 4.5 kg: ARX(97%), ARMAX(97%), BJ(97%), OE(97%), SS(92%)

Figure A.3 An example of black box system identification results at 40 Hz (subject # 16)

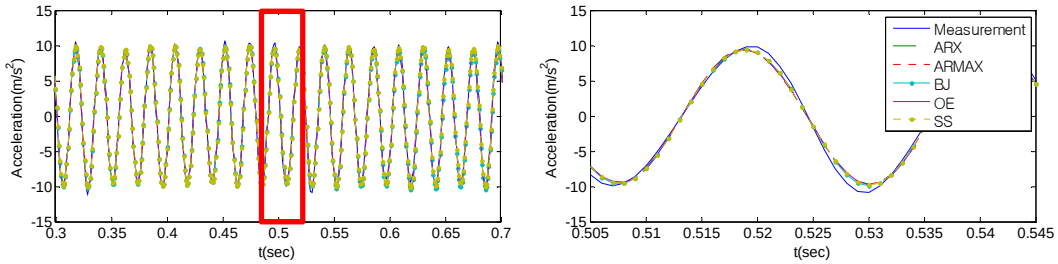

(a) 45 Hz & 0 kg: ARX(94%), ARMAX(94%), BJ(93%), OE(93%), SS(94%)

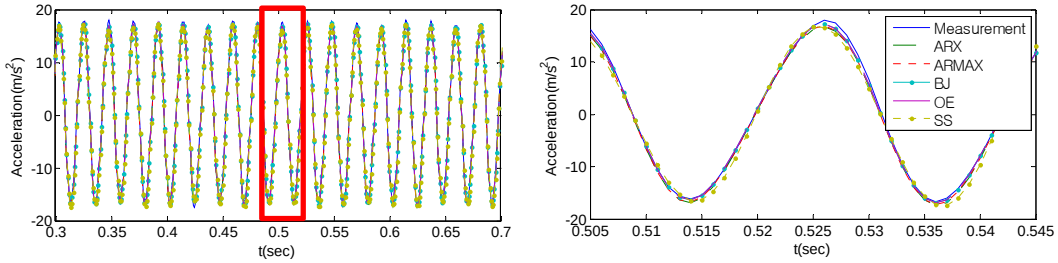

(b) 45 Hz & 2.3 kg: ARX(95%), ARMAX(95%), BJ(96%), OE(96%), SS(91%)

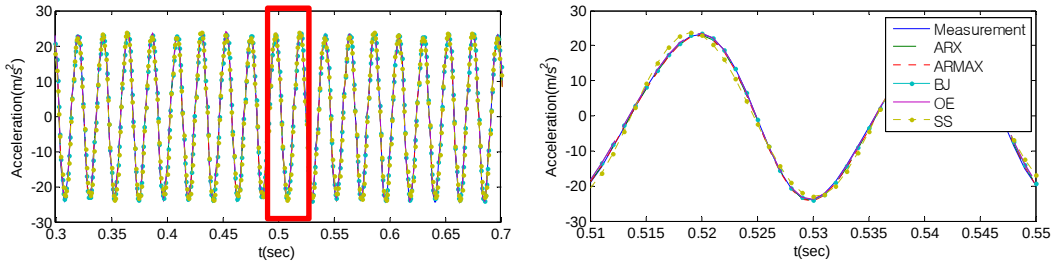

(c) 45 Hz & 4.5 kg: ARX(97%), ARMAX(98%), BJ(97%), OE(96%), SS(90%)

Figure A.4 An example of black box system identification results at 45 Hz (subject # 16)

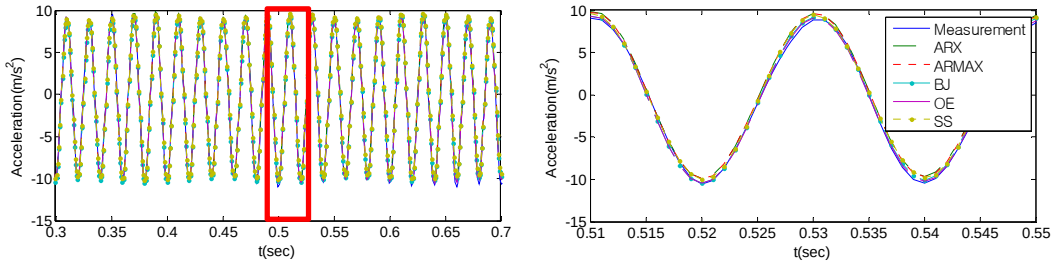

(a) 50 Hz & 0 kg: ARX(83%), ARMAX(83%), BJ(84%), OE(95%), SS(83%)

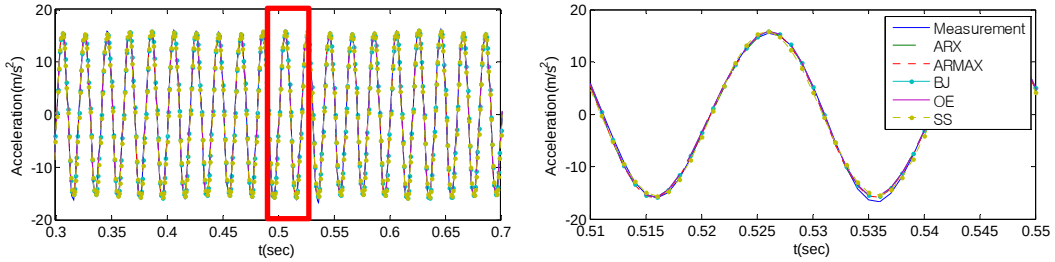

(b) 50 Hz & 2.3 kg: ARX(96%), ARMAX(96%), BJ(97%), OE(97%), SS(94%)

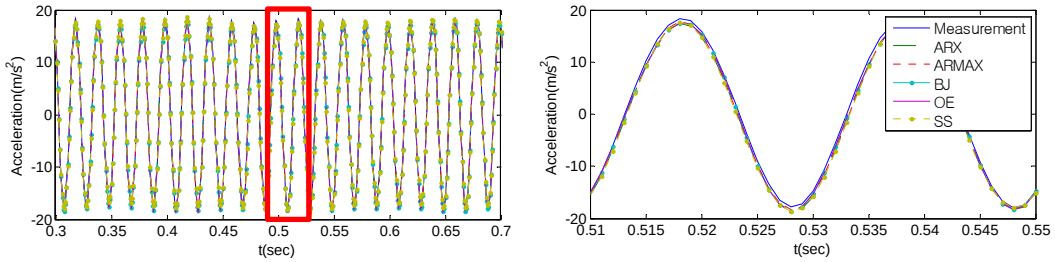

(c) 50 Hz & 4.5 kg: ARX(95%), ARMAX(95%), BJ(95%), OE(95%), SS(94%)

Figure A.5 An example of black box system identification results at 50 Hz (subject # 16)

Table A.1 Black box system identification results (Subject # 2).

Freq (Hz)	Mass (kg)	ARX		ARMAX		BJ		OE		SS	
		(na, nb, nk)	fit (%)	(na, nb, nc, nk)	fit (%)	(nb, nc, nd, nf, nk)	fit (%)	(nb, nf, nk)	fit (%)	(order)	fit (%)
10	0	(11,11,4)	62	(11,11,5,4)	60	(11,5,5,5,4)	55	(11,5,4)	78	6	60
	2.3	(12,11,3)	60	(12,11,5,3)	56	(11,5,5,5,3)	67	(11,5,3)	68	6	56
	4.5	(10,14,4)	51	(10,14,3,4)	45	(14,3,3,3,4)	38	(14,3,4)	67	8	50
15	0	(11,8,7)	69	(11,8,5,7)	66	(8,5,5,5,7)	76	(8,5,7)	88	8	72
	2.3	(9,8,2)	77	(9,8,5,2)	78	(8,5,5,5,2)	76	(8,5,2)	83	9	80
	4.5	(10,3,10)	45	(10,3,5,10)	68	(3,5,5,5,10)	80	(3,5,10)	80	9	79
20	0	(12,4,7)	80	(12,4,5,7)	82	(4,5,5,5,7)	81	(4,5,7)	86	10	84
	2.3	(10,4,9)	84	(10,4,5,9)	86	(4,5,5,5,9)	91	(4,5,9)	91	8	88
	4.5	(12,6,12)	86	(12,6,5,12)	85	(6,5,5,5,12)	89	(6,5,12)	89	6	78
25	0	(9,10,5)	96	(9,10,5,5)	93	(10,5,5,5,5)	65	(10,5,5)	96	10	96
	2.3	(12,4,2)	94	(12,4,3,2)	93	(4,3,3,3,2)	94	(4,3,2)	94	5	82
	4.5	(12,5,12)	92	(12,5,3,12)	93	(5,3,3,3,12)	94	(5,3,12)	94	7	94
30	0	(11,4,7)	93	(11,4,5,7)	93	(4,5,5,5,7)	94	(4,5,7)	95	7	95
	2.3	(11,5,12)	96	(11,5,5,12)	96	(5,5,5,5,12)	96	(5,5,12)	97	7	93
	4.5	(11,5,7)	95	(11,5,5,7)	95	(5,5,5,5,7)	97	(5,5,7)	98	7	89
35	0	(12,8,10)	95	(12,8,5,10)	96	(8,5,5,5,10)	97	(8,5,10)	97	5	93
	2.3	(9,3,9)	94	(9,3,5,9)	88	(3,5,5,5,9)	93	(3,5,9)	95	5	91
	4.5	(9,1,4)	94	(9,1,3,4)	91	(1,3,3,3,4)	85	(1,3,4)	86	5	95
40	0	(10,11,3)	97	(10,11,3,3)	97	(11,3,3,3,3)	96	(11,3,3)	97	5	94
	2.3	(9,12,7)	97	(9,12,3,7)	97	(12,3,3,3,7)	97	(12,3,7)	97	5	92
	4.5	(10,9,6)	96	(10,9,3,6)	96	(9,3,3,3,6)	95	(9,3,6)	96	5	93
45	0	(12,12,10)	96	(12,12,3,10)	96	(12,3,3,3,10)	96	(12,3,10)	96	6	95
	2.3	(12,4,9)	96	(12,4,3,9)	97	(4,3,3,3,9)	97	(4,3,9)	97	5	91
	4.5	(12,9,8)	98	(12,9,3,8)	98	(9,3,3,3,8)	98	(9,3,8)	98	5	93
50	0	(9,7,10)	91	(9,7,3,10)	91	(7,3,3,3,10)	89	(7,3,10)	96	3	89
	2.3	(9,12,5)	93	(9,12,3,5)	93	(12,3,3,3,5)	92	(12,3,5)	94	3	91
	4.5	(9,12,3)	98	(9,12,3,3)	98	(12,3,3,3,3)	97	(12,3,3)	97	3	88

Table A.2 Black box system identification results (Subject # 3).

Freq (Hz)	Mass (kg)	ARX		ARMAX		BJ		OE		SS	
		(na, nb, nk)	fit (%)	(na, nb, nc, nk)	fit (%)	(nb, nc, nd, nf, nk)	fit (%)	(nb, nf, nk)	fit (%)	(order)	fit (%)
10	0	(13,11,9)	70	(13,11,5,9)	55	(11,5,5,5,9)	72	(11,5,9)	76	7	62
	2.3	(13,13,10)	64	(13,13,5,10)	52	(13,5,5,5,10)	72	(13,5,10)	68	8	64
	4.5	(11,4,7)	61	(11,4,3,7)	62	(4,3,3,3,7)	58	(4,3,7)	62	8	83
15	0	(13,5,3)	81	(13,5,3,3)	78	(5,3,3,3,3)	86	(5,3,3)	87	5	85
	2.3	(9,8,7)	81	(9,8,3,7)	83	(8,3,3,3,7)	86	(8,3,7)	87	7	85
	4.5	(15,1,10)	73	(15,1,3,10)	74	(1,3,3,3,10)	65	(1,3,10)	75	7	83
20	0	(9,10,14)	93	(9,10,3,14)	92	(10,3,3,3,14)	93	(10,3,14)	92	5	81
	2.3	(12,3,7)	87	(12,3,3,7)	87	(3,3,3,3,7)	83	(3,3,7)	85	8	89
	4.5	(12,12,1)	88	(12,12,3,1)	88	(12,3,3,3,1)	89	(12,3,1)	89	7	87
25	0	(9,7,5)	95	(9,7,5,5)	93	(7,5,5,5,5)	94	(7,5,5)	94	5	87
	2.3	(12,6,7)	80	(12,6,5,7)	79	(6,5,5,5,7)	86	(6,5,7)	88	7	73
	4.5	(12,10,3)	88	(12,10,5,3)	84	(10,5,5,5,3)	73	(10,5,3)	92	4	82
30	0	(11,5,3)	87	(11,5,3,3)	88	(5,3,3,3,3)	77	(5,3,3)	95	5	69
	2.3	(11,10,9)	91	(11,10,5,9)	91	(10,5,5,5,9)	92	(10,5,9)	89	6	89
	4.5	(12,4,8)	94	(12,4,3,8)	94	(4,3,3,3,8)	85	(4,3,8)	84	4	88
35	0	(9,3,3)	90	(9,3,3,3)	89	(3,3,3,3,3)	93	(3,3,3)	92	4	88
	2.3	(12,3,2)	93	(12,3,3,2)	88	(3,3,3,3,2)	93	(3,3,2)	90	4	87
	4.5	(12,3,13)	91	(12,3,3,13)	92	(3,3,3,3,13)	93	(3,3,13)	93	4	91
40	0	(10,9,11)	93	(10,9,3,11)	93	(9,3,3,3,11)	93	(9,3,11)	94	5	91
	2.3	(10,8,6)	96	(10,8,3,6)	96	(8,3,3,3,6)	71	(8,3,6)	97	5	93
	4.5	(10,12,14)	96	(10,12,3,14)	96	(12,3,3,3,14)	96	(12,3,14)	96	5	94
45	0	(13,10,12)	95	(13,10,3,12)	95	(10,3,3,3,12)	96	(10,3,12)	95	6	94
	2.3	(11,3,2)	92	(11,3,3,2)	95	(3,3,3,3,2)	96	(3,3,2)	96	5	93
	4.5	(10,7,7)	95	(10,7,3,7)	95	(7,3,3,3,7)	95	(7,3,7)	95	5	83
50	0	(10,5,3)	93	(10,5,3,3)	93	(5,3,3,3,3)	94	(5,3,3)	96	4	88
	2.3	(15,10,3)	97	(15,10,3,3)	97	(10,3,3,3,3)	92	(10,3,3)	96	4	91
	4.5	(14,10,3)	98	(14,10,3,3)	97	(10,3,3,3,3)	91	(10,3,3)	98	4	93

Table A.3 Black box system identification results (Subject # 4).

Freq	Mass	ARX		ARMAX		BJ		OE		SS	
(Hz)	(kg)	(na, nb, nk)	fit (%)	(na, nb, nc, nk)	fit (%)	(nb, nc, nd, nf, nk)	fit (%)	(nb, nf, nk)	fit (%)	(order)	fit (%)
10	0	(11,4,4)	71	(11,4,5,4)	78	(4,5,5,5,4)	79	(4,5,4)	80	8	81
	2.3	(14,10,2)	78	(14,10,5,2)	78	(10,5,5,5,2)	77	(10,5,2)	80	5	77
	4.5	(12,3,4)	65	(12,3,3,4)	63	(3,3,3,3,4)	65	(3,3,4)	68	6	74
15	0	(9,7,6)	85	(9,7,3,6)	91	(7,3,3,3,6)	93	(7,3,6)	92	5	91
	2.3	(9,4,6)	74	(9,4,3,6)	91	(4,3,3,3,6)	91	(4,3,6)	91	4	88
	4.5	(9,2,10)	60	(9,2,3,10)	52	(2,3,3,3,10)	73	(2,3,10)	83	5	90
20	0	(14,5,10)	83	(14,5,3,10)	84	(5,3,3,3,10)	85	(5,3,10)	89	4	85
	2.3	(12,5,12)	87	(12,5,3,12)	88	(5,3,3,3,12)	88	(5,3,12)	89	5	85
	4.5	(15,6,12)	89	(15,6,3,12)	90	(6,3,3,3,12)	90	(6,3,12)	89	5	87
25	0	(12,12,11)	84	(12,12,5,11)	85	(12,5,5,5,11)	85	(12,5,11)	85	4	78
	2.3	(12,12,3)	94	(12,12,5,3)	93	(12,5,5,5,3)	88	(12,5,3)	95	5	86
	4.5	(12,10,9)	89	(12,10,3,9)	89	(10,3,3,3,9)	88	(10,3,9)	94	5	85
30	0	(11,4,3)	89	(11,4,3,3)	88	(4,3,3,3,3)	89	(4,3,3)	91	4	88
	2.3	(11,7,5)	94	(11,7,3,5)	94	(7,3,3,3,5)	90	(7,3,5)	92	3	89
	4.5	(12,10,8)	94	(12,10,3,8)	94	(10,3,3,3,8)	92	(10,3,8)	95	5	91
35	0	(15,12,12)	90	(15,12,3,12)	91	(12,3,3,3,12)	89	(12,3,12)	91	3	85
	2.3	(9,7,9)	95	(9,7,3,9)	94	(7,3,3,3,9)	94	(7,3,9)	95	3	93
	4.5	(9,10,8)	95	(9,10,3,8)	95	(10,3,3,3,8)	95	(10,3,8)	97	3	93
40	0	(11,4,4)	77	(11,4,5,4)	89	(4,5,5,5,4)	76	(4,5,4)	86	7	88
	2.3	(10,8,4)	90	(10,8,3,4)	90	(8,3,3,3,4)	93	(8,3,4)	93	7	92
	4.5	(9,9,2)	96	(9,9,3,2)	96	(9,3,3,3,2)	95	(9,3,2)	96	8	96
45	0	(11,3,2)	77	(11,3,3,2)	76	(3,3,3,3,2)	70	(3,3,2)	89	3	85
	2.3	(10,6,2)	93	(10,6,3,2)	93	(6,3,3,3,2)	93	(6,3,2)	93	3	92
	4.5	(10,9,12)	96	(10,9,3,12)	96	(9,3,3,3,12)	96	(9,3,12)	97	5	96
50	0	(10,8,12)	90	(10,8,3,12)	90	(8,3,3,3,12)	91	(8,3,12)	91	5	90
	2.3	(10,6,4)	92	(10,6,3,4)	92	(6,3,3,3,4)	91	(6,3,4)	93	5	93
	4.5	(10,6,4)	93	(10,6,3,4)	94	(6,3,3,3,4)	96	(6,3,4)	97	5	95

Table A.4 Black box system identification results (Subject # 5).

Freq	Mass	ARX		ARMAX		BJ		OE		SS	
(Hz)	(kg)	(na, nb, nk)	fit (%)	(na, nb, nc, nk)	fit (%)	(nb, nc, nd, nf, nk)	fit (%)	(nb, nf, nk)	fit (%)	(order)	fit (%)
10	0	(13,4,6)	68	(13,4,5,6)	69	(4,5,5,5,6)	75	(4,5,6)	75	6	60
	2.3	(11,7,2)	67	(11,7,5,2)	68	(7,5,5,5,2)	73	(7,5,2)	76	6	64
	4.5	(9,4,10)	62	(9,4,5,10)	65	(4,5,5,5,10)	76	(4,5,10)	75	6	53
15	0	(13,8,5)	74	(13,8,5,5)	88	(8,5,5,5,5)	80	(8,5,5)	88	7	80
	2.3	(13,3,5)	83	(13,3,5,5)	79	(3,5,5,5,5)	88	(3,5,5)	88	7	90
	4.5	(13,4,6)	83	(13,4,5,6)	86	(4,5,5,5,6)	87	(4,5,6)	85	5	76
20	0	(11,9,8)	86	(11,9,3,8)	86	(9,3,3,3,8)	90	(9,3,8)	89	7	90
	2.3	(15,14,10)	91	(15,14,5,10)	91	(14,5,5,5,10)	94	(14,5,10)	94	7	90
	4.5	(9,12,10)	82	(9,12,3,10)	84	(12,3,3,3,10)	89	(12,3,10)	89	7	86
25	0	(12,4,7)	90	(12,4,3,7)	90	(4,3,3,3,7)	93	(4,3,7)	93	4	90
	2.3	(12,3,4)	91	(12,3,3,4)	91	(3,3,3,3,4)	91	(3,3,4)	91	4	84
	4.5	(12,10,10)	91	(12,10,3,10)	88	(10,3,3,3,10)	92	(10,3,10)	92	7	89
30	0	(14,3,4)	91	(14,3,5,4)	94	(3,5,5,5,4)	80	(3,5,4)	92	8	91
	2.3	(10,5,7)	92	(10,5,3,7)	91	(5,3,3,3,7)	91	(5,3,7)	91	8	93
	4.5	(12,9,2)	95	(12,9,5,2)	95	(9,5,5,5,2)	94	(9,5,2)	95	8	93
35	0	(12,10,5)	92	(12,10,5,5)	90	(10,5,5,5,5)	88	(10,5,5)	96	5	91
	2.3	(12,7,8)	96	(12,7,5,8)	95	(7,5,5,5,8)	96	(7,5,8)	95	5	90
	4.5	(12,7,10)	93	(12,7,5,10)	95	(7,5,5,5,10)	95	(7,5,10)	95	5	87
40	0	(10,8,9)	94	(10,8,5,9)	94	(8,5,5,5,9)	95	(8,5,9)	96	3	91
	2.3	(10,6,2)	94	(10,6,5,2)	95	(6,5,5,5,2)	95	(6,5,2)	95	5	89
	4.5	(11,10,2)	96	(11,10,5,2)	95	(10,5,5,5,2)	94	(10,5,2)	94	5	91
45	0	(10,4,4)	92	(10,4,5,4)	93	(4,5,5,5,4)	94	(4,5,4)	95	3	91
	2.3	(10,6,2)	96	(10,6,5,2)	96	(6,5,5,5,2)	96	(6,5,2)	97	3	93
	4.5	(10,9,10)	93	(10,9,5,10)	93	(9,5,5,5,10)	96	(9,5,10)	96	5	92
50	0	(10,5,11)	93	(10,5,5,11)	93	(5,5,5,5,11)	95	(5,5,11)	96	4	93
	2.3	(12,7,8)	95	(12,7,5,8)	95	(7,5,5,5,8)	97	(7,5,8)	97	4	94
	4.5	(12,3,4)	95	(12,3,5,4)	95	(3,5,5,5,4)	95	(3,5,4)	95	4	90

Table A.5 Black box system identification results (Subject # 6).

Freq (Hz)	Mass (kg)	ARX		ARMAX		BJ		OE		SS	
		(na, nb, nk)	fit (%)	(na, nb, nc, nk)	fit (%)	(nb, nc, nd, nf, nk)	fit (%)	(nb, nf, nk)	fit (%)	(order)	fit (%)
10	0	(15,8,7)	84	(15,8,5,7)	84	(8,5,5,5,7)	84	(8,5,7)	86	6	84
	2.3	(14,9,7)	70	(14,9,5,7)	69	(9,5,5,5,7)	59	(9,5,7)	78	8	69
	4.5	(14,7,12)	61	(14,7,5,12)	82	(7,5,5,5,12)	47	(7,5,12)	83	6	54
15	0	(9,11,8)	56	(9,11,5,8)	72	(11,5,5,5,8)	75	(11,5,8)	85	5	74
	2.3	(9,8,11)	83	(9,8,5,11)	82	(8,5,5,5,11)	83	(8,5,11)	84	5	79
	4.5	(12,2,15)	55	(12,2,5,15)	74	(2,5,5,5,15)	68	(2,5,15)	84	5	65
20	0	(12,4,14)	76	(12,4,3,14)	76	(4,3,3,3,14)	77	(4,3,14)	77	7	74
	2.3	(11,4,5)	75	(11,4,3,5)	70	(4,3,3,3,5)	78	(4,3,5)	80	7	79
	4.5	(12,13,10)	71	(12,13,3,10)	74	(13,3,3,3,10)	76	(13,3,10)	87	7	64
25	0	(12,6,11)	82	(12,6,3,11)	80	(6,3,3,3,11)	73	(6,3,11)	87	7	78
	2.3	(12,15,8)	88	(12,15,3,8)	88	(15,3,3,3,8)	86	(15,3,8)	88	7	83
	4.5	(12,5,4)	82	(12,5,3,4)	71	(5,3,3,3,4)	87	(5,3,4)	87	5	74
30	0	(11,4,9)	74	(11,4,3,9)	74	(4,3,3,3,9)	75	(4,3,9)	74	5	74
	2.3	(10,5,6)	79	(10,5,5,6)	82	(5,5,5,5,6)	83	(5,5,6)	87	8	84
	4.5	(10,7,13)	94	(10,7,5,13)	90	(7,5,5,5,13)	95	(7,5,13)	96	8	88
35	0	(15,3,4)	79	(15,3,5,4)	79	(3,5,5,5,4)	87	(3,5,4)	85	5	76
	2.3	(12,1,4)	92	(12,1,3,4)	89	(1,3,3,3,4)	86	(1,3,4)	86	5	89
	4.5	(9,8,8)	94	(9,8,5,8)	94	(8,5,5,5,8)	90	(8,5,8)	93	5	90
40	0	(11,6,3)	91	(11,6,3,3)	89	(6,3,3,3,3)	91	(6,3,3)	88	5	83
	2.3	(10,9,10)	92	(10,9,3,10)	92	(9,3,3,3,10)	93	(9,3,10)	92	5	93
	4.5	(12,6,6)	88	(12,6,5,6)	88	(6,5,5,5,6)	88	(6,5,6)	89	5	87
45	0	(11,9,8)	87	(11,9,3,8)	87	(9,3,3,3,8)	87	(9,3,8)	86	5	88
	2.3	(10,11,11)	93	(10,11,3,11)	93	(11,3,3,3,11)	94	(11,3,11)	94	3	92
	4.5	(12,9,4)	94	(12,9,3,4)	94	(9,3,3,3,4)	91	(9,3,4)	94	3	91
50	0	(11,6,3)	86	(11,6,3,3)	87	(6,3,3,3,3)	92	(6,3,3)	93	3	91
	2.3	(10,4,1)	95	(10,4,3,1)	95	(4,3,3,3,1)	95	(4,3,1)	94	3	94
	4.5	(10,12,8)	92	(10,12,3,8)	95	(12,3,3,3,8)	93	(12,3,8)	93	2	90

Table A.6 Black box system identification results (Subject # 7).

Freq	Mass	ARX		ARMAX		BJ		OE		SS	
(Hz)	(kg)	(na, nb, nk)	fit (%)	(na, nb, nc, nk)	fit (%)	(nb, nc, nd, nf, nk)	fit (%)	(nb, nf, nk)	fit (%)	(order)	fit (%)
10	0	(11,12,1)	88	(11,12,5,1)	89	(12,5,5,5,1)	91	(12,5,1)	91	6	89
	2.3	(13,12,4)	82	(13,12,5,4)	82	(12,5,5,5,4)	83	(12,5,4)	82	7	81
	4.5	(11,3,10)	73	(11,3,5,10)	75	(3,5,5,5,10)	74	(3,5,10)	74	6	71
15	0	(9,8,6)	87	(9,8,5,6)	86	(8,5,5,5,6)	91	(8,5,6)	92	5	88
	2.3	(11,7,5)	81	(11,7,5,5)	83	(7,5,5,5,5)	86	(7,5,5)	86	5	83
	4.5	(11,12,9)	86	(11,12,5,9)	85	(12,5,5,5,9)	87	(12,5,9)	90	5	85
20	0	(12,5,9)	94	(12,5,3,9)	94	(5,3,3,3,9)	95	(5,3,9)	95	5	92
	2.3	(9,6,10)	88	(9,6,3,10)	88	(6,3,3,3,10)	90	(6,3,10)	93	8	90
	4.5	(9,4,12)	90	(9,4,3,12)	89	(4,3,3,3,12)	91	(4,3,12)	92	6	89
25	0	(12,9,2)	95	(12,9,3,2)	94	(9,3,3,3,2)	96	(9,3,2)	96	6	91
	2.3	(12,9,6)	93	(12,9,3,6)	90	(9,3,3,3,6)	94	(9,3,6)	95	4	81
	4.5	(12,10,2)	90	(12,10,5,2)	90	(10,5,5,5,2)	92	(10,5,2)	94	4	80
30	0	(12,1,3)	83	(12,1,5,3)	90	(1,5,5,5,3)	96	(1,5,3)	96	5	94
	2.3	(9,10,5)	93	(9,10,5,5)	92	(10,5,5,5,5)	96	(10,5,5)	96	3	84
	4.5	(12,7,8)	95	(12,7,5,8)	95	(7,5,5,5,8)	94	(7,5,8)	94	3	86
35	0	(9,7,6)	95	(9,7,5,6)	94	(7,5,5,5,6)	95	(7,5,6)	95	3	91
	2.3	(12,9,12)	93	(12,9,5,12)	94	(9,5,5,5,12)	91	(9,5,12)	93	3	91
	4.5	(9,5,7)	94	(9,5,5,7)	95	(5,5,5,5,7)	95	(5,5,7)	95	3	90
40	0	(10,8,3)	96	(10,8,5,3)	96	(8,5,5,5,3)	96	(8,5,3)	96	3	93
	2.3	(10,5,6)	96	(10,5,5,6)	96	(5,5,5,5,6)	96	(5,5,6)	96	3	92
	4.5	(10,7,3)	95	(10,7,5,3)	96	(7,5,5,5,3)	97	(7,5,3)	97	3	92
45	0	(10,12,11)	94	(10,12,5,11)	94	(12,5,5,5,11)	96	(12,5,11)	96	3	94
	2.3	(10,8,1)	95	(10,8,5,1)	95	(8,5,5,5,1)	96	(8,5,1)	95	3	94
	4.5	(12,11,9)	96	(12,11,5,9)	96	(11,5,5,5,9)	95	(11,5,9)	95	3	95
50	0	(10,1,3)	95	(10,1,5,3)	95	(1,5,5,5,3)	95	(1,5,3)	95	3	94
	2.3	(11,4,9)	95	(11,4,5,9)	95	(4,5,5,5,9)	96	(4,5,9)	96	3	94
	4.5	(11,1,10)	95	(11,1,5,10)	95	(1,5,5,5,10)	95	(1,5,10)	95	3	93

Table A.7 Black box system identification results (Subject # 8).

Freq (Hz)	Mass (kg)	ARX		ARMAX		BJ		OE		SS	
		(na, nb, nk)	fit (%)	(na, nb, nc, nk)	fit (%)	(nb, nc, nd, nf, nk)	fit (%)	(nb, nf, nk)	fit (%)	(order)	fit (%)
10	0	(11,7,7)	72	(11,7,5,7)	71	(7,5,5,5,7)	65	(7,5,7)	75	5	71
	2.3	(9,6,6)	67	(9,6,5,6)	67	(6,5,5,5,6)	69	(6,5,6)	70	7	66
	4.5	(9,2,1)	54	(9,2,3,1)	55	(2,3,3,3,1)	74	(2,3,1)	73	6	53
15	0	(11,4,8)	92	(11,4,3,8)	91	(4,3,3,3,8)	93	(4,3,8)	93	5	92
	2.3	(9,1,6)	81	(9,1,3,6)	79	(1,3,3,3,6)	67	(1,3,6)	77	5	89
	4.5	(11,4,4)	89	(11,4,3,4)	90	(4,3,3,3,4)	88	(4,3,4)	87	5	87
20	0	(12,1,1)	93	(12,1,5,1)	93	(1,5,5,5,1)	80	(1,5,1)	85	5	92
	2.3	(12,4,3)	95	(12,4,3,3)	95	(4,3,3,3,3)	95	(4,3,3)	96	5	94
	4.5	(9,9,7)	94	(9,9,3,7)	92	(9,3,3,3,7)	93	(9,3,7)	91	7	93
25	0	(9,9,9)	92	(9,9,3,9)	93	(9,3,3,3,9)	94	(9,3,9)	95	4	94
	2.3	(9,9,10)	89	(9,9,3,10)	93	(9,3,3,3,10)	93	(9,3,10)	92	4	93
	4.5	(12,7,7)	91	(12,7,3,7)	90	(7,3,3,3,7)	95	(7,3,7)	94	4	91
30	0	(9,3,4)	94	(9,3,3,4)	94	(3,3,3,3,4)	86	(3,3,4)	94	3	88
	2.3	(11,11,4)	96	(11,11,3,4)	96	(11,3,3,3,4)	96	(11,3,4)	97	3	92
	4.5	(11,4,4)	95	(11,4,3,4)	95	(4,3,3,3,4)	91	(4,3,4)	97	4	95
35	0	(12,2,12)	93	(12,2,3,12)	94	(2,3,3,3,12)	94	(2,3,12)	94	4	94
	2.3	(9,5,9)	91	(9,5,3,9)	96	(5,3,3,3,9)	96	(5,3,9)	94	4	95
	4.5	(12,4,6)	95	(12,4,5,6)	95	(4,5,5,5,6)	95	(4,5,6)	93	2	95
40	0	(11,8,10)	91	(11,8,5,10)	92	(8,5,5,5,10)	95	(8,5,10)	95	4	88
	2.3	(10,5,2)	94	(10,5,5,2)	94	(5,5,5,5,2)	95	(5,5,2)	96	4	94
	4.5	(11,6,12)	93	(11,6,5,12)	96	(6,5,5,5,12)	95	(6,5,12)	96	2	92
45	0	(11,5,3)	91	(11,5,5,3)	92	(5,5,5,5,3)	91	(5,5,3)	91	4	91
	2.3	(10,12,5)	93	(10,12,5,5)	93	(12,5,5,5,5)	95	(12,5,5)	92	4	92
	4.5	(13,8,5)	93	(13,8,5,5)	94	(8,5,5,5,5)	94	(8,5,5)	94	2	92
50	0	(11,9,5)	93	(11,9,5,5)	93	(9,5,5,5,5)	94	(9,5,5)	94	2	92
	2.3	(10,8,12)	92	(10,8,3,12)	90	(8,3,3,3,12)	92	(8,3,12)	89	2	91
	4.5	(10,6,4)	92	(10,6,3,4)	92	(6,3,3,3,4)	93	(6,3,4)	95	3	91

Table A.8 Black box system identification results (Subject # 9).

Freq (Hz)	Mass (kg)	ARX		ARMAX		BJ		OE		SS	
		(na, nb, nk)	fit (%)	(na, nb, nc, nk)	fit (%)	(nb, nc, nd, nf, nk)	fit (%)	(nb, nf, nk)	fit (%)	(order)	fit (%)
10	0	(8,7,7)	89	(8,7,5,7)	90	(7,5,5,5,7)	89	(7,5,7)	90	6	88
	2.3	(15,4,11)	64	(15,4,5,11)	76	(4,5,5,5,11)	82	(4,5,11)	86	8	81
	4.5	(8,8,10)	80	(8,8,5,10)	75	(8,5,5,5,10)	66	(8,5,10)	87	8	74
15	0	(10,8,6)	92	(10,8,3,6)	92	(8,3,3,3,6)	90	(8,3,6)	92	8	89
	2.3	(9,8,2)	86	(9,8,3,2)	88	(8,3,3,3,2)	90	(8,3,2)	90	5	88
	4.5	(9,3,9)	81	(9,3,3,9)	80	(3,3,3,3,9)	86	(3,3,9)	88	5	84
20	0	(9,9,10)	93	(9,9,3,10)	95	(9,3,3,3,10)	95	(9,3,10)	93	6	86
	2.3	(12,2,5)	86	(12,2,3,5)	85	(2,3,3,3,5)	86	(2,3,5)	81	3	85
	4.5	(9,10,8)	94	(9,10,3,8)	95	(10,3,3,3,8)	94	(10,3,8)	95	3	88
25	0	(9,4,6)	91	(9,4,3,6)	93	(4,3,3,3,6)	96	(4,3,6)	96	4	91
	2.3	(9,4,12)	93	(9,4,3,12)	93	(4,3,3,3,12)	92	(4,3,12)	93	3	85
	4.5	(9,9,8)	96	(9,9,3,8)	90	(9,3,3,3,8)	93	(9,3,8)	95	2	84
30	0	(9,10,8)	95	(9,10,3,8)	96	(10,3,3,3,8)	95	(10,3,8)	97	4	89
	2.3	(11,5,8)	94	(11,5,3,8)	95	(5,3,3,3,8)	95	(5,3,8)	95	4	92
	4.5	(12,7,7)	94	(12,7,3,7)	94	(7,3,3,3,7)	94	(7,3,7)	94	4	90
35	0	(9,8,9)	96	(9,8,3,9)	96	(8,3,3,3,9)	97	(8,3,9)	97	2	91
	2.3	(12,3,2)	96	(12,3,3,2)	96	(3,3,3,3,2)	96	(3,3,2)	96	3	94
	4.5	(9,10,6)	93	(9,10,3,6)	92	(10,3,3,3,6)	94	(10,3,6)	95	2	90
40	0	(12,11,1)	95	(12,11,3,1)	94	(11,3,3,3,1)	95	(11,3,1)	95	3	93
	2.3	(10,9,5)	95	(10,9,3,5)	95	(9,3,3,3,5)	95	(9,3,5)	95	3	94
	4.5	(12,4,5)	96	(12,4,3,5)	96	(4,3,3,3,5)	96	(4,3,5)	91	3	95
45	0	(10,3,1)	93	(10,3,3,1)	91	(3,3,3,3,1)	96	(3,3,1)	93	3	91
	2.3	(10,6,5)	96	(10,6,3,5)	96	(6,3,3,3,5)	97	(6,3,5)	97	2	90
	4.5	(10,6,10)	97	(10,6,3,10)	96	(6,3,3,3,10)	95	(6,3,10)	95	2	92
50	0	(10,5,1)	96	(10,5,3,1)	95	(5,3,3,3,1)	96	(5,3,1)	96	2	92
	2.3	(8,7,1)	90	(8,7,3,1)	90	(7,3,3,3,1)	96	(7,3,1)	96	3	89
	4.5	(8,7,10)	96	(8,7,3,10)	96	(7,3,3,3,10)	92	(7,3,10)	96	3	91

Table A.9 Black box system identification results (Subject # 10).

Freq	Mass	ARX		ARMAX		BJ		OE		SS	
(Hz)	(kg)	(na, nb, nk)	fit (%)	(na, nb, nc, nk)	fit (%)	(nb, nc, nd, nf, nk)	fit (%)	(nb, nf, nk)	fit (%)	(order)	fit (%)
10	0	(15,13,7)	69	(15,13,5,7)	66	(13,5,5,5,7)	51	(13,5,7)	80	6	59
	2.3	(11,12,1)	74	(11,12,5,1)	80	(12,5,5,5,1)	86	(12,5,1)	87	8	82
	4.5	(13,12,9)	82	(13,12,5,9)	64	(12,5,5,5,9)	79	(12,5,9)	91	8	72
15	0	(9,5,1)	85	(9,5,5,1)	84	(5,5,5,5,1)	86	(5,5,1)	87	7	85
	2.3	(9,13,4)	85	(9,13,5,4)	76	(13,5,5,5,4)	85	(13,5,4)	90	8	89
	4.5	(13,9,10)	74	(13,9,5,10)	78	(9,5,5,5,10)	84	(9,5,10)	87	9	87
20	0	(12,4,3)	87	(12,4,5,3)	89	(4,5,5,5,3)	90	(4,5,3)	90	10	93
	2.3	(9,6,11)	92	(9,6,5,11)	93	(6,5,5,5,11)	94	(6,5,11)	96	10	94
	4.5	(12,4,10)	88	(12,4,3,10)	90	(4,3,3,3,10)	93	(4,3,10)	93	9	94
25	0	(9,10,10)	92	(9,10,5,10)	90	(10,5,5,5,10)	93	(10,5,10)	93	10	94
	2.3	(12,1,4)	88	(12,1,5,4)	87	(1,5,5,5,4)	90	(1,5,4)	90	7	90
	4.5	(9,14,12)	93	(9,14,5,12)	91	(14,5,5,5,12)	91	(14,5,12)	96	7	90
30	0	(11,11,3)	90	(11,11,5,3)	91	(11,5,5,5,3)	92	(11,5,3)	96	7	93
	2.3	(11,11,3)	94	(11,11,5,3)	92	(11,5,5,5,3)	87	(11,5,3)	97	5	89
	4.5	(9,5,9)	90	(9,5,5,9)	94	(5,5,5,5,9)	96	(5,5,9)	95	5	92
35	0	(10,2,2)	87	(10,2,5,2)	87	(2,5,5,5,2)	88	(2,5,2)	89	3	89
	2.3	(12,8,3)	95	(12,8,3,3)	95	(8,3,3,3,3)	96	(8,3,3)	96	3	90
	4.5	(12,5,12)	85	(12,5,3,12)	84	(5,3,3,3,12)	88	(5,3,12)	92	3	89
40	0	(11,9,1)	88	(11,9,5,1)	88	(9,5,5,5,1)	90	(9,5,1)	88	3	83
	2.3	(15,4,6)	88	(15,4,5,6)	87	(4,5,5,5,6)	86	(4,5,6)	94	3	85
	4.5	(10,12,4)	96	(10,12,3,4)	96	(12,3,3,3,4)	96	(12,3,4)	96	3	91
45	0	(11,1,5)	85	(11,1,5,5)	86	(1,5,5,5,5)	84	(1,5,5)	86	2	87
	2.3	(10,3,7)	86	(10,3,5,7)	85	(3,5,5,5,7)	89	(3,5,7)	89	2	86
	4.5	(10,7,9)	95	(10,7,3,9)	95	(7,3,3,3,9)	94	(7,3,9)	93	2	90
50	0	(10,14,2)	89	(10,14,3,2)	89	(14,3,3,3,2)	90	(14,3,2)	91	2	89
	2.3	(10,8,12)	95	(10,8,3,12)	95	(8,3,3,3,12)	95	(8,3,12)	95	3	93
	4.5	(10,14,1)	96	(10,14,3,1)	96	(14,3,3,3,1)	96	(14,3,1)	96	3	92

APPENDIX B

The nonlinear equations

$$\begin{pmatrix} A_{11} & A_{12} & A_{13} & A_{14} & A_{15} & A_{16} \\ Sym & A_{22} & A_{23} & A_{24} & A_{25} & A_{26} \\ Sym & Sym & A_{33} & A_{34} & A_{35} & A_{36} \\ Sym & Sym & Sym & A_{44} & A_{45} & A_{46} \\ Sym & Sym & Sym & Sym & A_{55} & A_{56} \\ Sym & Sym & Sym & Sym & Sym & A_{66} \end{pmatrix} \begin{Bmatrix} \ddot{z}_F \\ \ddot{z}_T \\ \ddot{\theta}_2 \\ \ddot{\theta}_3 \\ \ddot{\theta}_4 \\ \ddot{x} \end{Bmatrix} = \begin{bmatrix} B_1 \\ B_2 \\ B_3 \\ B_4 \\ B_5 \\ B_6 \end{bmatrix},$$

where Sym is symmetry

$$A_{11} = m_T + m_1 + m_2 + m_3 + m_4,\ A_{12} = m_T,\ A_{13} = -\left(m_T + \frac{1}{2} m_1 + \frac{1}{2} m_2 \right) L_2 \sin\theta_2(t),$$

$$A_{14} = -\left(m_T + \frac{1}{2} m_1 + m_2 + \frac{1}{2} m_3 \right) L_3 \sin\theta_3(t),$$

$$A_{15} = -\left(m_T + \frac{1}{2} m_1 + m_2 + m_3 + \frac{1}{2} m_4 \right) L_4 \sin\theta_4(t),$$

$$A_{16} = 0,$$

$$A_{22} = m_T,\ A_{24} = -m_T L_3 \sin\theta_3(t),$$

$$A_{25} = -m_T L_4 \sin\theta_4(t),\ A_{26} = 0,$$

$$E_1 = L_1{}^2 - \left(L_2 \cos\theta_2(t) + L_3 \cos\theta_3(t) + L_4 \cos\theta_4(t) \right)^2,$$

$$E_2 = L_2 \cos\theta_2(t) + L_3 \cos\theta_3(t) + L_4 \cos\theta_4(t),$$

$$A_{32} = -m_T L_2 \sin\theta_2(t),$$

$$A_{33} = \left(m_T + \frac{1}{4} m_1 \frac{{L_1}^2}{E_1} + \frac{I_1}{E_1} \right) \left(L_2 \sin \theta_2 (t) \right)^2 + \left(m_3 + m_4 \right) \left(L_2 \cos \theta_2 (t) \right)^2 + \frac{1}{4} m_2 {L_2}^2 + I_2,$$

$$A_{34} = \left(m_T + \frac{1}{4} m_1 \frac{{L_1}^2}{E_1} + \frac{1}{2} m_2 + \frac{I_1}{E_1} \right) L_2 \sin \theta_2 (t) L_3 \sin \theta_3 (t) + \left(\frac{1}{2} m_3 + m_4 \right) L_2 \cos \theta_2 (t) L_3 \cos \theta_3 (t),$$

$$A_{35} = \left(m_T + \frac{1}{4} m_1 \frac{{L_1}^2}{E_1} + \frac{1}{2} m_2 + \frac{I_1}{E_1} \right) L_2 \sin \theta_2 (t) L_4 \sin \theta_4 (t) + \frac{1}{2} m_4 L_2 \cos \theta_2 (t) L_4 \cos \theta_4 (t),$$

$$A_{36} = 0,$$

$$A_{44} = \left(m_T + \frac{1}{4} m_1 {L_1}^2 \frac{1}{E_1} + m_2 + \frac{I_1}{E_1} \right) \left(L_3 \sin \theta_3 (t) \right)^2 + m_4 \left(L_3 \cos \theta_3 (t) \right)^2 + \frac{1}{4} m_3 {L_3}^2 + I_3,$$

$$A_{45} = \left(m_T + \frac{1}{4} m_1 {L_1}^2 \frac{1}{E_1} + m_2 + \frac{1}{2} m_3 + \frac{I_1}{E_1} \right) L_3 \sin \theta_3 (t) L_4 \sin \theta_4 (t) + \frac{1}{2} m_4 L_3 \cos \theta_3 (t) L_4 \cos \theta_4 (t),$$

$$A_{46} = 0,$$

$$A_{55} = \left(m_T + \frac{1}{4} m_1 {L_1}^2 \frac{1}{E_1} + m_2 + m_3 + \frac{I_1}{E_1} \right) \left(L_4 \sin \theta_4 (t) \right)^2 + \frac{1}{4} m_4 + I_4,$$

$$A_{56} = 0,$$

$$A_{66} = 0.$$

$$B_1 = \left(m_T + \frac{1}{2}m_1 + \frac{1}{2}m_2 \right) L_2 \cos\theta_2(t)\left(\ddot{\theta}_2\right)^2 + \left(m_T + \frac{1}{2}m_1 + m_2 + \frac{1}{2}m_3 \right) L_3 \cos\theta_3(t)\left(\ddot{\theta}_3\right)^2$$
$$+ \left(m_T + \frac{1}{2}m_1 + m_2 + m_3 + \frac{1}{2}m_4 \right) L_4 \cos\theta_4(t)\left(\ddot{\theta}_4\right)^2$$
$$- c_f \dot{z}_F - k_f \dot{z}_F - \left(m_T + m_1 + m_2 + m_3 + m_4\right)\ddot{y}_B,$$

$$B_2 = m_T L_2 \cos\theta_2(t)\left(\dot{\theta}_2\right)^2 + m_T L_3 \cos\theta_3(t)\left(\dot{\theta}_3\right)^2 + m_T L_4 \cos\theta_4(t)\left(\dot{\theta}_4\right)^2$$
$$- k_T z_T(t) - c_T \dot{z}_T - m_T \ddot{y}_B,$$

$$B_3 = -\left\{ \begin{array}{l} \left(m_T + \frac{1}{4}m_1 \frac{{L_1}^2}{E_1} - m_3 - m_4 + \frac{I_1}{E_1} \right) {L_2}^2 \sin\theta_2(t)\cos\theta_2(t) \\ -\frac{1}{4}\left(m_1 {L_1}^2 + 4I_1\right)\frac{E_2}{{E_1}^2}\left(L_2 \sin\theta_2(t)\right)^3 \end{array} \right\}\left(\dot{\theta}_2\right)^2$$
$$-\left\{ \begin{array}{l} -\left(\frac{1}{4}m_1 {L_1}^2 + I_1 \right)\left(L_3 \sin\theta_3(t)\right)^2 L_2 \sin\theta_2(t)\frac{E_2}{{E_1}^2} \\ +\left(m_T + \frac{1}{4}m_1 \frac{{L_1}^2}{E_1} + \frac{1}{2}m_2 + \frac{I_1}{E_1} \right) L_2 \sin\theta_2(t) L_3 \cos\theta_3(t) \\ -\left(\frac{1}{2}m_3 + m_4 \right) L_3 \sin\theta_3(t) L_2 \cos\theta_2(t) \end{array} \right\}\left(\dot{\theta}_3\right)^2$$
$$-\left\{ \begin{array}{l} -\left(\frac{1}{4}m_1 {L_1}^2 + I_1 \right)\left(L_4 \sin\theta_4(t)\right)^2 L_2 \sin\theta_2(t)\frac{E_2}{{E_1}^2} \\ +\left(m_T + \frac{1}{4}m_1 {L_1}^2 \frac{1}{E_1} + \frac{1}{2}m_2 - \frac{1}{2}m_4 + \frac{I_1}{E_1} \right) L_2 \sin\theta_2(t) L_4 \cos\theta_4(t) \end{array} \right\}\left(\dot{\theta}_4\right)^2$$
$$-\left\{ \begin{array}{l} c_1 \frac{\left(E_2 L_1 \sin\theta_{10} L_2 \sin\theta_2(t)\right)^2}{E_1} + c_2\left(\frac{L_2 \sin\theta_2(t)}{\sqrt{E_1}} + 1 \right)^2 \\ -\frac{1}{2}\left(m_1 {L_1}^2 + 4I_1\right)\frac{E_2}{{E_1}^2}\left(L_2 \sin\theta_2(t)\right)^2 L_3 \sin\theta_3(t)\dot{\theta}_3 \\ -\frac{1}{2}\left(m_1 {L_1}^2 + 4I_1\right)\frac{E_2}{{E_1}^2}\left(L_2 \sin\theta_2(t)\right)^2 L_4 \sin\theta_4(t)\dot{\theta}_4 \end{array} \right\}\dot{\theta}_2$$

$$
-\left\{\begin{array}{l} c_1\left(E_2L_1\sin\theta_{10}\right)^2 L_2\cos\theta_2(t)L_3\sin\theta_3(t)\dfrac{1}{E_1} \\ +c_2L_3\cos\theta_3(t)\dfrac{\left(L_2\sin\theta_2(t)+\sqrt{E_1}\right)}{E_1} \\ -\dfrac{1}{2}\left(m_1{L_1}^2+4I_1\right)L_2\sin\theta_2(t)L_3\cos\theta_3(t)L_4\cos\theta_4(t)\dfrac{E_2}{{E_1}^2}\dot{\theta}_4 \end{array}\right\}\dot{\theta}_3
$$

$$
-\left\{\begin{array}{l} c_1\left(E_2L_1\sin\theta_{10}\right)^2 L_2\cos\theta_2(t)L_4\sin\theta_4(t)\dfrac{1}{E_1} \\ +c_2L_4\cos\theta_4(t)\dfrac{\left(L_2\sin\theta_2(t)-\sqrt{E_1}\right)}{E_1} \end{array}\right\}\dot{\theta}_4
$$

$$
+c_1L_1\sin\theta_{10}\frac{E_2}{\sqrt{E_1}}L_2\sin\theta_2(t)\dot{x}
$$

$$
-k_{11}\left[\begin{array}{l} -\sqrt{E_1}L_1\sin\theta_{10} \\ +L_2\left(\sin\theta_2(t)-\sin\theta_{20}\right)\end{array}\right]\left(-L_1\sin\theta_{10}L_2\sin\theta_2(t)\frac{E_2}{\sqrt{E_1}}+L_2\cos\theta_2(t)\right)
$$

$$
-k_{12}\left[L_2\left(\sin\theta_2(t)-\sin\theta_{20}\right)-x(t)\right]L_2\cos\theta_2(t)
$$

$$
-k_2\left[\cos^{-1}\frac{E_2}{L_1}+\theta_2(t)-\left(\theta_{10}+\theta_{20}\right)\right]\frac{L_2\sin\theta_2(t)+\sqrt{E_1}}{\sqrt{E_1}}
$$

$$
+k_3\left[\theta_3(t)-\theta_2(t)-\left(\theta_{30}-\theta_{20}\right)\right]+\left(m_t+\frac{1}{2}m_1+\frac{1}{2}m_2\right)L_2\sin\theta_2(t)\ddot{y}_b,
$$

$$
B_4=-\left\{\begin{array}{l} \left(m_T+\dfrac{1}{4}m_1\dfrac{{L_1}^2}{E_1}+\dfrac{1}{2}m_2+\dfrac{I_1}{E_1}\right)L_3\sin\theta_3(t)L_2\cos\theta_2(t) \\ -\left(\dfrac{1}{4}m_1{L_1}^2+I_1\right)\dfrac{E_2}{{E_1}^2}L_3\sin\theta_3(t)\left(L_2\sin\theta_2(t)\right)^2 \\ -\left(\dfrac{1}{2}m_3+m_4\right)L_2\sin\theta_2(t)L_3\cos\theta_3(t)\end{array}\right\}\left(\dot{\theta}_2\right)^2
$$

$$
-\left\{\begin{array}{l} -\left(\dfrac{1}{4}m_1{L_1}^2+I_1\right)\left(L_3\sin\theta_3(t)\right)^3\dfrac{E_2}{{E_1}^2} \\ +\left(m_T+\dfrac{1}{4}m_1{L_1}^2\dfrac{1}{E_1}+m_2-m_4+\dfrac{I_1}{E_1}\right){L_3}^2\sin\theta_3(t)\cos\theta_3(t)\end{array}\right\}\left(\dot{\theta}_3\right)^2
$$

$$
-\left\{\begin{array}{l}
-\left(\frac{1}{4}m_1{L_1}^2+I_1\right)\left(L_4\sin\theta_4(t)\right)^2 L_3\sin\theta_3(t)\frac{A2}{A1^2} \\
+\left(m_T+\frac{1}{4}m_1{L_1}^2\frac{1}{A1}+m_2+\frac{1}{2}m_3-\frac{1}{2}m_4+\frac{I_1}{A1}\right)L_3\sin\theta_3(t)L_4\cos\theta_4(t)
\end{array}\right\}\left(\dot{\theta}_4\right)^2
$$

$$
-\left\{\begin{array}{l}
c_1\frac{\left(E_2L_1\sin\theta_{10}\right)^2}{E_1}L_2\sin\theta_2(t)L_3\sin\theta_3(t)+c_2\left(\frac{L_2\sin\theta_2(t)+\sqrt{E_1}}{E_1}\right)L_3\sin\theta_3(t) \\
-\frac{1}{2}\left(m_1{L_1}^2+4I_1\right)\frac{E_2}{{E_1}^2}L_2\sin\theta_2(t)\left(L_3\sin\theta_3(t)\right)^2\dot{\theta}_3 \\
-\frac{1}{2}\left(m_1{L_1}^2+4I_1\right)\frac{E_2}{{E_1}^2}L_2\sin\theta_2(t)L_3\sin\theta_3(t)L_4\sin\theta_4(t)\dot{\theta}_4
\end{array}\right\}\dot{\theta}_2
$$

$$
-\left\{\begin{array}{l}
c_3+\frac{c_2\left(L_3\sin\theta_3(t)\right)^2}{E_1}+\frac{c_1\left(E_2L_1\sin\theta_{10}L_3\sin\theta_3(t)\right)^2}{E_1} \\
-\frac{1}{2}\left(m_1{L_1}^2+4I_1\right)L_4\sin\theta_4(t)\left(L_3\sin\theta_3(t)\right)^2\frac{E_2}{{E_1}^2}\dot{\theta}_4
\end{array}\right\}\dot{\theta}_3
$$

$$
-\left\{\begin{array}{l}
c_1\left(E_2L_1\sin\theta_{10}\right)^2L_4\sin\theta_4(t)L_3\sin\theta_3(t)\frac{1}{E_1} \\
+c_2L_4\sin\theta_4(t)L_3\sin\theta_3(t)\frac{1}{E_1}
\end{array}\right\}\dot{\theta}_4
$$

$$
+c_1L_1\sin\theta_{10}\frac{E_2}{\sqrt{E_1}}L_3\sin\theta_3(t)\dot{x}
$$

$$
+k_{11}\left[-\sqrt{E_1}L_1\sin\theta_{10}+L_2\left(\sin\theta_2(t)-\sin\theta_{20}\right)\right]L_1\sin\theta_{10}L_3\sin\theta_3(t)\frac{E_2}{\sqrt{E_1}}
$$

$$
-k_2\left[\cos^{-1}\frac{E_2}{L_1}+\theta_2(t)-\left(\theta_{10}+\theta_{20}\right)\right]\frac{L_3\sin\theta_3(t)}{\sqrt{E_1}}-k_3\left[\theta_3(t)-\theta_2(t)-\left(\theta_{30}-\theta_{20}\right)\right]
$$

$$
+k_4\left[\theta_4(t)-\theta_3(t)-\left(\theta_{40}-\theta_{30}\right)\right]+\left(m_t+\frac{1}{2}m_1+m_2+\frac{1}{2}m_3\right)L_3\sin\theta_3(t)\ddot{y}_b,
$$

$$
\begin{aligned}
B_5 = &-\left\{\begin{array}{l}\left(m_T+\frac{1}{4}\frac{m_1{L_1}^2}{E_1}+\frac{1}{2}m_2+\frac{I_1}{E_1}\right)L_4\sin\theta_4(t)L_2\cos\theta_2(t)\\ -\frac{1}{4}\left(m_1{L_1}^2+4I_1\right)\frac{E_2}{{E_1}^2}L_4\sin\theta_4(t)\left(L_2\sin\theta_2(t)\right)^2\\ -\frac{1}{2}m_4L_2\sin\theta_2(t)L_4\cos\theta_4(t)\end{array}\right\}\left(\dot\theta_2\right)^2\\
&-\left\{\begin{array}{l}-\left(\frac{1}{4}m_1{L_1}^2+I_1\right)\left(L_3\sin\theta_3(t)\right)^2L_4\sin\theta_4(t)\frac{E_2}{{E_1}^2}\\ +\left(m_T+\frac{1}{4}m_1{L_1}^2\frac{1}{E_1}+m_2+\frac{1}{2}m_3+\frac{I_1}{E_1}\right)L_3\cos\theta_3(t)L_4\sin\theta_4(t)\\ -\frac{1}{2}m_4L_3\sin\theta_3(t)L_4\cos\theta_4(t)\end{array}\right\}\left(\dot\theta_3\right)^2\\
&-\left\{\begin{array}{l}-\left(\frac{1}{4}m_1{L_1}^2+I_1\right)\left(L_4\sin\theta_4(t)\right)^3L_2\sin\theta_2(t)\frac{E_2}{{E_1}^2}\\ +\left(m_T+\frac{1}{4}m_1{L_1}^2\frac{1}{E_1}+m_2+m_3+\frac{I_1}{E_1}\right){L_4}^2\sin\theta_4(t)\cos\theta_4(t)\end{array}\right\}\left(\dot\theta_4\right)^2\\
&-\left\{\begin{array}{l}c_1\frac{\left(E_2L_1\sin\theta_{10}\right)^2}{E_1}L_4\sin\theta_4(t)L_2\sin\theta_2(t)+c_2\frac{L_4\sin\theta_4(t)\left(L_2\sin\theta_2(t)+\sqrt{E_1}\right)}{E_1}\\ -\frac{1}{2}\left(m_1{L_1}^2+4I_1\right)\frac{E_2}{{E_1}^2}L_2\sin\theta_2(t)L_3\sin\theta_3(t)L_4\sin\theta_4(t)\dot\theta_3\\ -\frac{1}{2}\left(m_1{L_1}^2+4I_1\right)\frac{E_2}{{E_1}^2}L_2\sin\theta_2(t)\left(L_4\sin\theta_4(t)\right)^2\dot\theta_4\end{array}\right\}\dot\theta_2\\
&-\left\{\begin{array}{l}c_1\left(E_2L_1\sin\theta_{10}\right)^2L_3\sin\theta_3(t)L_4\sin\theta_4(t)\frac{1}{E_1}+c_2L_3\sin\theta_3(t)L_4\sin\theta_4(t)\frac{1}{E_1}\\ -\frac{1}{2}\left(m_1{L_1}^2+4I_1\right)\left(L_4\sin\theta_4(t)\right)^2L_3\sin\theta_3(t)\frac{E_2}{{E_1}^2}\dot\theta_4\end{array}\right\}\dot\theta_3\\
&-\left\{c_1\left(E_2L_1\sin\theta_{10}L_4\sin\theta_4(t)\right)^2\frac{1}{E_1}+c_2\left(L_4\sin\theta_4(t)\right)^2\frac{1}{E_1}+c_4\right\}\dot\theta_4\\
&+c_1L_1\sin\theta_{10}\frac{E_2}{\sqrt{E_1}}L_4\sin\theta_4(t)\dot x\\
&-k_{11}\left[\sqrt{E_1}L_1\sin\theta_{10}-L_2\left(\sin\theta_2(t)-\sin\theta_{20}\right)\right]\left(L_1\sin\theta_{10}L_4\sin\theta_4(t)\frac{E_2}{\sqrt{E_1}}\right)
\end{aligned}
$$

$$-k_2\left[\cos^{-1}\frac{E_2}{L_1}+\theta_2(t)-(\theta_{10}+\theta_{20})\right]\frac{L_4\sin\theta_4(t)}{\sqrt{E_1}}$$
$$-k_4\left[\theta_4(t)-\theta_3(t)-(\theta_{40}-\theta_{30})\right]+\left(m_T+\frac{1}{2}m_1+m_2+m_3+\frac{1}{2}m_4\right)L_4\sin\theta_4(t)\ddot{y}_b,$$

$$B_6=-c_1\dot{x}+c_1L_1\sin\theta_{10}\frac{E_2}{\sqrt{E_1}}\left(L_2\sin\theta_2(t)\dot{\theta}_2+L_3\sin\theta_3(t)\dot{\theta}_3+L_4\sin\theta_4(t)\dot{\theta}_4\right)$$
$$+k_{12}\left[L_2\left(\sin\theta_2(t)-\sin\theta_{20}\right)-x(t)\right].$$

APPENDIX C

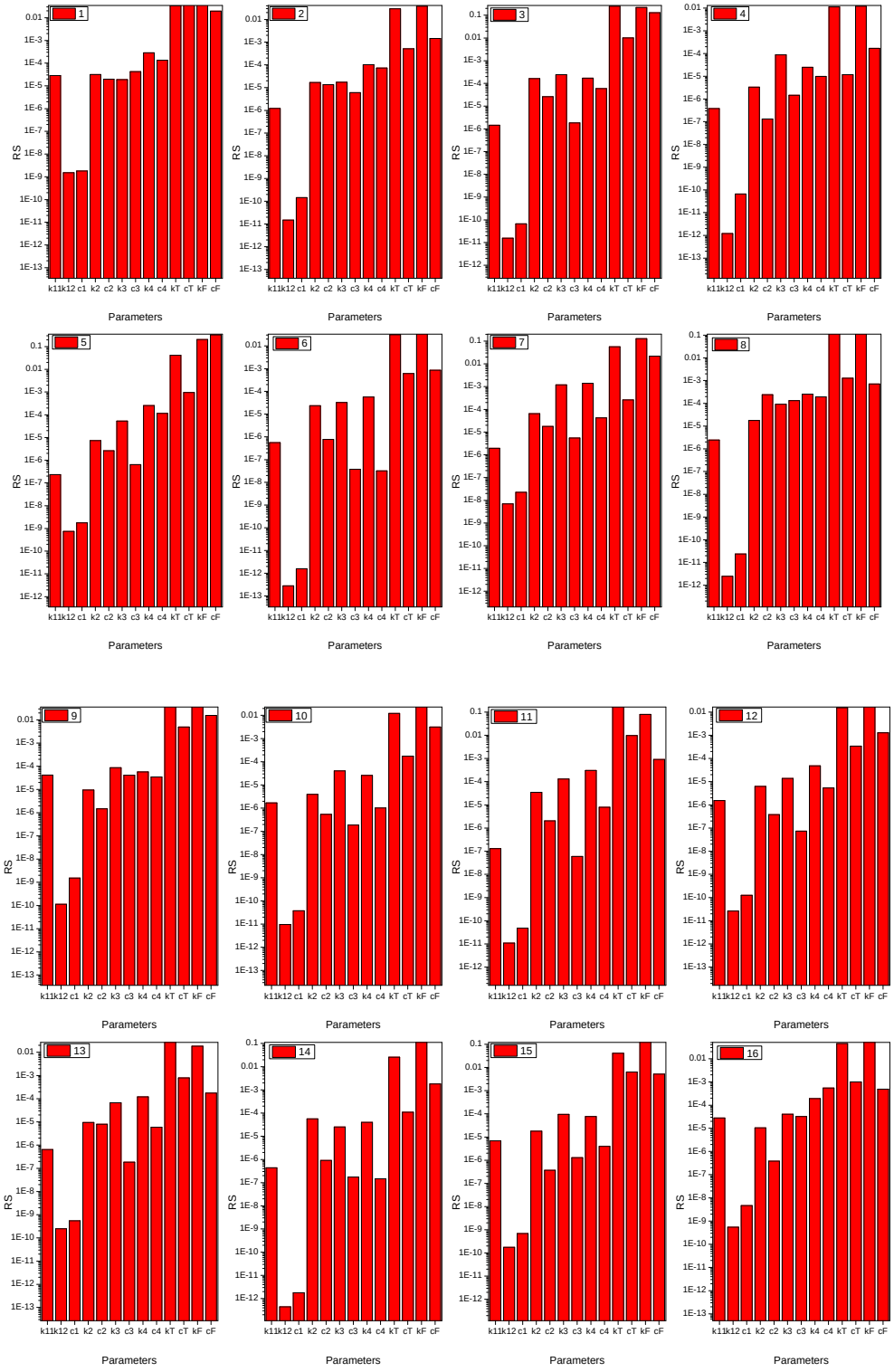
1
2
3
4
5
6
7
8
9
10
11
12
13
14
15
16
RS
Parameters
k11 k12 c1 k2 c2 k3 c3 k4 c4 kT cT kF cF

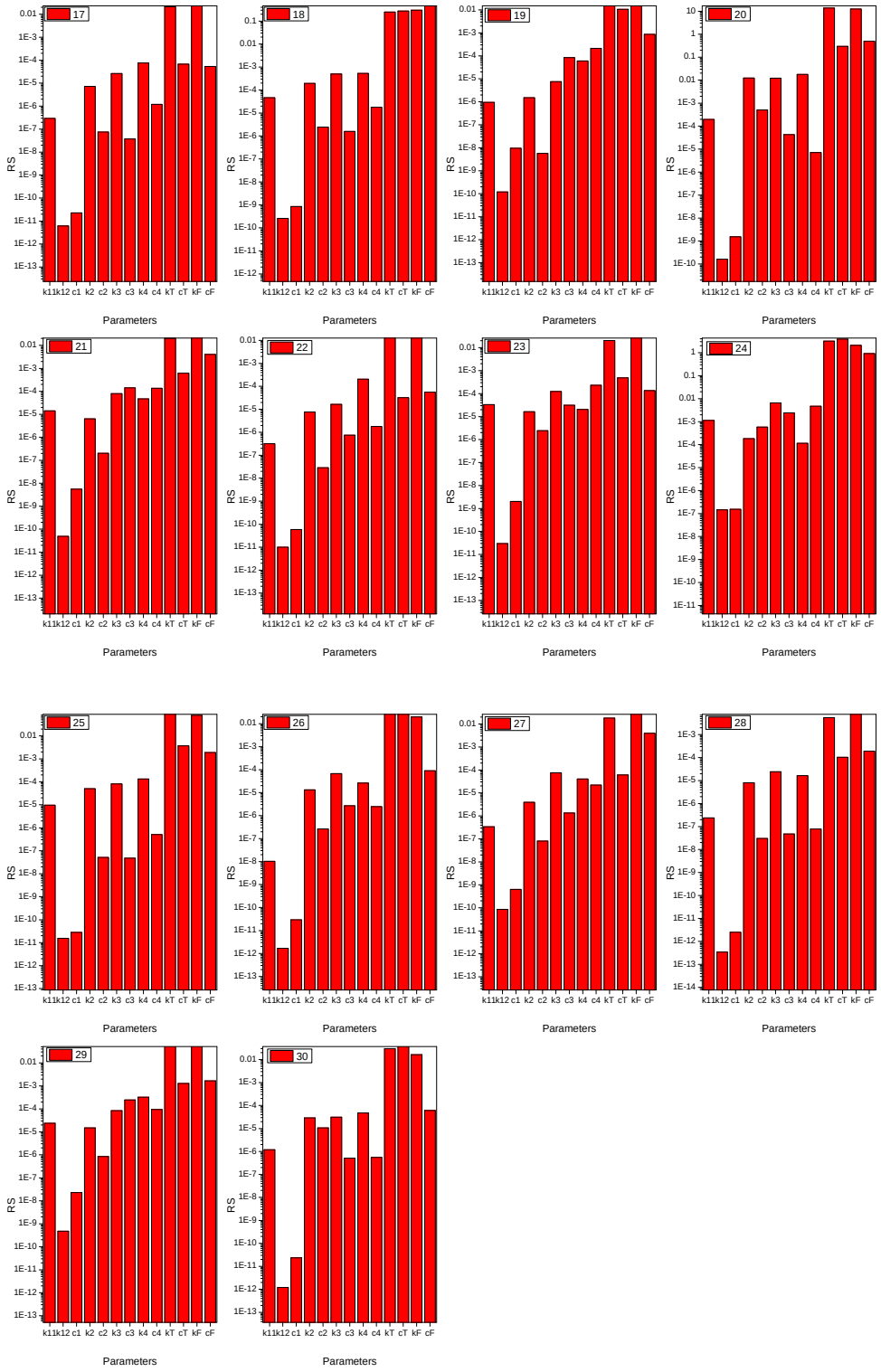

Figure C.1 The relative sensitivity of parameters (30 cases)

APPENDIX D

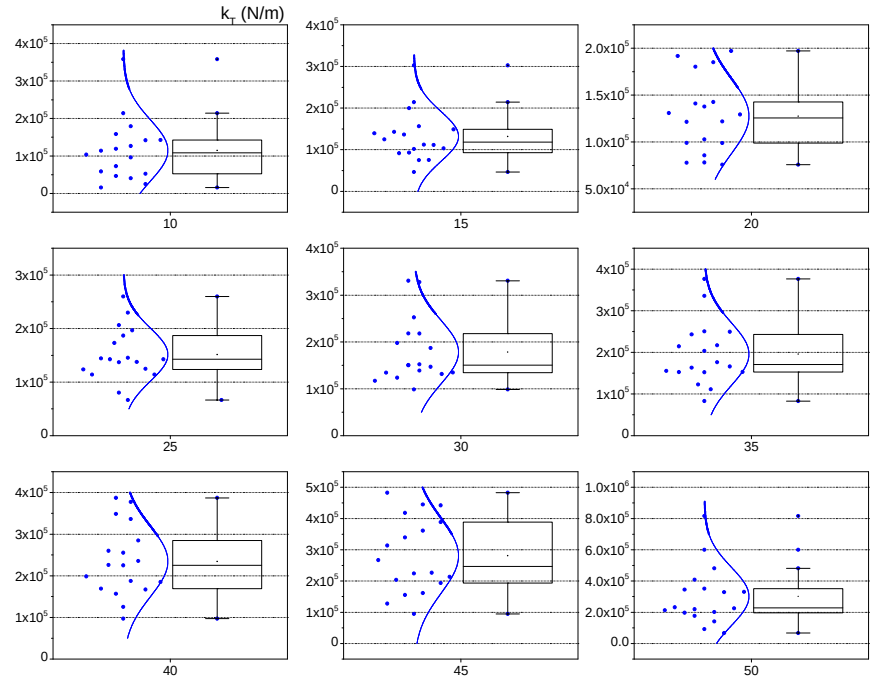

(a) The estimated spring constants (k_T) of the talocrural joint.

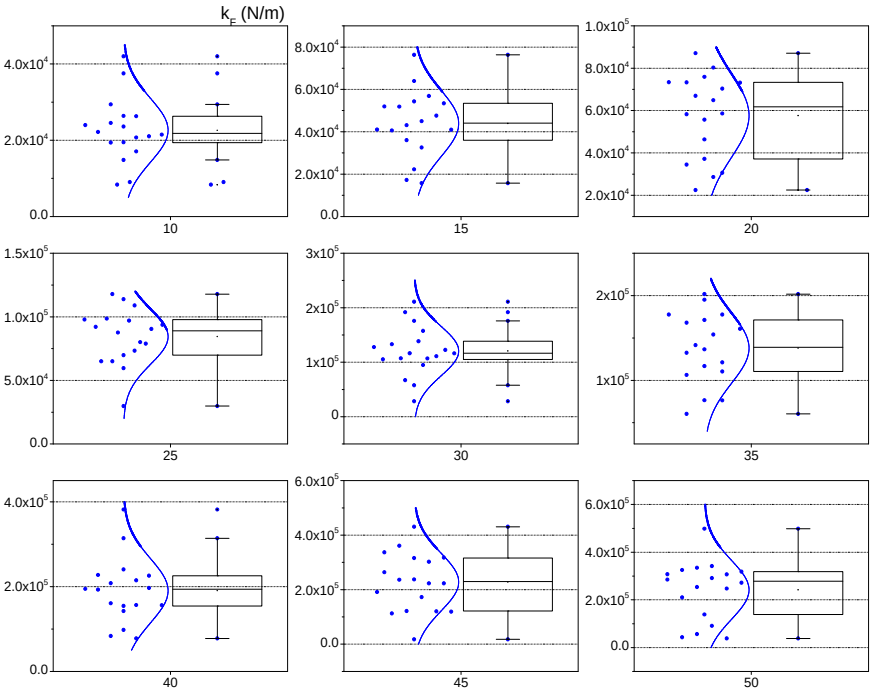

(b) The estimated spring constants (k_F) of the fat pad.

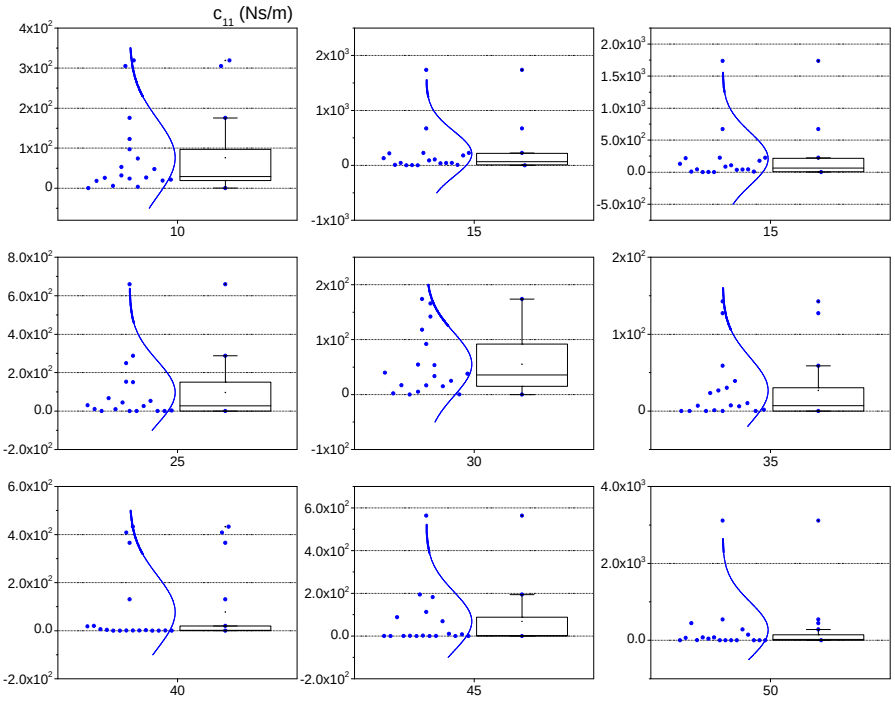

(c) The estimated damping constants (c_{11}) of the talocrural joint.

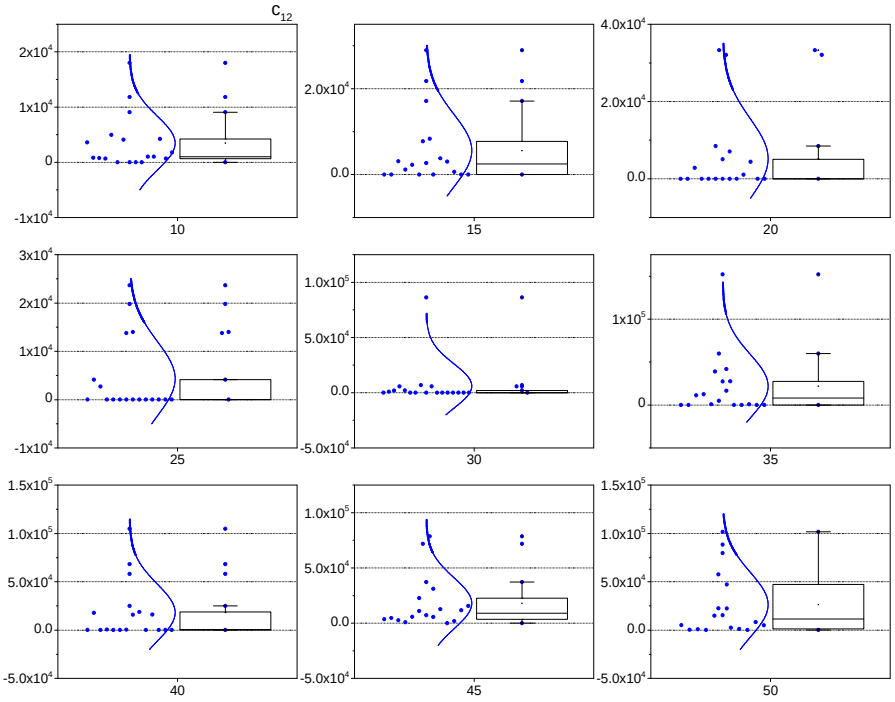

(d) The estimated damping constants (c_{12}) of the talocrural joint.

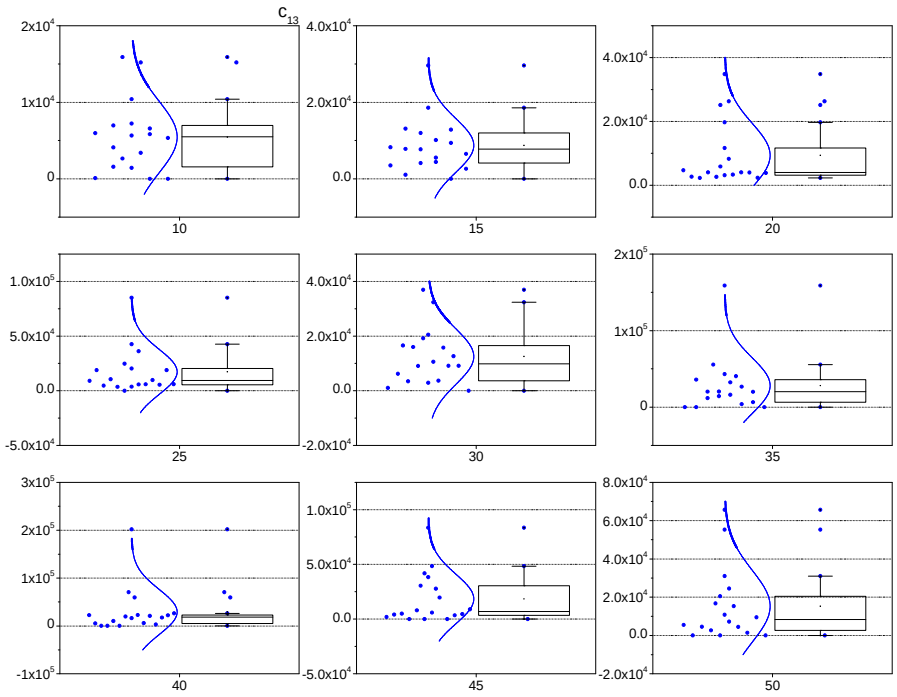

(e) The estimated damping constants (c_{13}) of the talocrural joint.

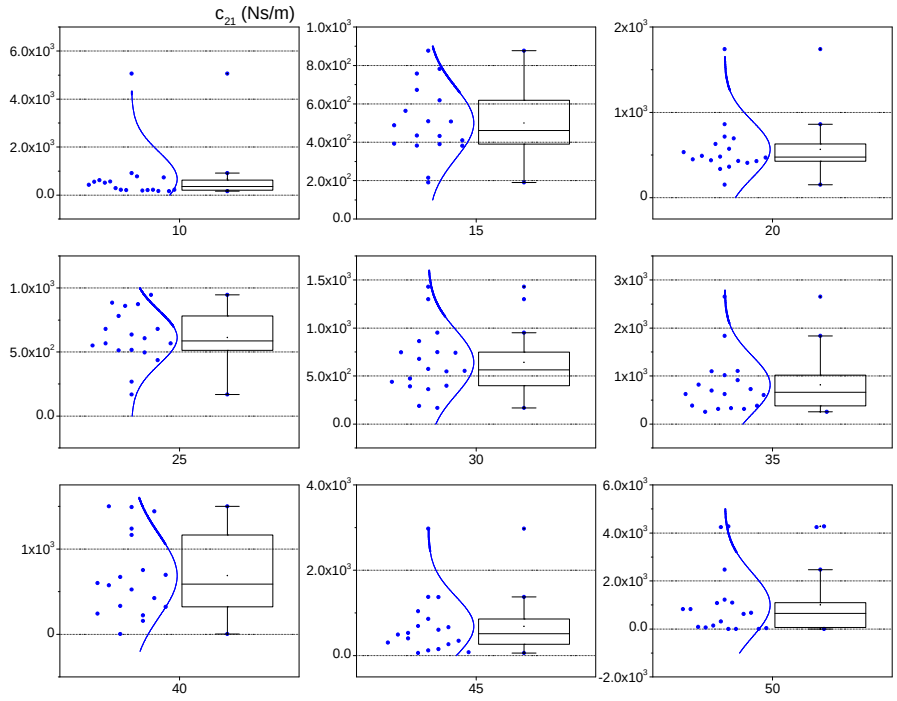

(f) The estimated damping constants (c_{21}) of the fat pad.

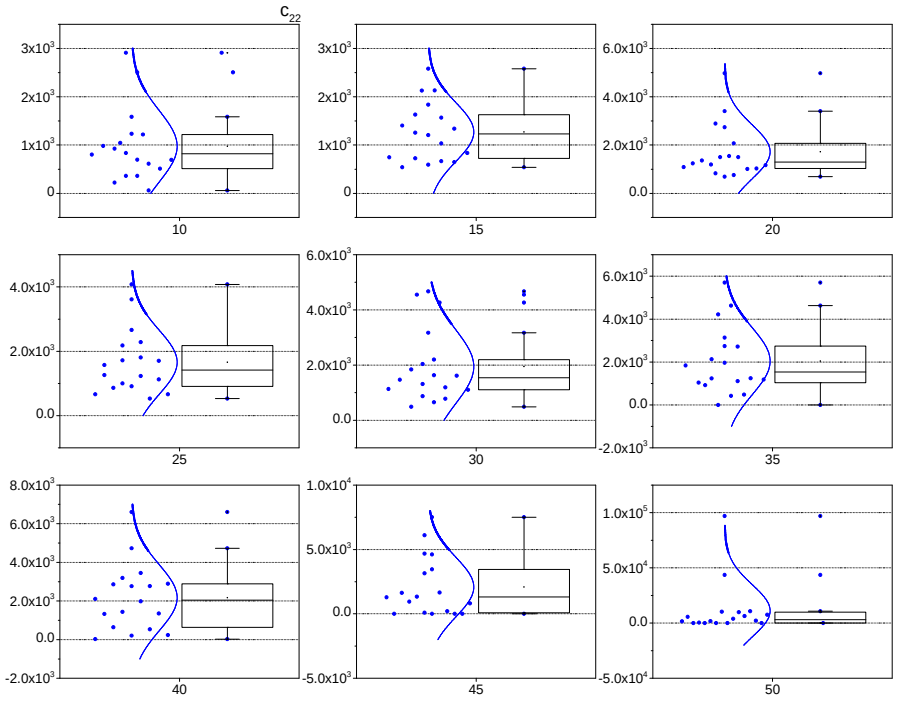

(g) The estimated damping constants (c_{22}) of the fat pad.

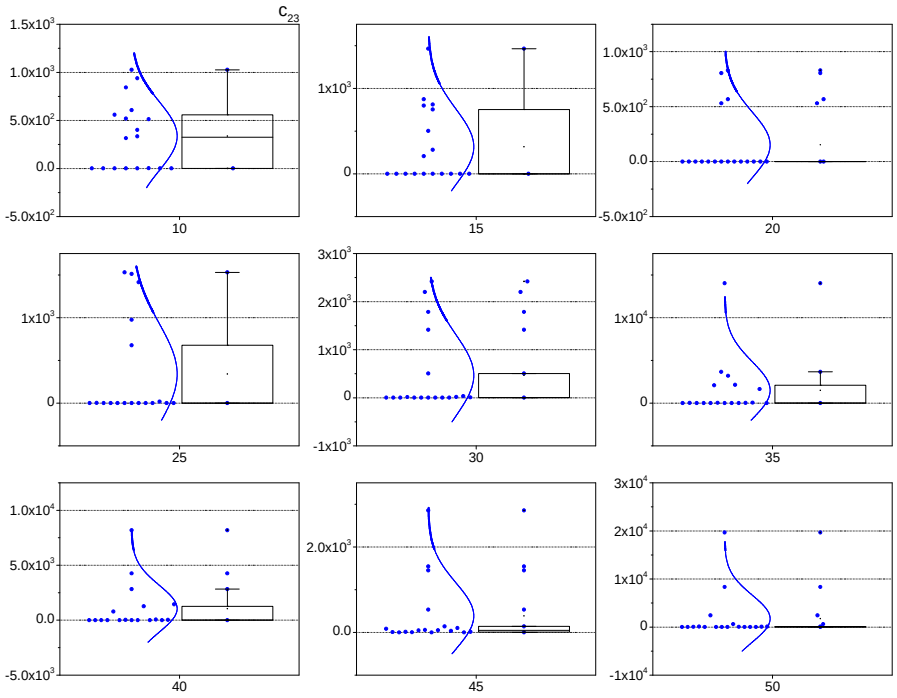

(h) The estimated damping constants (c_{23}) of the fat pad.

Figure D.1 The distribution of the estimated parameters for without an extra mass.

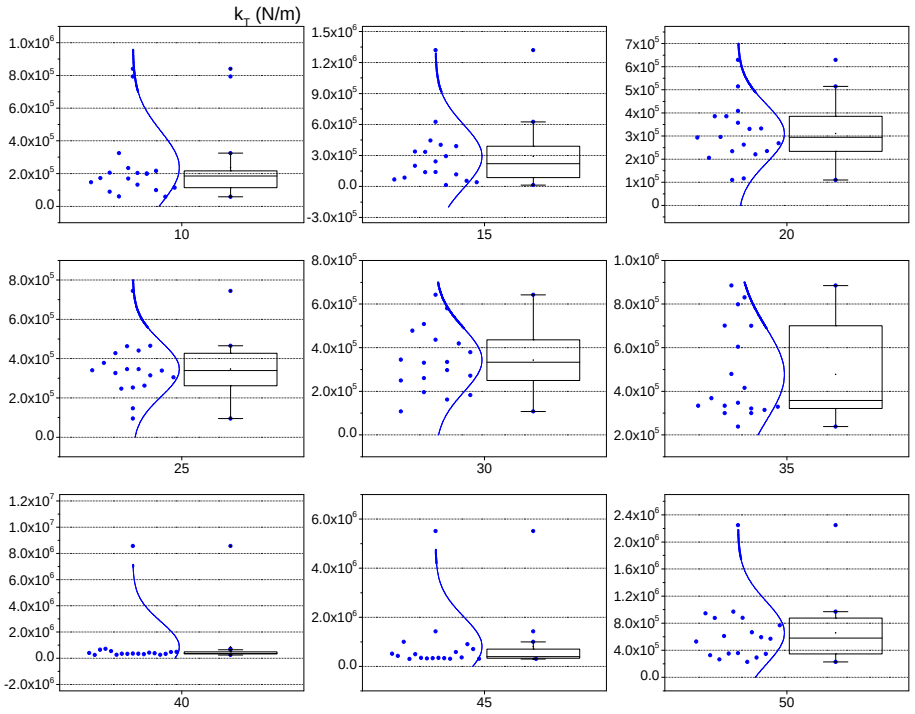

(a) The estimated spring constants (k_T) of the talocrural joint.

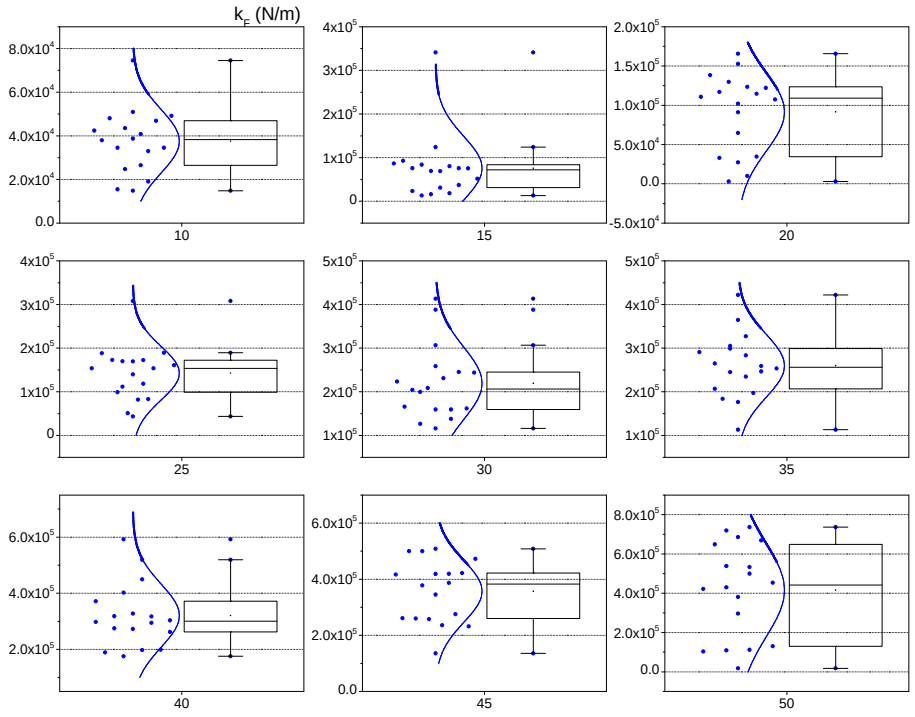

(b) The estimated spring constants (k_F) of the fat pad.

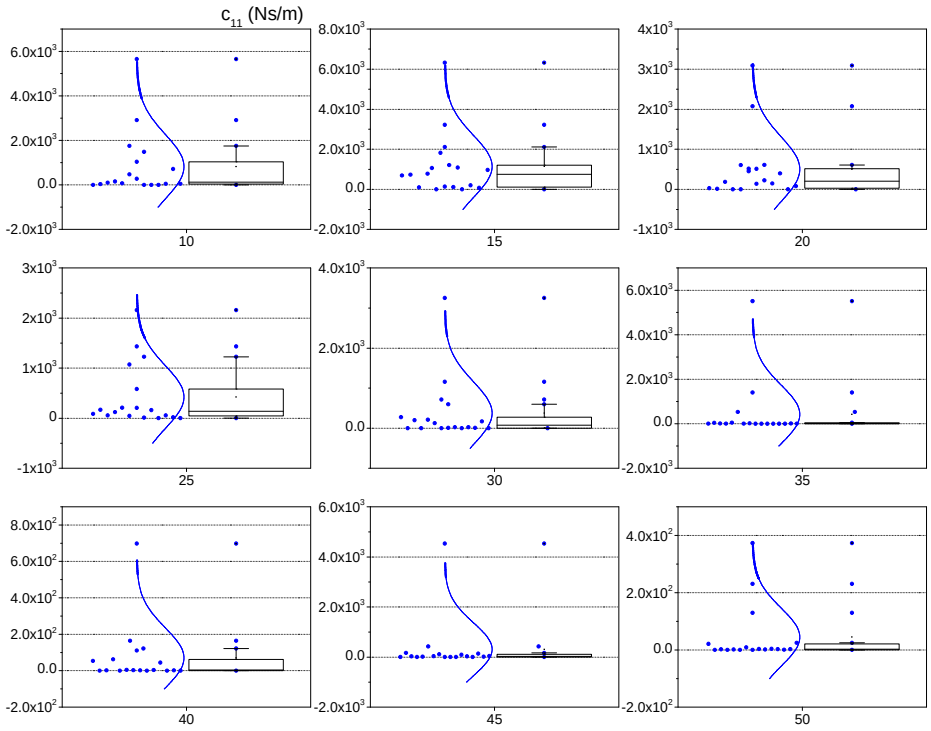

(c) The estimated damping constants (c_{11}) of the talocrural joint.

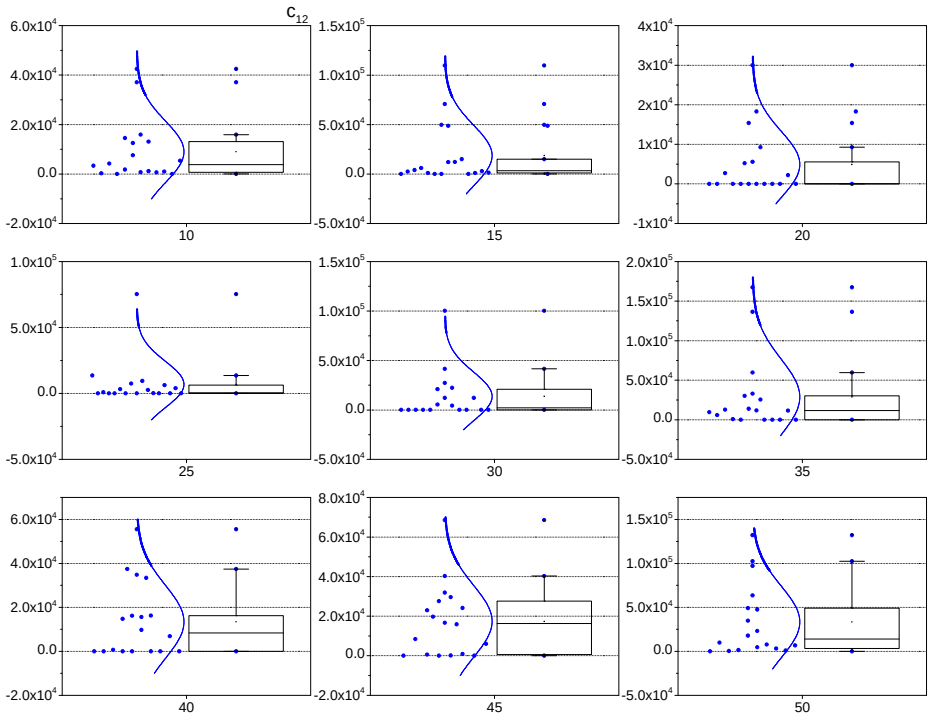

(d) The estimated damping constants (c_{12}) of the talocrural joint.

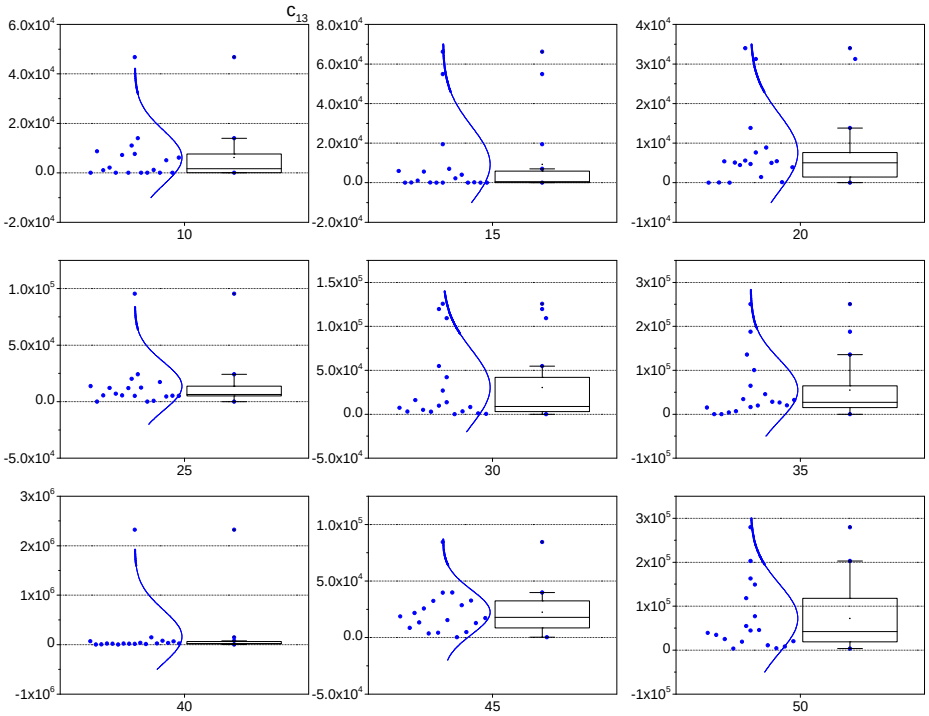

(e) The estimated damping constants (c_{13}) of the talocrural joint.

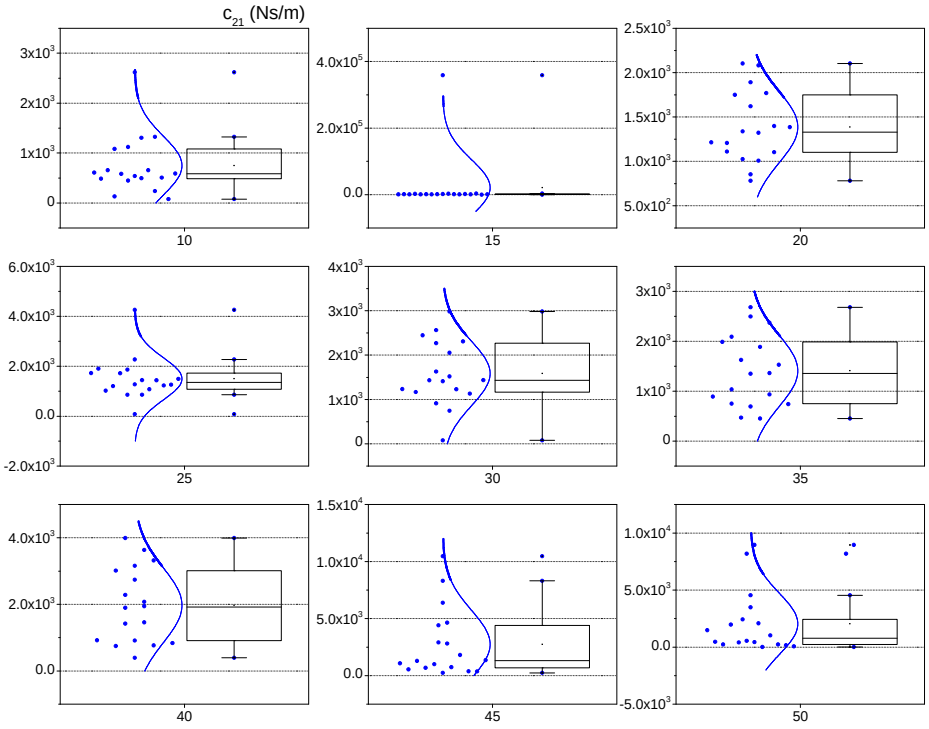

(f) The estimated damping constants (c_{21}) of the fat pad.

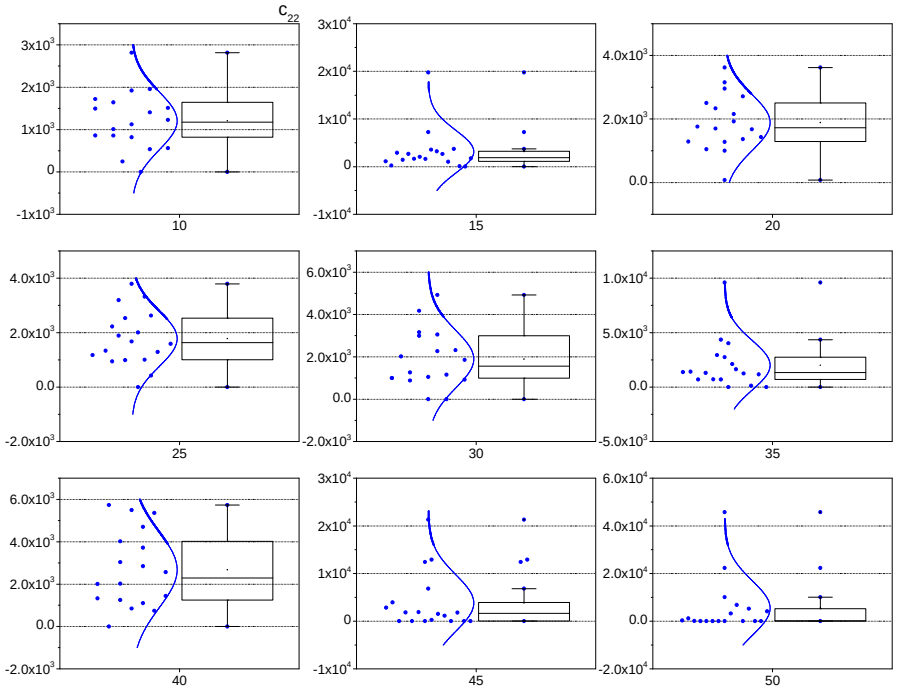

(g) The estimated damping constants (c_{22}) of the fat pad.

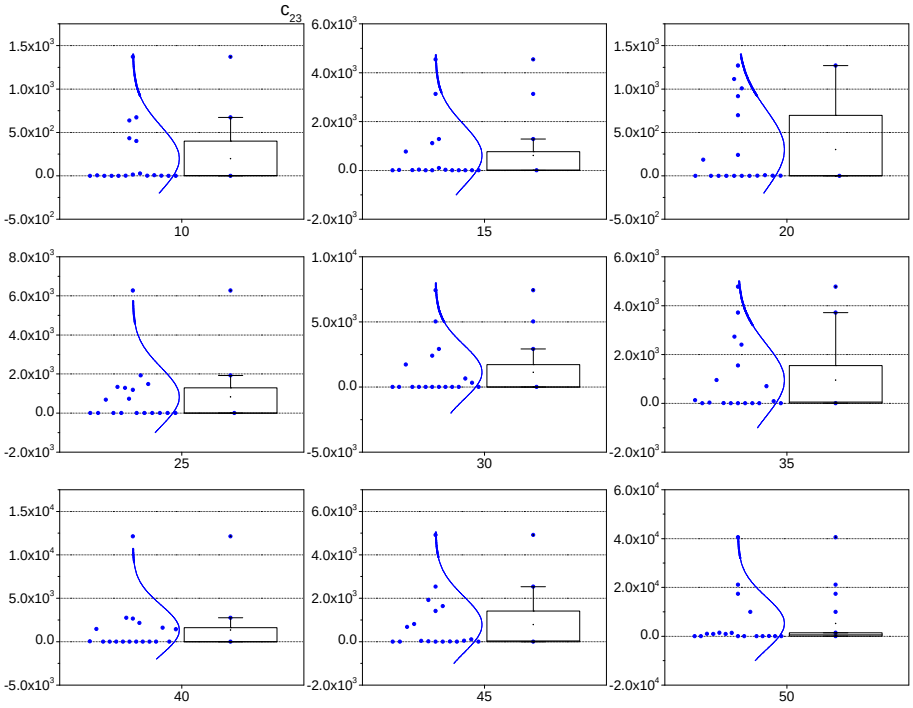

(h) The estimated damping constants (c_{23}) of the fat pad.

Figure D.2 The distribution of the estimated parameters for with 2.3 kg mass.

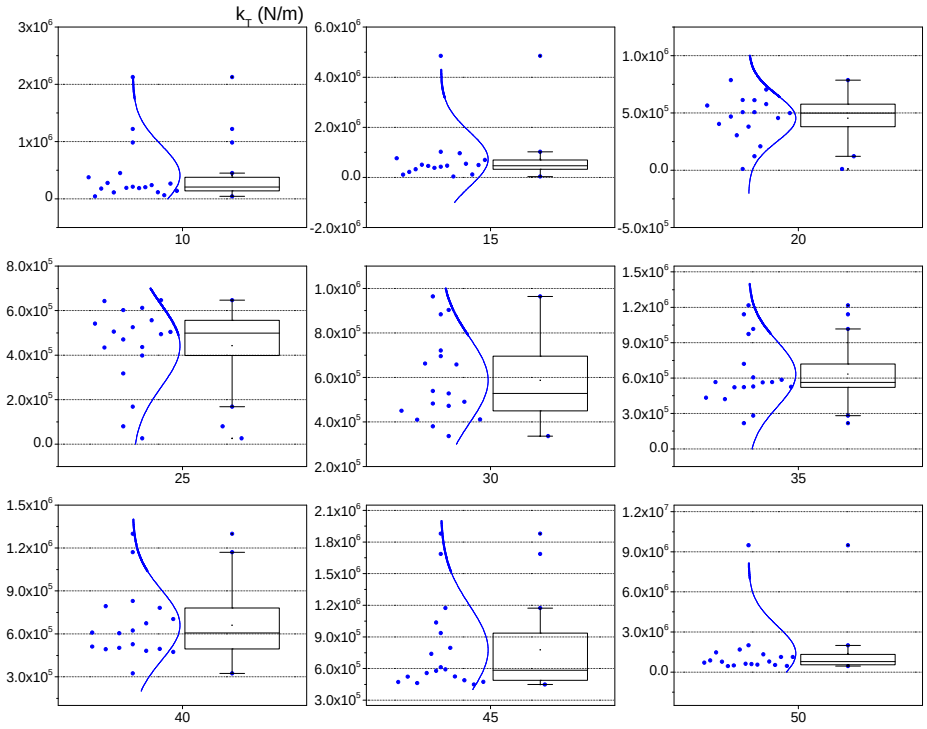

(a) The estimated spring constants (k_T) of the talocrural joint.

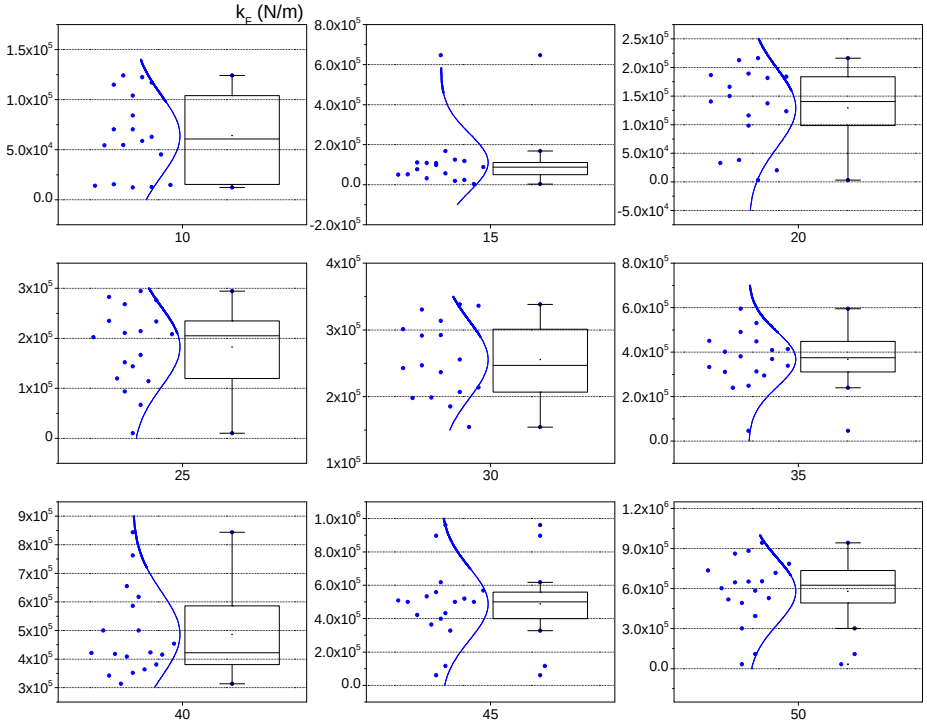

(b) The estimated spring constants (k_F) of the fat pad.

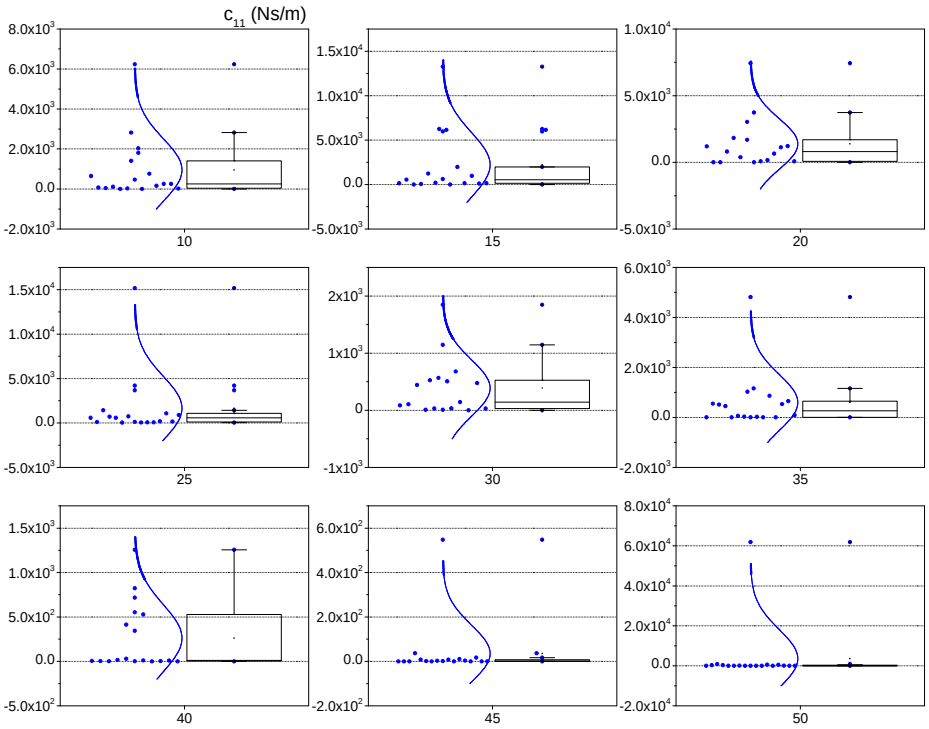

(c) The estimated damping constants (c_{11}) of the talocrural joint.

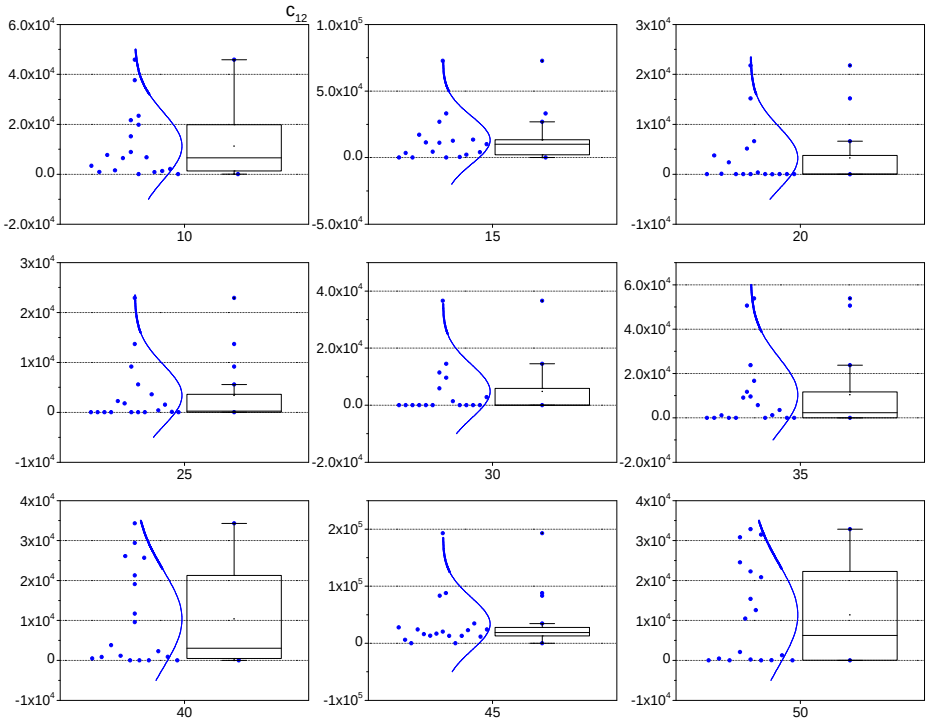

(d) The estimated damping constants (c_{12}) of the talocrural joint.

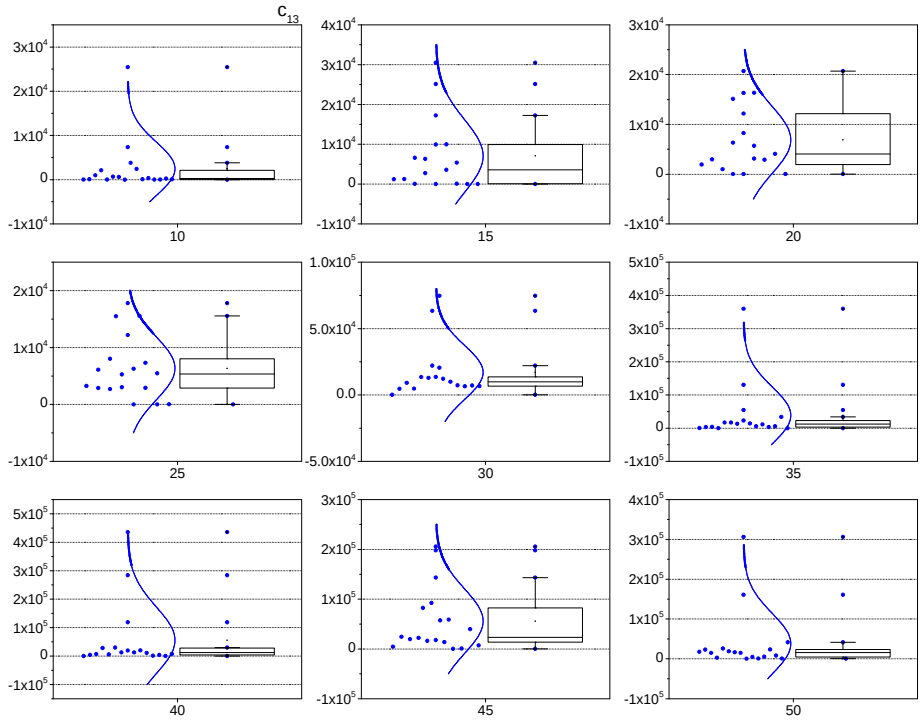

(e) The estimated damping constants (c_{13}) of the talocrural joint.

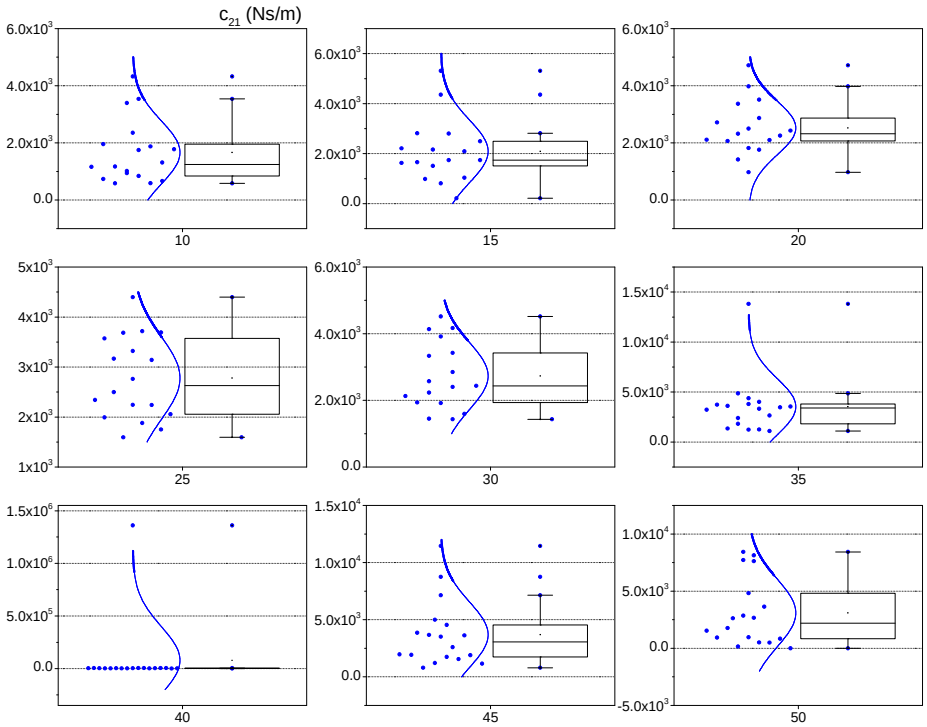

(f) The estimated damping constants (c_{21}) of the fat pad.

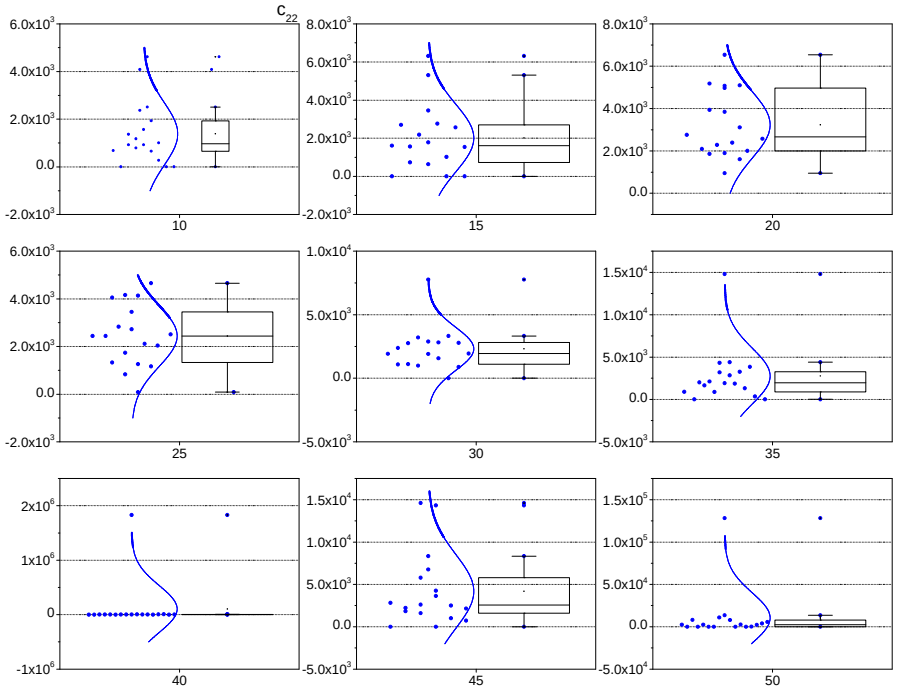

(g) The estimated damping constants (c_{22}) of the fat pad.

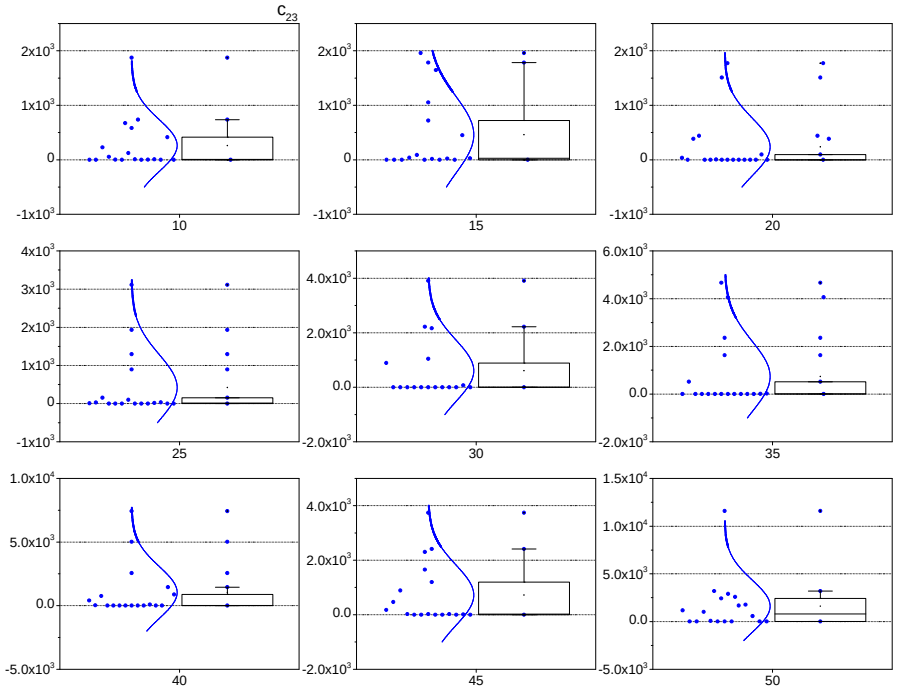

(h) The estimated damping constants (c_{23}) of the fat pad.

Figure D.3 The distribution of the estimated parameters for with 4.5 kg mass.

VITA

Hwa Bok Wee was born on Jun 18, 1973 in Sunchon, Chonnma, Korea. He graduated from Sunchon high school in 1991. He obtained his B.S. in Mechanical Engineering of Sunchon National University in 1995. After graduating in February 1995, he served Korean Army military service as an officer (platoon leader) for two and half years. Later, after finishing his military service, he continued his graduate studies at Sunchon National University and earned his M.S. degree in 2000. Since 2000, he worked for three and half years as a as a research engineer at Signetics Korea. He started his Ph.D. at University of Utah in 2004 and transferred to Lehigh University in 2006. He received a Ph.D. in Mechanical Engineering and Mechanics degree in 2012.